

Measurement of photonuclear jet production in ultraperipheral Pb + Pb collisions at $\sqrt{s_{NN}} = 5.02$ TeV with the ATLAS detector

G. Aad *et al.**
(ATLAS Collaboration)

 (Received 18 September 2024; accepted 28 January 2025; published 19 March 2025)

In ultrarelativistic heavy ion collisions at the LHC, each nucleus acts as a source of high-energy real photons that can scatter off the opposing nucleus in ultraperipheral photonuclear ($\gamma + A$) collisions. Hard scattering processes initiated by the photons in such collisions provide a novel method for probing nuclear parton distributions in a kinematic region not easily accessible to other measurements. ATLAS has measured production of dijet and multijet final states in ultraperipheral Pb + Pb collisions at $\sqrt{s_{NN}} = 5.02$ TeV using a dataset recorded in 2018 with an integrated luminosity of 1.72 nb^{-1} . Photonuclear final states are selected by requiring a rapidity gap in the photon direction; this selects events where one of the outgoing nuclei remains intact. Jets are reconstructed using the anti- k_t algorithm with radius parameter, $R = 0.4$. Triple-differential cross sections, unfolded for detector response, are measured and presented using two sets of kinematic variables. The first set consists of the total transverse momentum (H_T), rapidity, and mass of the jet system. The second set uses H_T and particle-level nuclear and photon parton momentum fractions, x_A and z_γ , respectively. The results are compared with leading-order perturbative QCD calculations of photonuclear jet production cross sections, where all leading order predictions using existing fits fall below the data in the shadowing region. More detailed theoretical comparisons will allow these results to strongly constrain nuclear parton distributions, and these data provide results from the LHC directly comparable to early physics results at the planned Electron-Ion Collider.

DOI: [10.1103/PhysRevD.111.052006](https://doi.org/10.1103/PhysRevD.111.052006)

I. INTRODUCTION

Studies of hard-scattering processes are a crucial component of the ultrarelativistic heavy-ion physics programs at the Large Hadron Collider (LHC) and the Relativistic Heavy Ion Collider. Such studies will soon reach or, in some cases, have already reached [1–3] a level of precision where measurements are sensitive to nuclear modifications of the parton distribution functions (PDFs) in the colliding nuclei. The modification of nuclear PDFs (nPDFs), relative to the PDFs of free nucleons, has been a subject of extensive study since the first measurements by the EMC experiment [4] decades ago. However, the scarcity of available data has hindered the interpretation of the observed nuclear modifications, limiting the precision of global fits compared to those performed for the proton PDFs (see, e.g. Refs. [5–8]).

Recent advances in the methods used to perform global fits to nuclear PDFs [9] and extensions to next-to-next-to-leading-order (NNLO) [10] in perturbative QCD, combined with the inclusion [3,11–13] of recent data from the LHC and experiments at Jefferson Laboratory, have significantly reduced uncertainties in the extracted nuclear PDFs. However, global fits remain limited by the precision and kinematic coverage of experimental data, requiring new measurements that cover a large kinematic range in Bjorken x and Q^2 for a heavy nucleus. Measurements are particularly important in the region of intermediate Q^2 ($100 \text{ GeV}^2 \lesssim Q^2 \lesssim 10^4 \text{ GeV}^2$), where data are lacking for a wide range of Bjorken x values. Such data will be provided by deep-inelastic scattering measurements at the Electron-Ion Collider (EIC) [14] when it becomes operational, but those data will also have limited Q^2 coverage at low x ($x \lesssim 10^{-2}$), where “shadowing,” the suppression of the nuclear PDFs at low x , is observed [15].

Ultraperipheral nuclear collisions (UPCs) [16–18] provide an opportunity to study nuclear PDFs using quasireal photons associated with one of the colliding nuclei as an electromagnetic (EM) probe of the other nucleus [19–21]. In a leading-order (LO) description of such “photonuclear” ($\gamma + A$) collisions, the photon can either scatter directly off

*Full author list given at the end of the article.

Published by the American Physical Society under the terms of the [Creative Commons Attribution 4.0 International license](https://creativecommons.org/licenses/by/4.0/). Further distribution of this work must maintain attribution to the author(s) and the published article’s title, journal citation, and DOI. Open access publication funded by CERN.

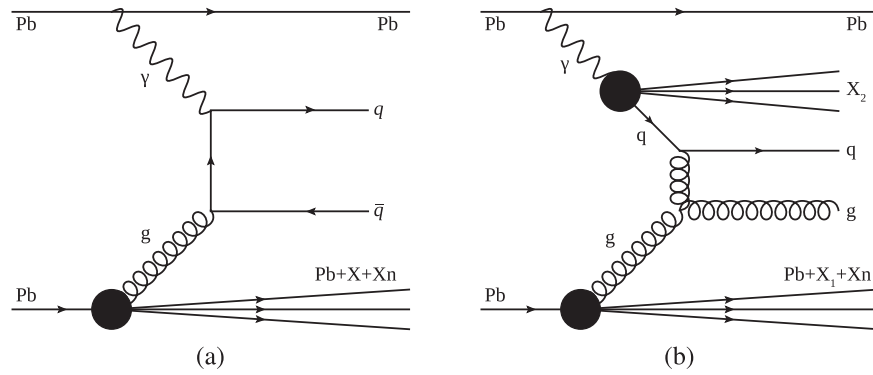


FIG. 1. Diagrams representing different types of leading-order contributions to dijet production in high-energy photon-nucleus collisions. Diagram (a) represents the direct contribution in which the photon itself participates in the hard scattering. Diagram (b) represents the “resolved” contribution in which a virtual excitation of the photon, into a state involving at least a $q\bar{q}$ pair and possibly multiple gluons, participates in the hard scattering. The black circles represent hadronic processes where hard partons are contributed from the initial state. Additional hadronic particle production occurs in the final state resulting from the breakup of the struck nucleus (X , X_1) or the resolved photon remnant (X_2).

a quark or gluon from the opposing nucleus or fluctuate, virtually, into a hadronic state that undergoes a hard-scattering process with that nucleus. The two different processes, often referred to as “direct” and “resolved,” respectively, are illustrated in Fig. 1.

At the LHC, the incident nuclei generate large fluxes of coherent photons with energies up to around 80 GeV. Thus, it is possible to study hard-scattering processes with Q^2 values well in excess of 100 GeV² initiated by the photons. Such photonuclear collisions typically produce two or more detected jets that can be used to reconstruct the kinematics of the incoming particles. Therefore, UPC photonuclear production of dijet or multijet final states in Pb + Pb collisions provides a direct probe of lead nPDFs. These measurements cover a unique range of parton kinematics due to the photonuclear collision system, allowing them to probe nPDFs at higher Q^2 than fixed-target experiments, over a broad range in x . These UPC measurements are complementary to other measurements [22,23] at the LHC in $p + \text{Pb}$ collisions that also provide useful constraints on the lead PDFs. Since $p + \text{Pb}$ collisions have a larger underlying event and more energetic hadronic probe, they have wider coverage in Bjorken x but do not extend as low in Q^2 . The kinematic coverage from photonuclear processes provides access to both the shadowing region at low x and the antishadowing region, where the nPDFs rise at intermediate x ($10^{-2} \lesssim x \lesssim 10^{-1}$). The use of an EM probe in UPCs also reduces the theoretical uncertainty associated with hadronic physics when extracting nPDFs.

The cross section for $\gamma + A$ processes and the final-state jet kinematics depend crucially on the photon flux provided by the incident nuclei. Thus, the recent incorporation of nuclear photon fluxes [24] into the PYTHIA8 [25] event generator has greatly facilitated UPC measurements at the LHC by allowing for more accurate modeling of the relevant initial state. Recent measurements, such as those

of dilepton production in ultraperipheral $\gamma\gamma$ scattering [26–29], have provided stringent tests of the current theoretical understanding of the flux generated by a nucleus. However, there remain some open issues [30–32] associated with the flux calculation, particularly involving the treatment of higher-energy photons produced inside the nucleus, which are relevant for measuring photonuclear jet production.

Additional uncertainty on the photon energy modeling arises from sensitivity to the photon fragmentation functions [33] introduced by resolved processes. To reduce the impact of photon flux and fragmentation uncertainties, measurements of photoproduction cross sections should be performed in intervals of photon energy. Resolved processes, however, do not allow for a straightforward extraction of the photon energy, so the hard-scattering kinematics are best characterized by the quantity $z_\gamma \equiv y_\gamma x_\gamma$, where y_γ is the fractional photon momentum, $y_\gamma \equiv E_\gamma / (\sqrt{s_{\text{NN}}}/2)$. x_γ is the fraction of the photon’s momentum carried by the parton entering the hard scattering, where $x_\gamma = 1$ for direct processes. These variables are further described and defined in terms of final-state jets in Sec. IV C.

UPC photonuclear scattering can be distinguished from non-UPC hard-scattering processes by requiring the photon-emitting nucleus to remain intact. Experimentally, this is accomplished by using the zero-degree calorimeters (ZDCs), which detect the beam-energy neutrons emitted in most hadronic nuclear interactions. The condition that no neutrons ($0n$) are observed in one direction, combined with a requirement for gaps in the particle rapidity distribution on that side of the event, is effective at identifying photonuclear collisions [34]. A requirement that at least one neutron (Xn) is observed in the other direction distinguishes photonuclear events from, for example, $\gamma\gamma$ scattering processes, and suppresses these backgrounds.

Although the emission of a coherent photon by an entire nucleus typically does not lead to nuclear breakup,

TABLE I. Ranges in the two sets of kinematic variables covered by the measurement and the intervals used in each variable for the measured cross sections.

Kinematic set	Variable	Minimum value	Maximum value	Interval type	Number of intervals
$(y_{\text{jets}}, m_{\text{jets}}, H_{\text{T}})$	y_{jets}	-4	2	linear	12
	m_{jets}	35 GeV	335 GeV	log	8
	H_{T}	35 GeV	275 GeV	log	8
$(x_{\text{A}}, z_{\gamma}, H_{\text{T}})$	x_{A}	2.0×10^{-3}	0.5	log	10
	z_{γ}	3.7×10^{-4}	0.027	log	7
	H_{T}	35 GeV	275 GeV	log	8

it is well known [35–37] that additional soft EM interactions between passing nuclei—so-called Coulomb excitations—can cause the photoemitting nucleus to break up. This process typically occurs via the excitation of the nucleus to a giant dipole resonance [38], which subsequently decays, emitting several neutrons. The probability for such neutron emission is sensitive to the inter-nuclear impact parameter [39]. The sampled impact parameters are smaller for $\gamma + A$ processes producing jets than, for example, $\gamma\gamma$ production of dileptons because of the higher required photon energies. Consequently, it is expected that nuclear breakup probabilities will be larger in $\gamma + A$ processes than, for example, $\gamma\gamma \rightarrow \mu^+\mu^-$. To reduce the sensitivity to theoretical uncertainties in modeling nuclear breakup, measurements of the breakup probability as a function of kinematic variables, in particular z_{γ} , is essential.

This paper presents measurements of dijet and multijet cross sections from photoproduction processes in ultra-peripheral Pb + Pb collisions at $\sqrt{s_{\text{NN}}} = 5.02$ TeV, using data recorded in 2018 with the ATLAS detector at the LHC, corresponding to an integrated luminosity of 1.72 nb^{-1} . The jets produced in $\gamma + A$ collisions are reconstructed using the anti- k_t algorithm [40,41] with a radius parameter $R = 0.4$. Triple-differential cross sections, unfolded for detector response, are measured using two sets of kinematic variables. The first set is based on the kinematics of the jet system: the jet system rapidity, y_{jets} , the jet system mass, m_{jets} , and H_{T} , the scalar sum of the transverse momenta (p_{T}) of the jets. The second set of kinematic variables more directly characterizes the hard-scattering process and parton kinematics. It consists of z_{γ} , the parton momentum fraction in the photon direction; x_{A} , the nuclear parton momentum fraction; and H_{T} , which can be viewed as a proxy for the momentum transfer, Q . Each of these variables is defined in coordinates oriented with respect to the direction (referred to hereafter as “photon-going”) of the photon-emitting nucleus, where the positive z axis points along the momentum direction of this nucleus. Table I lists the ranges covered by the measurement for each of the quantities in the two different sets of variables. The same ranges are used for both the reconstructed and unfolded results. For the differential cross sections that are the primary result of this measurement, between 8 and 12

intervals are defined covering each of the kinematic variables using either uniform linear or logarithmic divisions, as indicated in the table.

The remainder of this paper is structured as follows: Sec. II describes the ATLAS detector; Sec. III details the data and simulated event samples used in the measurement; Sec. IV discusses the reconstruction of physics objects and event selections applied in the analysis; Sec. V presents the procedure for performing the nominal analysis and cross section measurement; Sec. VI discusses systematic uncertainties; Sec. VII describes the measurement of nuclear breakup effects; Sec. VIII presents the results; and Sec. IX summarizes the paper and presents conclusions.

II. THE ATLAS DETECTOR

The ATLAS detector [42] at the LHC covers nearly the entire solid angle around the collision point.¹ It consists of an inner tracking detector surrounded by a thin superconducting solenoid, electromagnetic and hadronic calorimeters, and a muon spectrometer incorporating three large superconducting air-core toroidal magnets.

The inner-detector system (ID) is immersed in a 2 T axial magnetic field and provides charged-particle tracking in the range $|\eta| < 2.5$. The high-granularity silicon pixel detector covers the vertex region and typically provides four measurements per track, the first hit generally being in the insertable B-layer installed before Run 2 [43,44]. It is followed by the semiconductor tracker, which usually provides eight measurements per track. These silicon detectors are complemented by the transition radiation tracker, which enables radially extended track reconstruction up to $|\eta| = 2.0$. The transition radiation tracker also provides electron identification information based on the fraction of

¹ATLAS uses a right-handed coordinate system with its origin at the nominal interaction point (IP) in the center of the detector and the z axis along the beam pipe. The x axis points from the IP to the center of the LHC ring, and the y axis points upwards. Polar coordinates (r, ϕ) are used in the transverse plane, ϕ being the azimuthal angle around the z axis. The pseudorapidity is defined in terms of the polar angle θ as $\eta = -\ln \tan(\theta/2)$ and is equal to the rapidity $y = \frac{1}{2} \ln \left(\frac{E+p_z c}{E-p_z c} \right)$ in the relativistic limit. Angular distance is measured in units of $\Delta R \equiv \sqrt{(\Delta y)^2 + (\Delta \phi)^2}$.

hits (typically 30 in total) above a higher energy-deposit threshold corresponding to transition radiation.

The calorimeter system covers the pseudorapidity range $|\eta| < 4.9$. Within the region $|\eta| < 3.2$, electromagnetic calorimetry is provided by barrel and end cap high-granularity lead/liquid-argon (LAr) calorimeters, with an additional thin LAr presampler covering $|\eta| < 1.8$ to correct for energy loss in material upstream of the calorimeters. Hadronic calorimetry is provided by the steel/scintillator-tile calorimeter, segmented into three barrel structures within $|\eta| < 1.7$, and two copper/LAr hadronic end cap calorimeters. The solid angle coverage is completed with forward copper/LAr and tungsten/LAr calorimeter modules optimized for electromagnetic and hadronic energy measurements, respectively.

The muon spectrometer comprises separate trigger and high-precision tracking chambers measuring the deflection of muons in a magnetic field generated by the superconducting air-core toroidal magnets. The field integral of the toroids ranges between 2.0 and 6.0 T m across most of the detector. Three layers of precision chambers, each consisting of layers of monitored drift tubes, cover the region $|\eta| < 2.7$, complemented by cathode-strip chambers in the forward region, where the background is highest. The muon trigger system covers the range $|\eta| < 2.4$ with resistive-plate chambers in the barrel, and thin-gap chambers in the end cap regions.

The luminosity is measured mainly by the LUCID-2 [45] detector that records Cherenkov light produced in the quartz windows of photomultipliers located close to the beam pipe.

Two ZDCs, which measure neutrons emitted at small rapidity separation from the incident nuclei, are used for triggering and for offline event selection. The ZDCs are located symmetrically at a distance of ± 140 m from the nominal IP and cover $|\eta| > 8.3$ along the beam axis. Each calorimeter consists of four modules, each containing slightly more than one interaction length of tungsten absorber.

Events are selected by the first-level (L1) trigger system implemented in custom hardware, followed by selections made by algorithms implemented in software in the high-level trigger (HLT) [46]. The first-level trigger accepts events from the 40 MHz bunch crossings at a rate below 100 kHz, which the high-level trigger further reduces in order to record complete events to disk at about 1 kHz.

A software suite [47] is used in data simulation, in the reconstruction and analysis of real and simulated data, in detector operations, and in the trigger and data acquisition systems of the experiment.

III. DATA AND SIMULATED EVENT SAMPLES

A. Data sample

The measurements presented in this paper were performed using 1.72 nb^{-1} of Pb + Pb collision data recorded

by ATLAS during 2018. During that data-taking period, the typical number of hadronic Pb + Pb collisions per bunch crossing was $\mu \lesssim 5 \times 10^{-3}$. Although the likelihood of multiple hadronic collisions in a single bunch crossing is small, pileup may be induced by EM dissociation processes that have much larger cross sections [48–50]. This form of EM pileup is accounted for using methods described in Sec. VA.

The primary triggers used for the measurement involve a combination of $0nXn$ and transverse energy requirements at L1 and a requirement of at least one jet above a given p_T threshold in the HLT. In particular, the L1 triggers required that the total transverse energy measured in the ATLAS calorimeters, $\sum E_T$, satisfies $5 < \sum E_T < 200 \text{ GeV}$. The HLT jet triggers are based on anti- k_r jets with radius $R = 0.4$ reconstructed using topological clusters [51] formed from energy deposits in the calorimeter. These triggers were implemented with nominal jet- p_T thresholds of 10 and 20 GeV. For 40% of the sampled luminosity, the jet triggers were applied only over the pseudorapidity range $|\eta^{\text{jet}}| < 3.2$, while for the rest of the data jets were triggered over the range $|\eta^{\text{jet}}| < 4.9$. A separate set of events collected using only the L1 $0nXn$ and $\sum E_T$ conditions is used to evaluate the HLT jet-trigger efficiency.

In order to measure $\gamma + A$ collisions in which the photon-emitting nucleus breaks up due to additional soft-photon exchanges, a separate sample of $XnXn$ events was recorded. This sample used two triggers that require neutrons in both ZDCs. One of these selects events with a maximum $\sum E_T$ of 50 GeV and at least one track in the ID, while the other selects events with a minimum $\sum E_T$ of 50 GeV. The sampled luminosities were $33.2 \text{ } \mu\text{b}^{-1}$ and $32.7 \text{ } \mu\text{b}^{-1}$ for the first and second trigger, respectively. A sample of minimum-bias 5.02 TeV pp collisions is also used for background studies. This pp data sample was collected in 2017 using a trigger that required at least one track in the ID and collected 2.66 nb^{-1} of integrated luminosity.

B. Monte Carlo simulated samples

The primary Monte Carlo (MC) sample used for this analysis was created using the PYTHIA8 event generator, which can simulate photon-induced hard-scattering processes [52] and allows a user-defined photon flux, $F_{\gamma/A}$, to be specified. This sample was produced using the photon flux associated with a classical point charge integrated over the transverse dimensions above a minimum cutoff, $b_{\text{min}} \approx 6.62 \text{ fm}$ [24], the nominal radius of a lead nucleus, which is given in Eq. (1) by the equivalent photon approximation:

$$F_{\gamma/A}(E_\gamma) = \frac{2\alpha Z^2}{\pi} \frac{1}{\beta_B^2} \frac{1}{E_\gamma} \left[u_R K_1(u_R) K_0(u_R) - \frac{u_R^2 \beta_B^2}{2} (K_1^2(u_R) - K_0^2(u_R)) \right]. \quad (1)$$

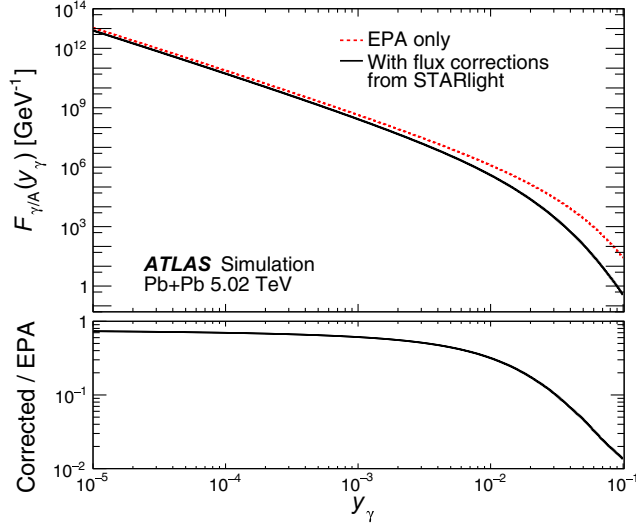


FIG. 2. The photon flux generated coherently by a single nucleus in equivalent photon approximation (EPA) with a hard cutoff at the nuclear radius (red dashed), compared to a photon flux fully corrected using the STARLIGHT [53] event generator (solid black). The ratio shown in the bottom panel is used to correct the PYTHIA8 MC sample used in this analysis.

Here $u_R = E_\gamma b_{\min} / \gamma_B \beta_B \hbar c$, α is the fine-structure constant, E_γ is the emitted photon energy, and β_B and γ_B are the Lorentz boost parameters associated with the photon-emitting nucleus. K_0 and K_1 are modified Bessel functions of the second kind. This description of the flux, however, is incomplete because it neglects effects arising from the nuclear size. First, the hard cutoff at the nuclear radius imperfectly approximates the requirement that no hadronic interactions occur in the collision. This requirement can be simulated with the STARLIGHT event generator [53], which is used in this analysis to reweight the photon spectrum in the PYTHIA8 sample. Additionally, Eq. (1) neglects the size of the struck nucleus, which is accounted for by modeling the nuclear thickness with a Woods-Saxon distribution [53] and integrating over the full range of impact parameters. The corrected and uncorrected photon fluxes are compared as a function of y_γ in Fig. 2, which demonstrates that these effects are small for collisions with small y_γ (large b) but important for large y_γ (small b), since collisions with smaller impact parameters are more sensitive to details of the collision geometry. The bottom panel of Fig. 2 shows the ratio of the corrected and uncorrected fluxes, which is the combined reweighting factor applied to the PYTHIA8 sample as a function of y_γ .

The simulated signal events include both direct and resolved photon processes; the latter require additional modeling using the CJKL photon PDF [33] set. The events were generated using the nCTEQ15 [54] nuclear parton distribution functions and the A14 set of tuned parameters (“tune”) [55]. Final-state stable particles, defined as those with $c\tau > 10$ mm, were then passed to a GEANT4-based

simulation of the ATLAS detector [56,57]. Samples with different selections on the hard-scattering kinematics were generated to ensure full coverage of the kinematic range considered in this measurement. Samples with equal numbers of events were generated for photons propagating in the positive and negative z directions.

Two other samples of events were generated to simulate potential backgrounds in the measurement. A set of diffractive photoproduction events was generated using PYTHIA8, but with a modified pomeron flux to account for coherent emission by the Pb nuclei, which yields kinematics similar to those of coherent photon emission. Since the sample of peripheral Pb + Pb events that satisfy the event-selection criteria is overwhelmingly dominated (> 99%) by events with a single binary nucleon-nucleon collision, a sample of pp collisions was generated using PYTHIA8, requiring a hard-scattering process producing jets with $p_T > 15$ GeV, to simulate this possible hadronic background.

IV. EVENT RECONSTRUCTION AND SELECTION

A. Event reconstruction

Charged particle tracks in the ID are reconstructed over the interval $|\eta^{\text{tr}}| < 2.5$ using the same methods and selections as applied in minimum-bias pp measurements [58]. Topological clusters are reconstructed over the interval $|\eta^{\text{cl}}| < 4.9$ from energy deposits in the calorimeter [51].

The jets used for this analysis are obtained from particle-flow inputs derived from tracks and clusters as described in Ref. [59]. They are reconstructed using the anti- k_r algorithm with radius parameter $R = 0.4$. The jets are calibrated to the hadronic scale using scale factors obtained from MC simulations specifically derived for low- μ pp data. A separate MC-based correction derived from the PYTHIA8 photonuclear sample is applied to account for differences in the hard-scattering physics and kinematics between $\gamma + A$ and pp events. Separate *in situ* energy scale corrections [60] are applied that account for differences in the jet response between data and simulation. These corrections are derived in low- μ 13 TeV pp data using jets recoiling against another object produced in the collision, such as another jet in a different η region or a Z boson. Details on the calibration are provided in Appendix A. The calibrations are derived such that they are valid for calibrated jet p_T values $p_T^{\text{jet}} > 15$ GeV; thus, only jets that satisfy this condition are included in the analysis. To ensure that the jets are fully contained within the acceptance of the detector, jets are also required to satisfy $|\eta^{\text{jet}}| < 4.4$.

The total energies of neutrons within the acceptance of the ZDCs are obtained by summing individual energy measurements from the four longitudinal segments of each calorimeter. The energy scale is calibrated using the single neutron peak ($E = 2.51$ TeV), for which an energy resolution of 17% is obtained. The primary analysis requires

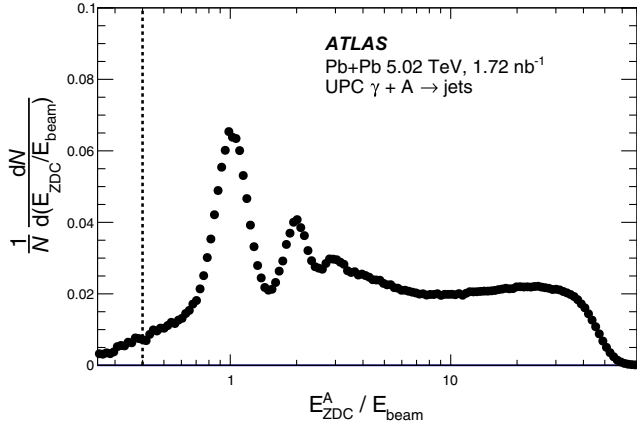


FIG. 3. Distribution of energies measured in the ATLAS ZDCs expressed in terms of the ratio of the measured energy to the beam energy, $E_{\text{beam}} = 2510$ GeV. The energies are measured in the calorimeter opposite the $0n$ side in events satisfying all photonuclear dijet event selections except the Xn energy requirement which selects events to the right of the dotted line.

events to satisfy a $0nXn$ requirement, which is imposed by requiring the energy in one of the ZDCs—the “ $0n$ ” direction—to be less than 1 TeV, while the energy in the other—the “ Xn ” direction—is greater than 1 TeV. The photon is assumed to be traveling in the $0n$ direction and the struck nucleus in the Xn direction. The distribution of ZDC energies on the struck-nucleus side is shown in Fig. 3 for events that satisfy the trigger requirements and all the event selections described in Sec. IV D except the ZDC energy requirement on the Xn side. It is observed that the single-neutron peak has a tail to small energies resulting from showers that start deep in the calorimeter and are not fully contained. The fraction of valid Xn events that would fall below the Xn energy threshold, indicated in the figure with the dashed line, is estimated to be $\lesssim 0.1\%$.

Another characteristic signature of photoproduction events is that they have large gaps in the rapidities of produced particles. This feature allows them to be separated from hadronic backgrounds. These rapidity gaps are determined using a combination of reconstructed tracks and clusters, both of which are required to have $p_T > 200$ MeV. Rapidity-dependent requirements are imposed on the significance of cluster energies relative to noise levels to suppress contributions from electronic noise [61]. So-called edge gaps, $\Delta\eta_\gamma$ and $\Delta\eta_A$ are defined as the interval between the edge of the detector ($\eta = \pm 4.9$) and the nearest track or cluster in the photon-going and nuclear-going directions, respectively.

To prevent the rejection of resolved photon processes, a second gap definition is constructed by summing all intervals, $\Delta\eta$, between η -adjacent tracks or clusters with $\Delta\eta > 0.5$. This sum includes all intervals from the most forward jet in the photon-going direction to the photon-going edge of the detector at $\eta = 4.9$, and the resulting

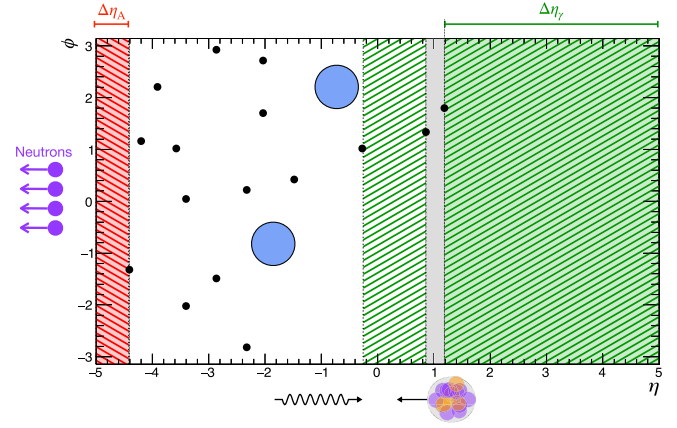


FIG. 4. Diagram illustrating how the various rapidity gap quantities are computed in a typical event with photonuclear jet production. Tracks and clusters are indicated by black points while the jets are shown with blue circles. The lack of neutrons in the positive η direction defines that as the photon-going direction. The $\Delta\eta_\gamma$ and $\Delta\eta_A$ are indicated by the green and red solid shaded areas, respectively. The regions contributing to the $\sum_\gamma \Delta\eta$ are shown with the hatched green shading, with the solid gray shaded region indicating a $\Delta\eta$ that is smaller than 0.5 and excluded from the $\sum_\gamma \Delta\eta$ calculation. All hatched regions contribute to $\sum \Delta\eta$.

quantity is denoted $\sum_\gamma \Delta\eta$. A separate sum of all intervals satisfying $\Delta\eta > 0.5$, regardless of orientation with respect to the jets, is denoted as $\sum \Delta\eta$ and is used to reject $\gamma\gamma$ backgrounds. Figure 4 illustrates how the various rapidity gap quantities are calculated.

B. Jet performance

The jet reconstruction capabilities are evaluated in the PYTHIA8 $\gamma + A \rightarrow$ jets MC sample by matching truth jets to the nearest reconstructed jet within $\Delta R < 0.3$. Response distributions, $p_T^{\text{reco}}/p_T^{\text{true}}$, are built in intervals of p_T^{true} and η^{truth} . Each distribution is fit to a Gaussian function whose mean and standard deviation are referred to as the jet energy scale (JES) and jet energy resolution (JER), respectively. The JES and JER are shown in Fig. 5 as functions of p_T^{true} for different intervals of $|\eta^{\text{truth}}|$. The mean response is generally within a half percent of unity over most of the p_T^{true} and η^{truth} range, which keeps the required unfolding corrections small.

The variation of the resolution with p_T^{jet} and $|\eta^{\text{jet}}|$ is consistent with what is observed in other ATLAS studies of jet response in pp collisions [60]. In this analysis, the resolution at the lowest p_T values is substantially smaller than in previous studies. This is because the pile-up, which is the dominant contribution in typical LHC pp analyses, is negligible in the Pb + Pb UPC dataset. The combined impact of deviations from unity in the JES and the overall effect of JER are corrected in the unfolding procedure. Possible differences in these jet calibrations between data and MC are included as sources of systematic uncertainty.

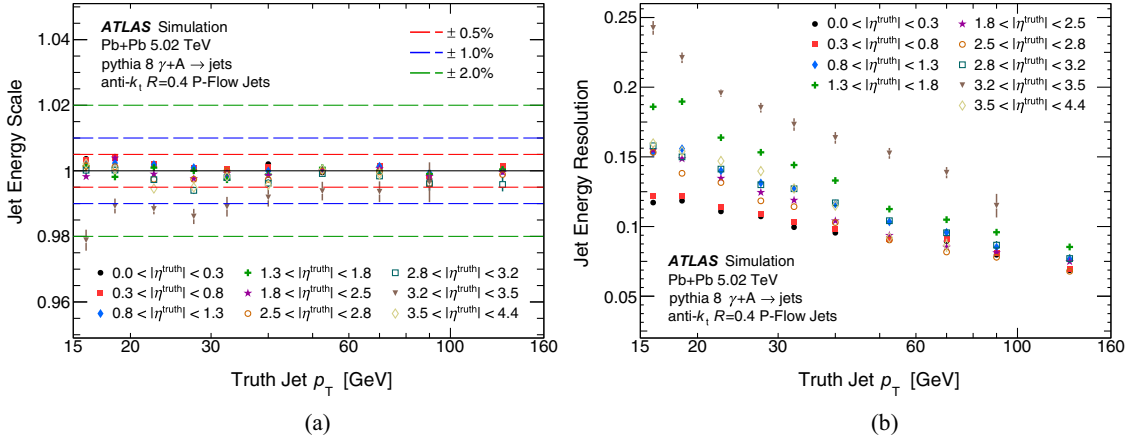


FIG. 5. The (a) mean and (b) standard deviation of jet response distributions as a function of p_T^{true} for different $|\eta^{\text{true}}|$ intervals. Results are restricted to jets with $15 < p_T^{\text{true}} < 160$ GeV. The red and blue dashed lines in (a) mark the 0.5% and 1% levels of closure, respectively.

C. Jet system kinematic variables

This analysis in this paper relies on the measurement of the kinematics of the outgoing system of N jets resulting from hard-scattering processes initiated by photons. The scalar transverse momentum sum, H_T , is defined as

$$H_T \equiv \sum_i p_{Ti}, \quad (2)$$

while the N -jet system mass and rapidity are calculated as

$$m_{\text{jets}} \equiv \left[\left(\sum_i E_i \right)^2 - \left| \sum_i \vec{p}_i \right|^2 \right]^{1/2}, \quad (3)$$

$$y_{\text{jets}} \equiv \frac{1}{2} \ln \left(\frac{\sum_i E_i + \sum_i p_{zi}^*}{\sum_i E_i - \sum_i p_{zi}^*} \right). \quad (4)$$

In the equations above, i runs over all measured jets in an event that satisfy $p_T^{\text{jet}} > 15$ GeV and $|\eta^{\text{jet}}| < 4.4$. E and \vec{p} represent jet energies and momentum vectors, respectively, and p_z represents the longitudinal component of the jet momentum. The signs of p_z^* are chosen to be positive in the photon-going direction. As a result, the y_{jets} values are signed such that negative (positive) y_{jets} values correspond to the jet system being shifted towards the nuclear (photon) direction.

Neglecting effects from initial-state parton showers of incoming quarks and gluons and final-state particles not included in the jet reconstruction, the quantities,

$$z_\gamma \equiv \frac{m_{\text{jets}}}{\sqrt{s_{\text{NN}}}} e^{+y_{\text{jets}}}, \quad (5)$$

$$x_A \equiv \frac{m_{\text{jets}}}{\sqrt{s_{\text{NN}}}} e^{-y_{\text{jets}}}, \quad (6)$$

correspond to fractions of the beam momentum carried by the partons in the emitted photon and struck nucleus, respectively. More generally, these quantities provide physical observables that are strongly correlated with the initial parton kinematics. In direct processes, in which the photon participates directly in the hard scattering, z_γ corresponds to the deep-inelastic scattering variable y .

D. Event selection

Events used in the measurement were recorded during stable running conditions of the LHC and meet standard data-quality criteria [62]. For the nominal analysis, events are must satisfy the $0nXn$ condition and contain at least two jets with $p_T^{\text{jet}} > 15$ GeV and $|\eta^{\text{jet}}| < 4.4$. For events that have at least one jet within the acceptance of the ID, a reconstructed primary vertex [63] is required. To reduce the contribution of events where jets produced in the hard scattering fail event selections or where the hadronic underlying event contributes additional jets, the mass of the jet system must satisfy $0.9H_T < m_{\text{jets}} < 4H_T$. This selection was optimized by studying the kinematic edges in x_A and z_γ as a function of H_T and choosing boundaries that approximately match those introduced by single-jet requirements.

To suppress hadronic Pb + Pb interactions that pass the $0nXn$ requirement, the sum of gaps in the photon-going direction, $\sum_\gamma \Delta\eta$, must satisfy $\sum_\gamma \Delta\eta > 2.5$. To suppress jet production from $\gamma\gamma$ or diffractive photoproduction processes, an edge gap requirement is imposed in the nuclear-going direction: $\Delta\eta_A < 3$. To suppress background from $\gamma + \gamma \rightarrow e^+e^-$ pairs, the total sum of gaps, $\sum \Delta\eta$, is required to be less than 9. Additional event cleaning requirements are applied to remove backgrounds [64] that result from upstream interactions of lead ions, from beam-halo muons passing through the detector, or from events whose calorimeter measurements are significantly distorted

TABLE II. Jet and event selections applied in the measurement. The event cleaning requirements are discussed in Sec. IV D. E_{0n} and E_{Xn} are the ZDC energies on either side of the ATLAS detector, which determine the photon-going and nucleus-going directions.

Jet	Event
$p_T^{\text{jet}} > 15 \text{ GeV}$	ZDC $0nXn$: $E_{0n} < 1 \text{ TeV}$ and $E_{Xn} > 1 \text{ TeV}$
$ \eta^{\text{jet}} < 4.4$	$N_{\text{jet}} \geq 2$
	$0.9H_T < m_{\text{jets}} < 4H_T$
	$\sum_{\gamma} \Delta\eta > 2.5$, $\Delta\eta_A < 3$, and $\sum \Delta\eta < 9$

by collisions occurring in bunch crossings preceding the crossing of interest. Backgrounds from upstream interactions are removed by rejecting events with more than one vertex, and by requiring consistency between the numbers of tracks and topoclusters within the angular acceptance of the ID. Beam-halo muon backgrounds are removed via vetoes on jets measured at large time delays relative to the bunch crossing. Events distorted by prior collisions are removed by rejecting events where significant regions of the calorimeter record negative energy signals, which are characteristic of this distorted response.

The jet kinematic and event-level selections applied in the analysis are summarized in Table II. Events passing these selections are referred to in the remainder of this paper as UPC $\gamma + A \rightarrow$ jets events. While events are selected using a gap requirement, an efficiency correction is applied for this selection, so the gap requirement is not part of the fiducial definition and should not be applied for theoretical comparisons to the measured cross sections.

The impact of the gap selection on the analysis is demonstrated in Fig. 6, which shows the correlation between the multiplicity of charged tracks, N_{ch} , and $\sum_{\gamma} \Delta\eta$. N_{ch} is defined as the number of reconstructed

tracks with $|\eta^{\text{tr}}| < 2.5$ and $p_T^{\text{tr}} > 0.2 \text{ GeV}$. In particular, events with small or zero $\sum_{\gamma} \Delta\eta$ have a very broad N_{ch} distribution as these events result primarily from hadronic interactions in which the particle production spans the full ID acceptance. In contrast, events with larger $\sum_{\gamma} \Delta\eta$ have much smaller multiplicities (even after accounting for the reduced geometrical acceptance), which is consistent with the expected behavior for photonuclear interactions, where hadronic production is primarily backward and partially or fully outside the acceptance of the ID.

V. ANALYSIS

This section presents the methods used to derive UPC $\gamma + A \rightarrow$ jets cross sections from the analysis components described in Secs. III and IV. First, the inefficiencies arising from the application of sample selection requirements are corrected for. Then, residual background contamination is constrained via detailed studies of the rapidity gap distributions, and the resulting jet kinematics are validated by comparison with expectations from MC simulations. Finally, three-dimensional cross section distributions are produced in two sets of jet kinematic variables and unfolded to correct for reconstruction effects.

A. Efficiency corrections

Multiple corrections are applied to the data to account for inefficiencies arising from triggers, gap requirements, and EM pileup. Each of these sources is described below. For other selections described in Sec. IV D but not listed in this section, including the $\sum \Delta\eta < 9$ requirement and event cleaning selections, the associated efficiency corrections are considered to be negligible since they remove no events from the MC sample.

Potential trigger inefficiencies arise at L1 from the ZDC $0nXn$ and minimum $\sum E_T$ requirements. Studies of the ZDC trigger indicate it has an inefficiency of less than

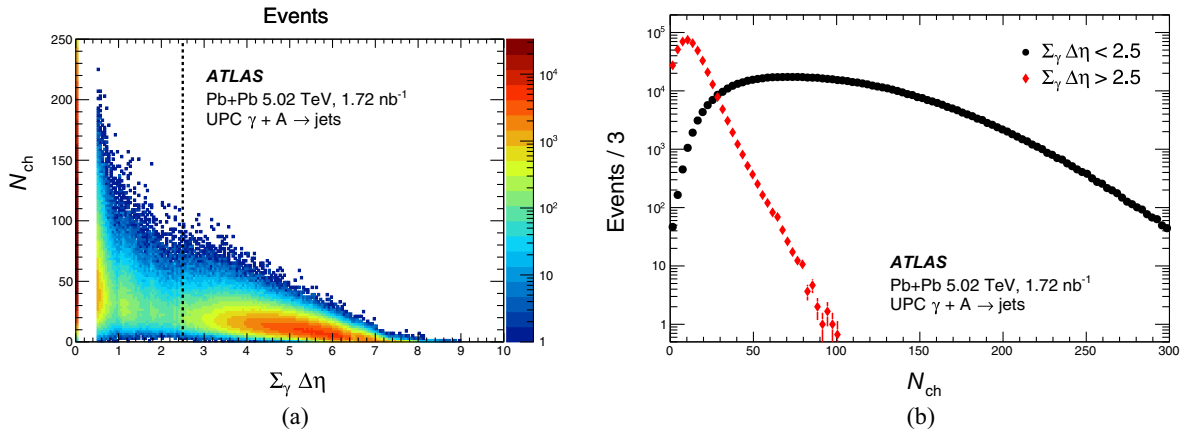


FIG. 6. (a) The distribution of charged track multiplicity, N_{ch} , versus the sum of gaps in the photon-going direction, $\sum_{\gamma} \Delta\eta$. (b) The distribution of N_{ch} for events passing and failing the $\sum_{\gamma} \Delta\eta > 2.5$ requirement. The distributions are obtained by applying all event selections detailed in Table II except the requirement on $\sum_{\gamma} \Delta\eta$.

0.1%, so no correction is required. The efficiency due to the L1 $\sum E_T > 5$ GeV requirement, $\epsilon_{\text{trig}}^{\text{L1}}$, depends on H_T because the jets produced in the $\gamma + A$ processes contribute significantly to $\sum E_T$. The inefficiency arises because the calculation of $\sum E_T$ used in the trigger can differ substantially from the offline values at low total event energy. These differences yield substantially smaller $\sum E_T$ values in the trigger, which results in inefficiency due to the $\sum E_T > 5$ GeV requirement. This inefficiency is a few percent for H_T values less than 40 GeV, less than 1% for H_T values above 40 GeV, and negligible for $H_T > 50$ GeV.

Inefficiencies in the HLT jet trigger arise from an initial filtering step performed in the HLT jet reconstruction. These inefficiencies are only significant near midrapidity due to differences in the energy scale between the particle-flow jets used in the analysis and the calorimeter jets used in the trigger. Single-jet efficiencies, $\epsilon_{\text{trig}}^{\text{jet}}$, are evaluated separately for the 10 and 20 GeV thresholds as a function of $|\eta^{\text{jet}}|$ and p_T^{jet} , and a per-event jet trigger efficiency correction is obtained using

$$C_{\text{trig}}^{\text{jet}} = \frac{1}{1 - \prod_i (1 - \epsilon_{\text{trig}_i}^{\text{jet}})}, \quad (7)$$

where i runs over the jets—usually two—in the final state. Since the jet trigger requires only a single jet, the event-level efficiency is much higher than the single-jet efficiency, due to the possibility of any jet satisfying the trigger requirement. The inefficiency is about 10% for H_T values less than 35 GeV, less than 2% for H_T values above 35 GeV, and negligible for $H_T > 40$ GeV. No trigger efficiency correction is applied to the MC simulation sample since a trigger is not required to select its events.

The event selection efficiency, ϵ_{evt} , is computed as a function of the complete set of particle-level kinematic variables used to characterize the final state, either $(y_{\text{jets}}, m_{\text{jets}}, H_T)$ or (x_A, z_γ, H_T) . The efficiency is evaluated using the portion of the MC $\gamma + A$ sample that falls within the UPC $\gamma + A \rightarrow$ jets acceptance defined in the previous section, and is separately tabulated for each of the kinematic intervals defined in Table I. The event selection efficiencies, ϵ_{evt} , account for losses of events due to the application of both nonphysics background requirements and gap requirements. The migration from truth to reconstructed values in the measured kinematic variables is corrected as part of the unfolding procedure and does not contribute to ϵ_{evt} . It is important to note that, although events are selected using gap requirements, they are corrected to a fiducial cross section definition without any gap selection. Thus, when comparing the results of this measurement to theoretical calculations, the theoretical comparison should not have any gap selections applied.

Because the non-physics background requirements cause negligible loss of MC $\gamma + A$ events, ϵ_{evt} mainly accounts for losses due to the gap selections, and these are dominated

by the $\sum_\gamma \Delta\eta > 2.5$ requirement. For events lying well within the kinematic acceptance, the losses due to the gap selections arise primarily from detector response and imperfect correspondence between particle-level and reconstructed $\sum_\gamma \Delta\eta$ or $\Delta\eta_A$ values. However, near the edge of the fiducial acceptance, the event selection efficiency also accounts for the loss of some particle-level events within the fiducial acceptance. As a result, the efficiency correction has the largest impact near the acceptance edge or for large values of z_γ and y_{jets} where the jets restrict the range of $\sum_\gamma \Delta\eta$. The efficiency correction is typically 10–20% in the highest z_γ interval measured, $0.015 < z_\gamma < 0.027$. In the next-highest interval, the correction is typically 5–10% and is less than 1% in other z_γ intervals.

The $0nXn$ requirement introduces an inefficiency due to the presence of EM pileup where independent dissociative Pb + Pb collisions, occurring in the same bunch crossing as an event of interest, produce neutrons in the photon-going direction of the $\gamma + A \rightarrow$ jets event. The rate at which these processes occur is estimated using the single EM dissociation cross section, which is used to calculate the per-event probability that an event is lost due to EM pileup following the procedure used in Refs. [26,27]. The correction, C_{EM} , averaged over the full dataset, is 1.070 ± 0.003 and is independent of the $\gamma + A \rightarrow$ jets kinematics. It is evaluated and applied event-by-event using the luminosity for the associated bunch crossing measured by ATLAS [65].

The corrections described above are combined into a single correction per event,

$$C = \frac{1}{\epsilon_{\text{trig}}^{\text{L1}} \epsilon_{\text{evt}}} \times C_{\text{trig}}^{\text{jet}} \times C_{\text{EM}}, \quad (8)$$

which is applied to every event included in the analysis, resulting in a corrected yield, N_{corr} , which is used to populate reconstructed kinematic distributions prior to unfolding.

B. Backgrounds

Backgrounds to this measurement arise primarily from hadronic or photon-induced processes that mimic some part of the signature of inclusive $\gamma + A$ hard-scattering events. A key element of backgrounds arising from photon-induced processes is independent nuclear breakup via Coulomb excitation (Breakup), which can cause processes that would otherwise have a $0n0n$ topology to satisfy the $0nXn$ selection. Additionally, the possibility is considered that the struck nucleus may not always emit neutrons (Non-Breakup). Either of these two possibilities, Breakup or Non-Breakup, allow for contamination to occur between neutron topologies, causing processes that do not typically have a $0nXn$ topology to contribute backgrounds to this measurement. Three such physical processes provide

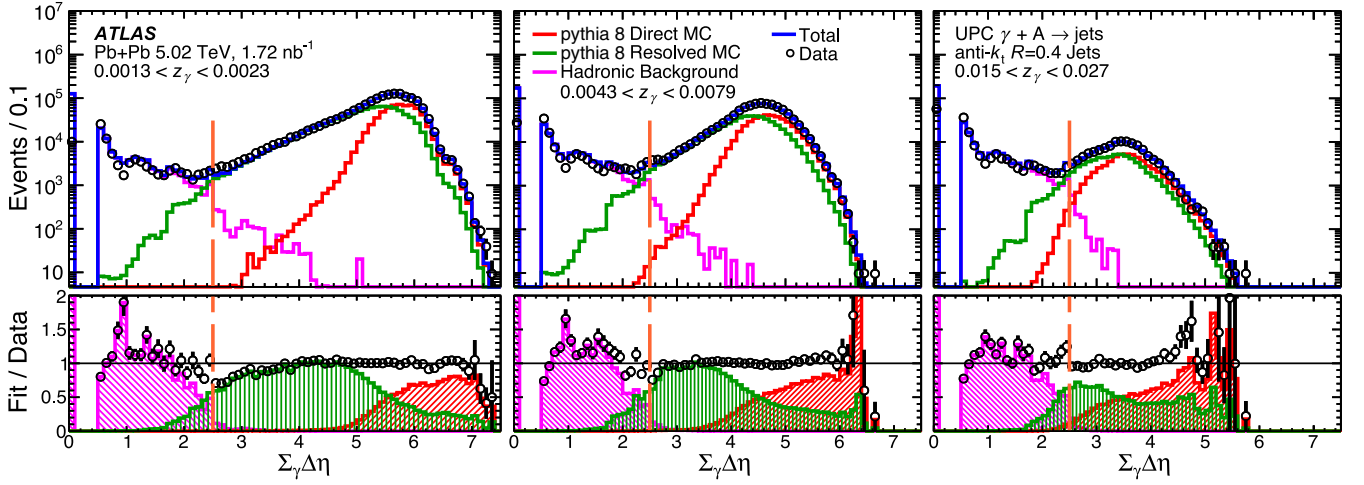


FIG. 7. Template fits of the $\sum_{\gamma} \Delta\eta$ distributions for several bins in z_{γ} , with nominal analysis selections applied. The PYTHIA8 Direct and Resolved MC samples provide the two contributions to the signal, and the hadronic background template is derived from a fitted combination of MC simulation and pp data. The bottom panel shows the ratio of the template fit results to the data in open markers and the ratio to each template component as the hatched bands. The orange dashed line denotes the nominal gap selection.

backgrounds sufficiently large to require a dedicated veto: hadronic Pb + Pb collisions, $\gamma + IP \rightarrow$ jets (diffractive photoproduction of jets), and $0n0n \gamma + A \rightarrow$ jets. Backgrounds resulting from these processes cannot be fully removed via ZDC selections, so rapidity gap selections are employed to reject them. Figures 7, 8, and 9 illustrate the efficacy of these selections.

The gap requirement in the photon-going direction ($\sum_{\gamma} \Delta\eta > 2.5$) mitigates the most prominent background, hadronic Pb + Pb collisions with a Non-Breakup condition. This background yields the steeply falling distribution at small $\sum_{\gamma} \Delta\eta$ visible in Fig. 7, and it is modeled

phenomenologically using a template distribution derived from the pp data and PYTHIA8 MC simulation. This description is expected to be imperfect due to the different ratios of hadronic and diffractive processes in pp and Pb + Pb collisions. However, the measurement itself is insensitive to the modeling of this background given the low rate of contamination shown in Fig. 9. Since the background contamination rates are so small, no subtraction is applied and no additional uncertainty is considered on the measurement resulting from imperfections in these template fits.

The gap requirement in the nucleus-going direction ($\Delta\eta_A < 3$) is employed to remove backgrounds resulting

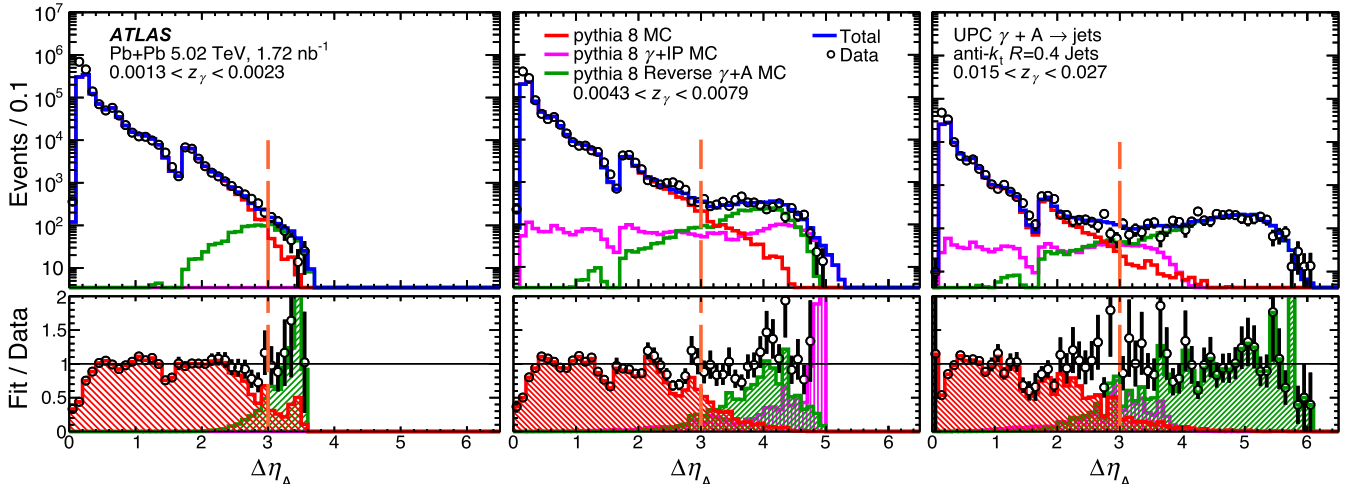


FIG. 8. Template fits of the $\Delta\eta_A$ distributions for several bins in z_{γ} , with nominal analysis selections applied. The PYTHIA8 MC sample corresponds to photonuclear MC sample, the $\gamma + IP$ sample corresponds to the coherent photodiffractive MC sample, and the Reverse $\gamma + A$ MC sample corresponds to $\gamma + A$ MC sample with its coordinate system inverted. The bottom panel shows the ratio of the template fit results to the data in open markers and the ratio to each template component as the hatched bands. The orange dashed line denotes the nominal gap selection.

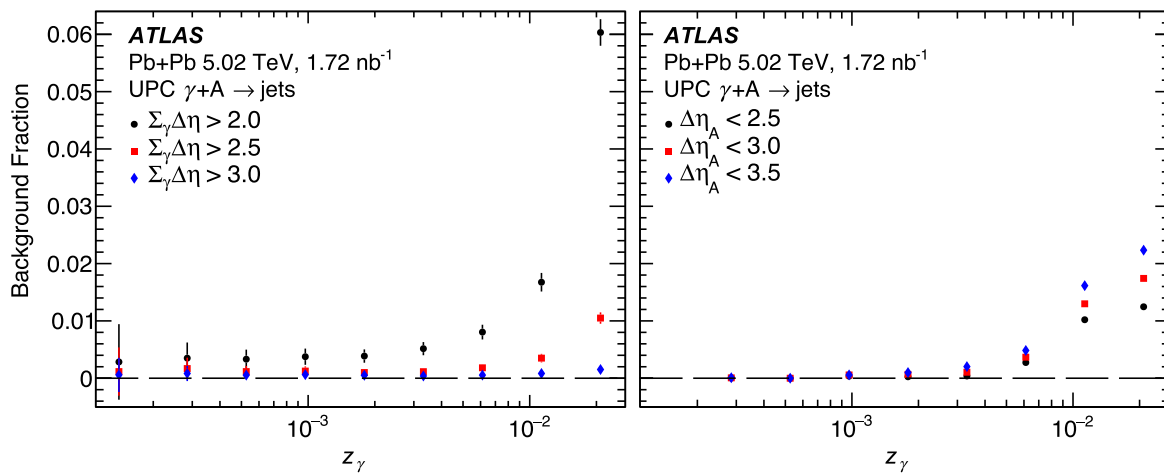


FIG. 9. Residual background fractions for several different possible gap selections, extracted from template fits of the $\sum_{\gamma} \Delta\eta$ and $\Delta\eta_A$ distributions. The red markers indicate the nominal selections which are applied in this measurement, and the other markers show variations demonstrating the sensitivity of the background rate to the choice of selection. Error bars represent statistical uncertainties only.

from two sources: $\gamma + IP \rightarrow$ jets and Non-Breakup $\gamma + A \rightarrow$ jets, both of which may contaminate the $0nXn$ sample in the Breakup case. The $\gamma + IP \rightarrow$ jets background is simulated using a PYTHIA8 MC sample where the pomerons are emitted coherently by the entire nucleus, softening the pomeron energy spectrum. For the Non-Breakup $\gamma + A \rightarrow$ jets background, the contamination is only important when uncorrelated nuclear breakup causes the photon-going direction to be misidentified by the ZDCs, manifesting as “reverse” $\gamma + A \rightarrow$ jets events. These backgrounds are modeled in template fits using a PYTHIA8 $\gamma + A \rightarrow$ jets sample, with its coordinate system inverted such that the photon-emitting nucleus moves in the negative direction. A template fit to the $\Delta\eta_A$ distribution is shown in Fig. 8, demonstrating the good description these background models provide for the observed distributions. Figure 9 shows the background contamination at different z_{γ} values for several edge gap requirements, including the region used for the event selection ($\Delta\eta_A < 3$ and $\sum_{\gamma} \Delta\eta > 2.5$). This figure demonstrates that the rate of background contamination is small enough to be neglected, so no subtraction is applied to the data. Studies of Non-Breakup $\gamma + A \rightarrow$ jets processes in a separate $0n0n$ sample indicate that they occur at a rate of about 4% of the $0nXn$ case. Since this rate is small compared to the total uncertainties on the measurement described in Sec. VI, no attempt is made to correct for it.

The different shapes of the direct and resolved photon processes seen in Fig. 7 can be used in a template fit to extract the rates of these processes in data as a function of z_{γ} , thereby allowing a comparison with the predictions from the PYTHIA8 MC. The shapes of the $\sum_{\gamma} \Delta\eta$ templates derived from PYTHIA8 are from LO modeling and could differ from data or from next-to-leading-order (NLO)

calculations. However, the difference between the LO and NLO cross sections may be primarily a normalization effect. The good agreement between data and the template fits suggests that this may be the case. The template fit then provides useful input on the accuracy of PYTHIA8 in predicting the relative contributions from direct and resolved processes. Figure 10 shows the fraction of direct $\gamma + A$ processes obtained from the $\sum_{\gamma} \Delta\eta$ template fits. In general, the data show a slightly smaller fraction of direct processes than PYTHIA8 at small z_{γ} and a slightly higher fraction at larger z_{γ} , with better agreement at large H_T .

C. Data-MC comparison

With the application of the corrections described above and a data-driven correction for breakup of the photon-emitting nucleus (see Sec. VII), distributions of $\gamma + A$ events from the data can be compared to the same distributions obtained from the PYTHIA8 MC sample. This is done by scaling differential cross sections obtained from PYTHIA8 by the integrated luminosity used in the measurement and comparing the result to the differential distribution of N_{corr} , the corrected yields, in the data. The gap selections used in the analysis are not applied to the PYTHIA8 sample since the data are already corrected for effects described in Sec. VA, but the same requirements on reconstructed jets are applied and the kinematic quantities for PYTHIA8 are obtained from reconstructed jets.

Figure 11 shows distributions of the jet multiplicity and the azimuthal angle separation, $\Delta\phi$, between the two jets having the highest p_T^{jet} values in the event. The PYTHIA8 prediction systematically underestimates the rate for events with more than two jets, likely because it only includes LO hard-scattering matrix elements. This aspect of PYTHIA8 is

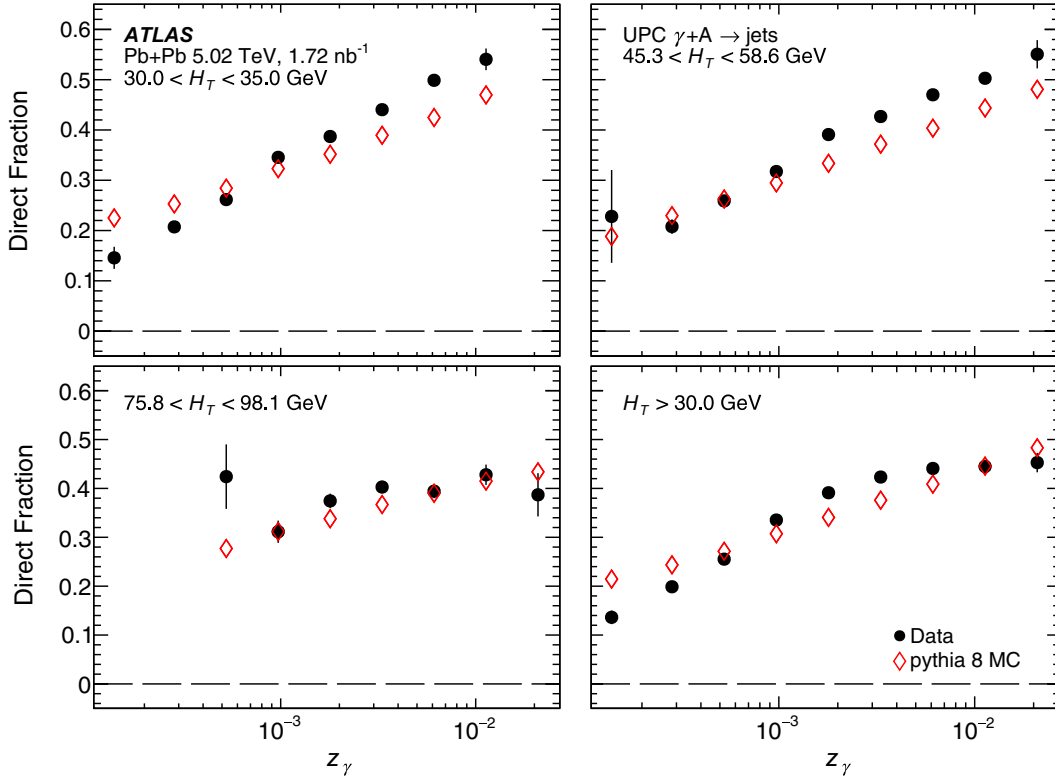


FIG. 10. The fraction of events resulting from direct photon processes, extracted from template fits of the $\sum_{\gamma} \Delta\eta$ distributions, compared to the results from PYTHIA8 using CJKL photon PDFs. Several different intervals in H_T are shown. Error bars represent statistical uncertainties only.

most likely responsible for the disagreement in the $\Delta\phi$ distribution for $\Delta\phi \lesssim 2.5$ rad.

Figure 12 shows a comparison of y_{jets} and H_T distributions between PYTHIA8 and data with corrections as

described in Sec. VA. In both MC samples and data, the y_{jets} distributions are shifted toward the nucleus-going direction because the typical photon energy is much smaller than that of the parton from which it scatters. The y_{jets}

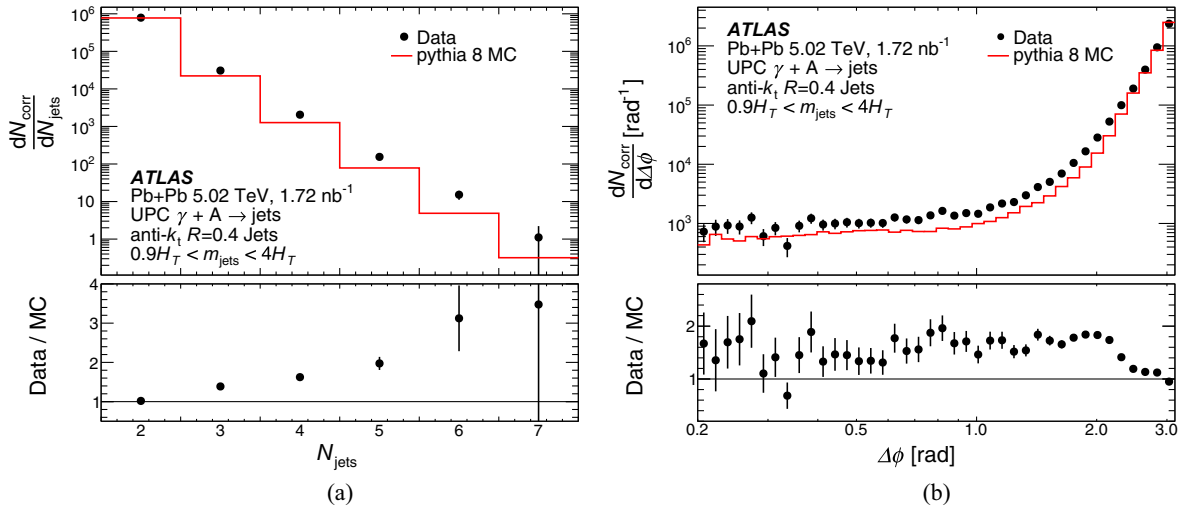


FIG. 11. Comparison of data and MC distributions for UPC $\gamma + A \rightarrow$ jets production, within the fiducial acceptance, for (a) the jet multiplicity and (b) the $\Delta\phi$ of the leading dijet pair. The distributions are shown for reconstructed jet kinematics after applying all event selections and efficiency corrections. The bottom panels show the ratios of the data and MC distributions. The error bars in both panels show statistical uncertainties only.

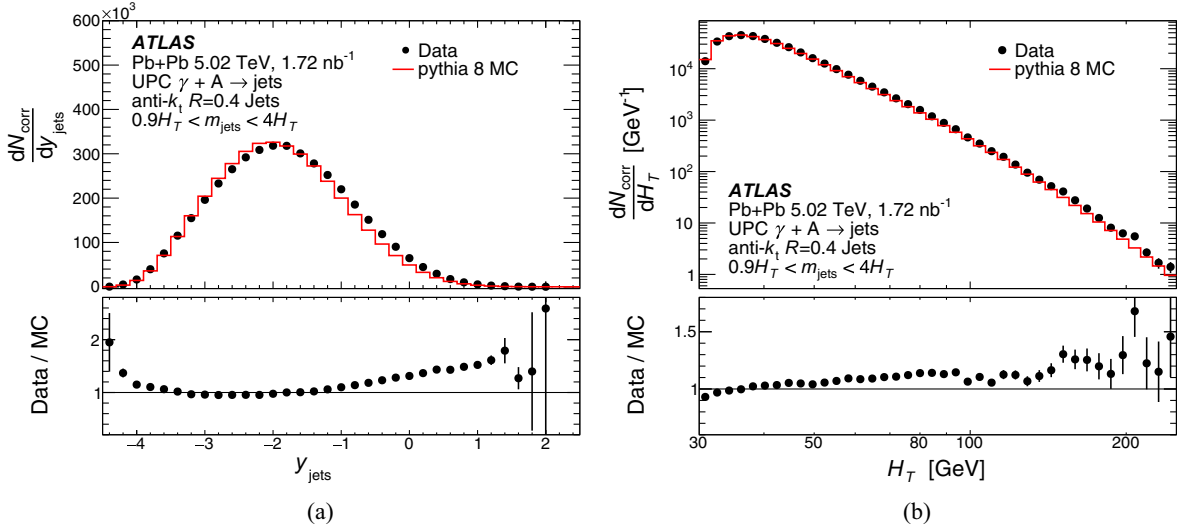


FIG. 12. Comparison of data and MC distributions for UPC $\gamma + A \rightarrow$ jets production, within the fiducial acceptance, for (a) y_{jets} and (b) H_T . The distributions are shown for reconstructed jet kinematics after applying all event selections and efficiency corrections. The bottom panels show the ratios of the data and MC distributions. The error bars in both panels show statistical uncertainties only.

distribution in data appears to be enhanced compared to the MC samples at both backward ($y_{\text{jets}} < -4$) and forward ($y_{\text{jets}} > -1$) y_{jets} values, while the data and MC samples agree well for intermediate values of y_{jets} . Nonetheless, the level of agreement is sufficiently good that PYTHIA8 can be used to evaluate the migration in $(y_{\text{jets}}, m_{\text{jets}}, H_T)$ and (x_A, z_γ, H_T) due to jet response, which is needed to unfold the measured cross sections.

D. Fiducial cross sections

The measured photonuclear jet cross sections, corrected for efficiency before unfolding for detector response, are calculated as

$$\frac{d^3\sigma_{\text{meas}}}{dH_T dy_{\text{jets}} dm_{\text{jets}}} \equiv \frac{1}{\mathcal{L} \Delta V(y_{\text{jets}}, m_{\text{jets}}, H_T)} \Delta N_{\text{corr}}, \quad (9)$$

$$\frac{d^3\sigma_{\text{meas}}}{dH_T dx_A dz_\gamma} \equiv \frac{1}{\mathcal{L} \Delta V(x_A, z_\gamma, H_T)} \Delta N_{\text{corr}}, \quad (10)$$

where ΔN_{corr} represents the corrected number of $\gamma + A \rightarrow$ jets events measured within the acceptance volume, ΔV is the geometric acceptance volume as a function of its three-dimensional bin defined in Table I, and \mathcal{L} is the integrated luminosity. The calculation of ΔV is described in greater detail in Appendix B. To account for the different p_T^{jet} and $|\eta^{\text{jet}}|$ acceptances and the different sampled luminosities of the jet triggers, the cross sections are separately evaluated in different intervals of leading and subleading jet p_T^{jet} and $|\eta^{\text{jet}}|$ and then summed over the fiducial acceptance of those variables.

To visualize the kinematic coverage of the measurement, two-dimensional (2D) cross sections are obtained from Eqs. (9) and (10) by integrating the third variable over the fiducial acceptance of the measurement. The 2D cross sections are evaluated using finer binning than that given in Table I, in order to better illustrate the kinematic coverage of the measurement. The results are presented in Fig. 13 for both sets of kinematic variables, scaled by the integrated luminosity to provide the corrected number of events. The left column shows the three possible sets of 2D cross sections using $(y_{\text{jets}}, m_{\text{jets}}, H_T)$ and the right column shows those using (x_A, z_γ, H_T) .

E. Unfolding procedure

The effects of detector response on the measured cross sections are corrected using an iterative Bayesian unfolding procedure [66–68], as implemented using the ROOUNFOLD software package [69]. The procedure accounts for both bin migration within the fiducial region and migration into and out of the fiducial region via a response matrix populated from the MC sample, which maps between the reconstructed and truth-level kinematic variables. This procedure works by unfolding the measured data using an assumed prior distribution as the true distribution. The output of the unfolding procedure is a set of posterior weights, which are used to construct an updated estimate for the true distribution. The unfolding is performed in three dimensions to properly account for bin migration effects that are correlated across one or more dimensions. These effects arise since the detector response in one unfolding variable is correlated with the value of other variables. The $(y_{\text{jets}}, m_{\text{jets}}, H_T)$ and (x_A, z_γ, H_T) distributions are unfolded separately. The performance of the unfolding procedure

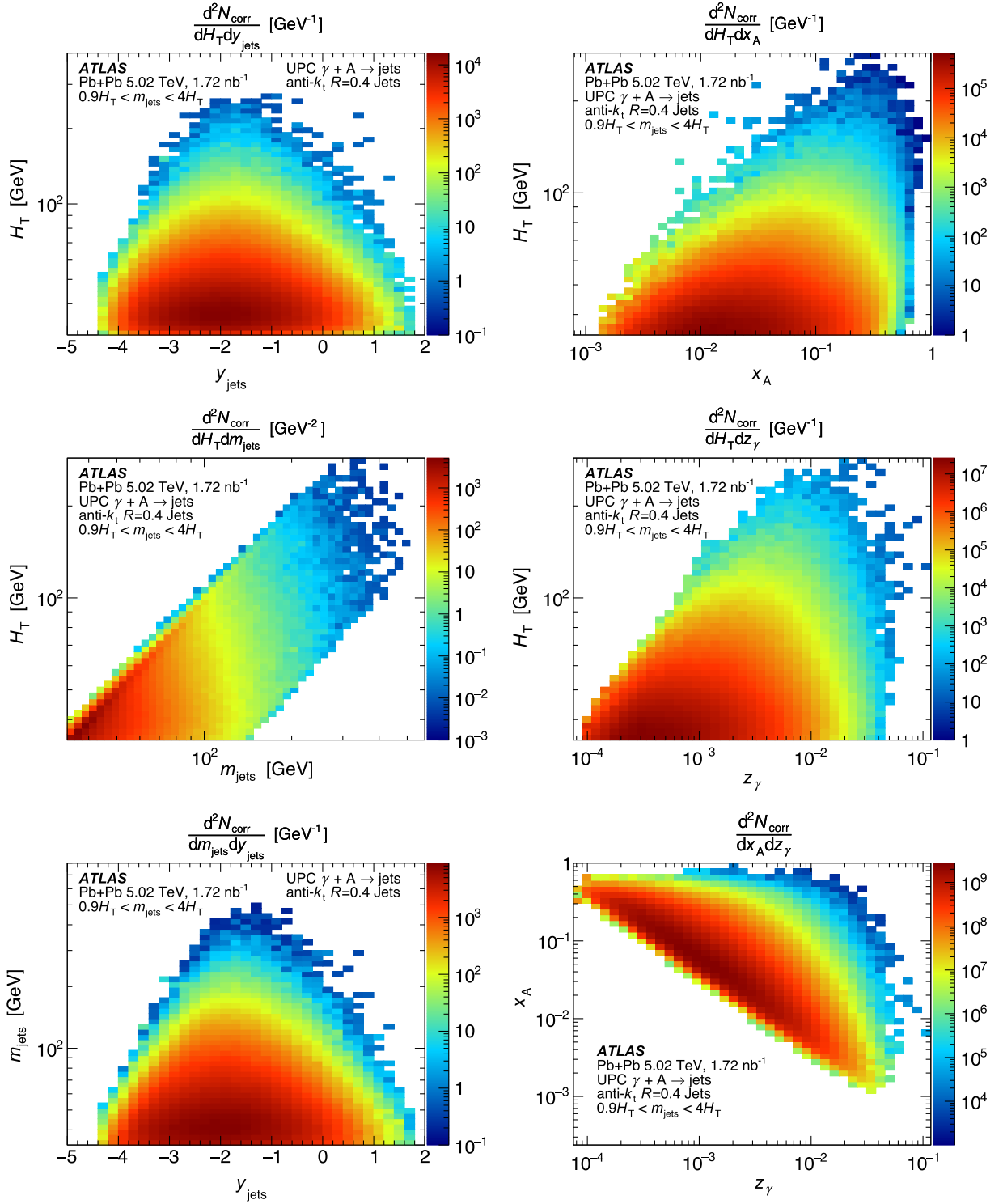


FIG. 13. Two-dimensional measured differential distributions of N_{corr} for $\gamma + A \rightarrow \text{jets}$ production in Pb + Pb UPC interactions obtained by integrating the three-dimensional cross sections obtained from Eqs. (9) and (10) over the acceptance of the third variable. The left column shows results using $(y_{\text{jets}}, m_{\text{jets}}, H_T)$ and the right column results using (x_A, z_γ, H_T) . These results are not unfolded for detector response.

was validated through studies of its efficiency, purity, and closure in simulated events.

The number of iterations used in the iterative Bayesian unfolding procedure must be specified. As the number of iterations is increased, the sensitivity of the unfolded results to the prior is reduced but the statistical uncertainties of the results typically increase. The residual sensitivity is evaluated by unfolding with an alternative prior, and is used to evaluate the systematic uncertainty discussed in Sec. VI. The number of iterations is chosen by first considering the general stability of the unfolded distributions under additional iterations and then by quantitatively comparing the systematic uncertainty from the residual sensitivity to the prior with the statistical uncertainty. The unfolded results for both sets of kinematic variables are based on five iterations.

Statistical uncertainties on the unfolded results are evaluated in the data by studying the impact of 1000 possible stochastic variations generated from the input distributions. The variations are each unfolded in the same manner as the data, and the statistical covariance is computed for the unfolded cross section for each pair of bins. Statistical uncertainties due to possible statistical fluctuations in the response matrix are obtained in an analogous fashion by generating alternative samplings of the response distributions.

VI. SYSTEMATIC UNCERTAINTIES

Point-to-point systematic uncertainties are assigned to the data from four different sources: event selection efficiency, JES uncertainty, JER uncertainty, and residual sensitivity to the unfolding prior. The event selection efficiency accounts for improper modeling of the impact of the gap selection when event selection efficiencies are evaluated in PYTHIA8. The JES systematic uncertainties account for the impact of imperfect knowledge of the *in situ* JES calibration on the measured cross sections. The JER uncertainties similarly describe the impact of imperfect knowledge of differences in the JER between data and MC simulation. The systematic uncertainty for residual sensitivity to the unfolding prior accounts for the residual dependence on the prior used in constructing the response matrices due to the finite number of iterations used in the Bayesian unfolding procedure. Additional uncertainties due to the luminosity measurement and correction for EM pileup, which are fully correlated across all bins, are propagated to the result. Uncertainties due to the trigger efficiency corrections were found to be negligible, due to the already small magnitude of these corrections within the fiducial acceptance of the measurement.

The event selection uncertainties are assessed for both gap requirements ($\Delta\eta_A < 3$ and $\sum_\gamma \Delta\eta > 2.5$), following the same procedure in each case, separately for each selection. Each gap requirement is individually tightened

by 0.5 units and the cross sections are measured with this new event selection. The event selection efficiency estimated in the simulation is also modified for this new selection, and the corrected cross sections are unfolded using the nominal procedure. The resulting cross sections are then compared to the nominal result to extract the uncertainty. By varying the efficiency correction as well, this method assigns uncertainties for the modified event selection efficiency incorrectly accounting for the effect of varying the selection in data, which provides a metric for mismodeling of the efficiency. Uncertainties due to residual backgrounds are neglected, since the rates of these backgrounds are found to be negligible in the studies shown in Sec. VB.

The JES and JER systematic uncertainties are propagated from the uncertainties obtained using the procedure described in Appendix A. For each source of uncertainty on the JES, a nuisance parameter variation is introduced, where the reconstructed p_T^{jet} of each jet in simulation is multiplied by a scale factor as a function of its $|\eta^{\text{jet}}|$ and p_T^{jet} . These nuisance parameter variations are used to construct modified response matrices, where the truth-level jet information is the same, but the varied jets are used to determine the reconstructed kinematics. The cross sections are unfolded with the modified response matrices and compared to the nominal result in order to determine the JES uncertainty for that nuisance parameter.

In the case of the JER, the procedure is similar, except that the jet transverse momenta are smeared as a function of $|\eta^{\text{jet}}|$ and p_T^{jet} according to each nuisance parameter. Additionally, in cases where the *in situ* measurement of the resolution in data is smaller than in the MC sample, it is necessary to smear data distributions instead of the MC response matrices. A pseudodata smearing procedure, where cross section distributions are populated from reconstructed MC events and smeared, rather than directly smearing the data, is applied in order to reduce the impact of statistical fluctuations on the uncertainty. These smeared distributions are unfolded with similarly varied response matrices, and the results are then compared to the nominal unfolded MC distributions, in order to translate fractional uncertainties bin by bin to the nominal cross sections.

The systematic uncertainty for residual sensitivity to the unfolding prior is determined by reweighting the prior distribution in the response matrices in order to match the reconstructed data distribution. The ratios of the reconstructed cross sections between data and MC simulation are evaluated as a function of the three variables used in the unfolding, and the results are smoothed using a Gaussian kernel. The ratios are then used to reweight the response matrix as a function of the truth-level jet kinematics. The cross sections are unfolded with the same number of iterations using these modified response matrices, and

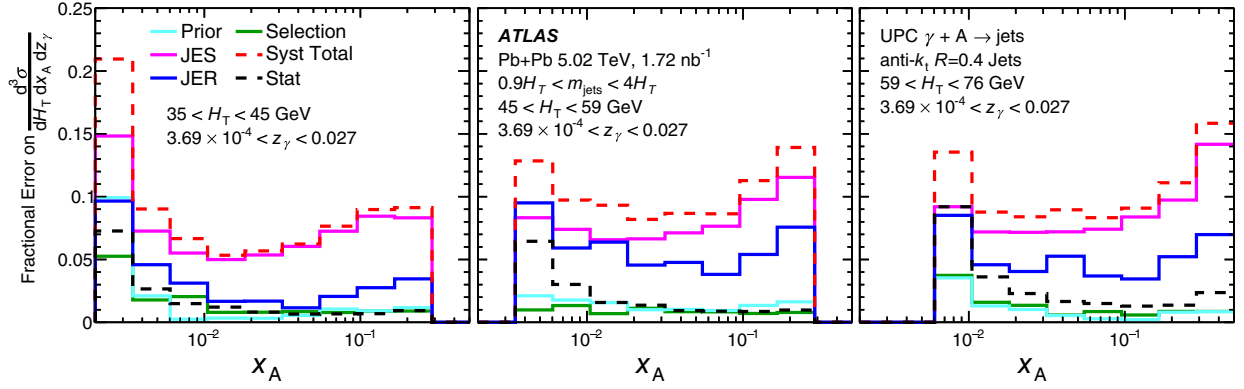


FIG. 14. A breakdown of the different systematic uncertainty contributions as a function of x_A , for a selection of bins in H_T , summed over z_γ .

the results of this procedure are compared to the nominal results in order to derive the systematic uncertainty.

The uncertainty on the integrated luminosity of the data sample is 2.0%. It is derived from the calibration of the luminosity scale using x - y beam-separation scans, following a methodology similar to that detailed in Ref. [65], using the LUCID-2 detector for the baseline luminosity measurements [45]. An additional uncertainty is applied to the measured total cross section due to uncertainty on the rate of EM pileup, which is not correlated with event kinematics. This uncertainty is obtained by varying the Pb + Pb dissociative cross section within its uncertainties, yielding a fractional uncertainty of 0.3%.

A summary of the different sources of systematic uncertainty for a selection of bins in H_T and summed over the full range in z_γ are shown as function of x_A in Fig. 14, demonstrating the contributions from each source of systematic uncertainty, compared to the statistical uncertainty. The statistical uncertainty due to the unfolding response matrix is included in the total statistical uncertainty but is negligible. The *in situ* measurement of the JES typically provides the largest source of systematic uncertainty, but in some regions near the edges of the phase space, the JER uncertainties grow larger. The event selection uncertainties are never dominant, and they are only substantial in the kinematic regions where the jets are near the edge of the photon-going gap (large z_γ , large positive y_{jets}). The sensitivity to the unfolding prior is smaller than the statistical uncertainty in all bins except for at the very edge of the phase space, where the unfolding becomes more difficult to control at the percent level. Additionally, correlations between the bins of the systematic uncertainties are assessed, where each JES or JER nuisance parameter is taken as 100% correlated between bins but uncorrelated with other nuisance parameters. The systematic uncertainty due to the event selection efficiency and sensitivity to the unfolding prior may have some unknown bin-to-bin correlation, so they are conservatively taken as completely uncorrelated bin to bin.

VII. NUCLEAR BREAKUP

In order to provide a useful evaluation of the measured cross sections, the data are compared to particle-level triple-differential cross sections from PYTHIA8. However, because the measurement nominally uses the $0nXn$ condition to identify $\gamma + A$ events, the PYTHIA8 cross sections must first be corrected for the effects of breakup of the photon-emitting nucleus, which can depend on the $\gamma + A$ kinematics, especially z_γ . This section describes how the methods described in Secs. V and VI are applied to the $XnXn$ sample in order to obtain an experimental measurement of the photon-going breakup likelihood. This result is then applied to the PYTHIA8 cross sections in order to allow a comparison with unfolded data.

The fraction of photonuclear jet events without breakup of the photon-emitting nucleus is measured as a function of z_γ using two samples: the nominal analysis $0nXn$ sample and an additional $XnXn$ sample. In the latter sample, the photon-going direction is selected using the side of the detector with the largest $\sum \Delta\eta$. In order to reduce potential background contamination from hadronic processes, a more strict gap requirement, $\Delta\eta_\gamma > 2.5$, is imposed in the photon-going direction for both samples. Studies of the gap distributions in $XnXn$ events indicated that this selection is necessary to achieve sufficient purity to measure $\gamma + A \rightarrow \text{jets}$ events in $XnXn$ collisions. This requirement preferentially removes resolved-photon events, but the probability that the photon-emitting nucleus breaks up is not sensitive to the nature of the hard-scattering process, due to the large separation in energy scales between the hard-scattering and soft photon exchange [39]. An assessment of the acceptance and ϵ_{evt} , separate from the one used in the nominal analysis, is performed for both the $XnXn$ and the corresponding $0nXn$ sample. Corrected cross sections from each sample are then unfolded in a modified three-dimensional binning, providing finer intervals in z_γ , and the fraction of events

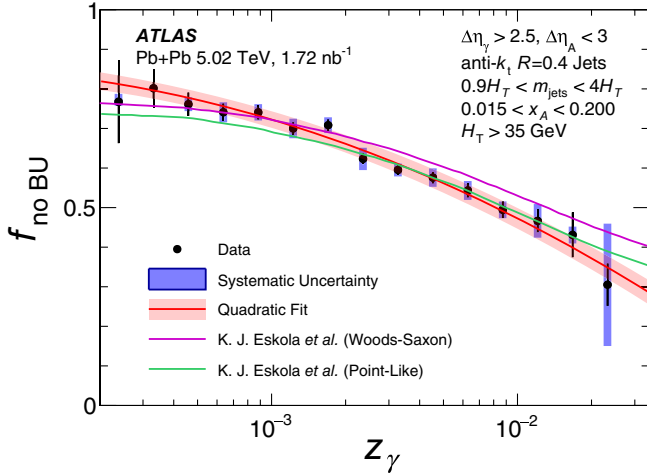


FIG. 15. The fraction of photonuclear jet events passing the fiducial requirements in which the photon-emitting nucleus does not breakup as a function of z_γ . The systematic uncertainties are shown as shaded blue bands, and the error bars are statistical uncertainties. A quadratic fit in $\ln(z_\gamma)$ is shown in red. These results indicate a strong dependence of the breakup rate on z_γ and an overall high rate of breakup due to additional Coulomb interactions, reaching 70% at high z_γ . Results are compared to theoretical calculations from Ref. [70].

which do not breakup is computed from the unfolded cross sections as

$$f_{\text{no BU}} \equiv \frac{d\sigma/dz_\gamma|_{0nXn}}{d\sigma/dz_\gamma|_{XnXn} + d\sigma/dz_\gamma|_{0nXn}}. \quad (11)$$

Full systematic uncertainties are then propagated through the ratio by applying systematic variations to each sample; most of the uncertainties largely cancel in the ratio. Figure 15 shows the measured no-breakup fraction as a function of z_γ . A quadratic fit in $\ln(z_\gamma)$ is used to smooth the variations. The quadratic fit is applied as a correction to theoretical predictions shown in Sec. VIII B as a function of z_γ . The breakup fraction shows a substantial variation with z_γ , which is expected to arise because higher photon energies are more likely at smaller impact parameters, and the probability of additional Coulomb excitations is also correlated with the impact parameter of the collision. Theoretical calculations from Ref. [70] describe the data by modeling the EM breakup probability as a function of impact parameter in a model of NLO $\gamma + A \rightarrow$ jets production, and they are compared to the data in Fig. 15. These calculations describe the measured fraction quite well but no single prediction captures the shape over the full range in z_γ . Since H_T and x_A are much more weakly correlated with impact parameter, no additional dependence on these variables is considered.

VIII. RESULTS

This section provides fully corrected triple-differential cross sections for photon-nucleus collisions with no breakup in the photon-going direction, $\frac{d^3\sigma}{dH_T dx_A dz_\gamma}$ and $\frac{d^3\sigma}{dH_T dy_{\text{jets}} dm_{\text{jets}}}$. Namely, the measured cross-sections obtained from Eqs. (9) and (10) in the kinematic intervals described in Table I are unfolded using the detector response obtained from PYTHIA8 events with full detector simulation, and systematic uncertainties described in Sec. VI are evaluated for each three-dimensional bin. More information about which bins are reported, the calculated mean value of each bin, and the phase-space volume used to define the triple-differential cross section are provided in Appendix B.

In order to separate uncertainties correlated across bins from those that are uncorrelated, the uncertainties of the results shown in this section are represented by three components: statistical, scale, and residual systematic uncertainties. The scale uncertainty is computed by separating out the part of the correlated uncertainty that corresponds to a single rescaling of the entire distribution. This component is taken to be the smallest fractional uncertainty on any single bin in that selection, for each uncertainty that is 100% correlated bin to bin. These scale uncertainties are added in quadrature and represented as a light red band, while the remaining systematic uncertainty is represented as a gray band and the statistical uncertainty is shown in yellow. Although these residual systematic uncertainties do have some correlation, the conservative assumption should be made that they are uncorrelated when interpreting the uncertainties.

A. Sensitivity to nuclear PDF effects

The results presented in this section for UPC $\gamma + A \rightarrow$ jets cross sections are compared to a theoretical calculation from LO PYTHIA8 which was produced using nCTEQ15 WZ + SIH [71] PDFs. While discrepancies may arise between the data and this theory calculation due to other sources, such as higher-order QCD effects or uncertainty on the photon flux, the primary goal of this comparison is to evaluate any inconsistencies that can be attributed to differences in the measured nPDFs. An understanding of the size of these effects and differences between the modifications in competing fits is important in assessing the impact of the data on constraining these effects. Figure 16 shows the ratio of photonuclear jet cross-section calculations between a PDF set with nuclear modifications (nCTEQ15 WZ + SIH, nNNPDF 3.0 [72]) and without modifications (CT18 [73], NNPDF 3.1 [74]). Both the numerator and denominator in these ratios are corrected for small isospin effects arising from differences in the parton content of protons and neutrons. The total uncertainty on the data measurement in these bins is shown for comparison, demonstrating the sensitivity of these data both to nPDF effects of this size and the existing differences in

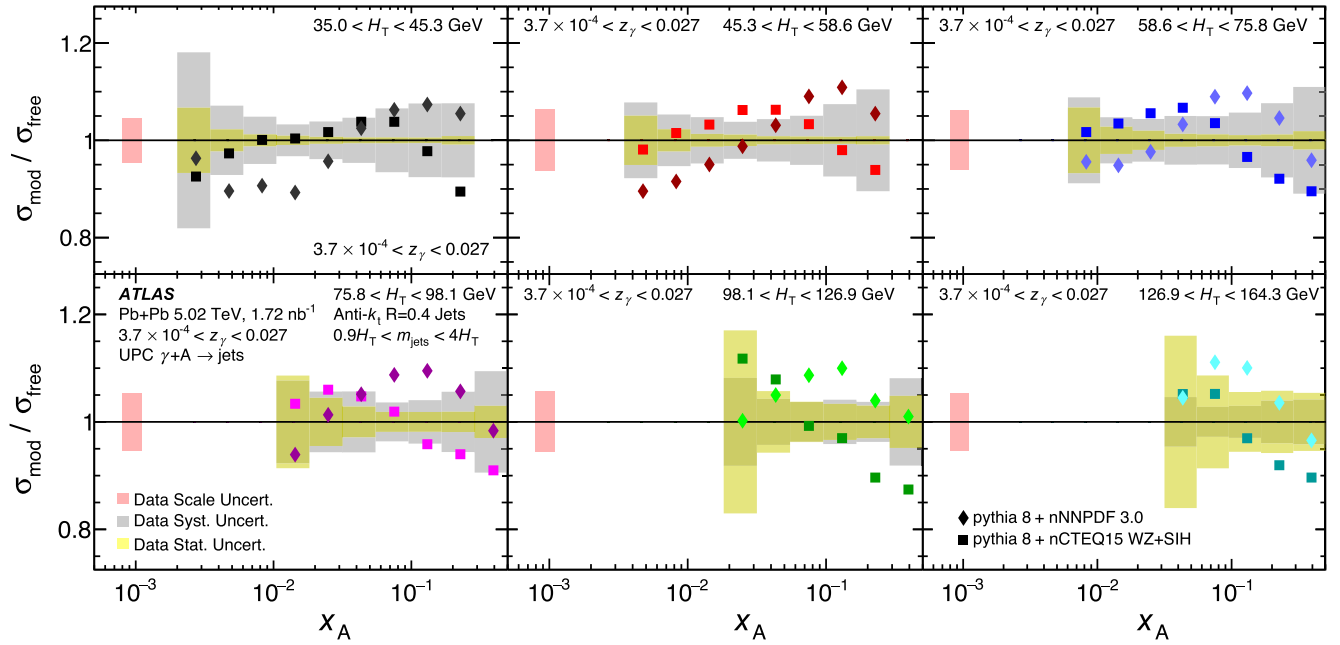


FIG. 16. The impact of nPDF modifications on the photonuclear jet cross section, represented by the ratio of the cross section calculated with modified nPDFs (σ_{mod}) to the cross section for unmodified free nucleon PDFs (σ_{free}). These effects are shown for nCTEQ15 WZ + SIH (squares) and nNNPDF 3.0 (diamonds) fits, where ratios are taken with respect to CT18 and NNPDF 3.1, respectively. Results are integrated over the z_γ range $3.7 \times 10^{-4} < z_\gamma < 0.027$, and each panel shows a separate range in H_T . The total uncertainty on this measurement in each bin is compared to the size of these modifications, where the light red bands show the total scale uncertainty, the gray bands are the quadrature sum of the residual systematic uncertainty, and the yellow bands show the statistical uncertainty.

current nPDF models. Studies of the potential impact of this measurement on nPDF uncertainties [21] indicate that the nPDF uncertainties are typically 10% or larger in this kinematic region, substantially smaller than the point-to-point uncertainty achieved in this measurement.

B. Photonuclear jet cross sections

This section presents the primary results of the analysis described in this paper, the triple-differential cross sections for jet production in Pb + Pb UPCs satisfying the $0nXn$ condition and the fiducial requirements presented in Sec. IV D and Appendix B. The measured cross sections are compared to LO PYTHIA8 cross sections with nCTEQ15 WZ + SIH nPDFs, obtained from the sample described in Sec. III, multiplied by $f_{\text{no BU}}$, the z_γ -dependent probability of no breakup determined empirically from data, as described in Sec. VII. The PYTHIA8 results are represented by the dashed lines. The ratios between the data and the PYTHIA8 calculations for selected intervals in H_T or x_A are shown in the panels below each figure. As these results present the first measurement of photonuclear jet cross sections, no attempt is made to incorporate theoretical uncertainties corresponding to effects such as renormalization scale, nPDFs, or the photon flux, since these uncertainties may be improved in subsequent theoretical comparisons.

The presentation of results begins with cross sections evaluated using $(y_{\text{jets}}, m_{\text{jets}}, H_T)$ which are closely related to the measured jet kinematics. Figure 17 shows cross sections as a function of y_{jets} in different intervals of m_{jets} that have been integrated over the H_T acceptance in each y_{jets} and m_{jets} interval. The comparison with PYTHIA8 + nCTEQ15 WZ + SIH shows a systematic difference as a function of y_{jets} . For small m_{jets} , the cross section in the data is larger than that in PYTHIA8 at forward rapidities and matches the results from PYTHIA8 at backward rapidities, while at larger m_{jets} , the ratio is largely independent of y_{jets} but the theory underpredicts the total cross-section. The difference between data and MC varies with H_T , becoming smaller near the maximum in the y_{jets} distribution with increasing H_T . These effects are also visible in Fig. 18, where the theory underpredicts the data at larger m_{jets} .

In the following figures, the measured cross sections are presented in terms of (x_A, z_γ, H_T) that more closely reflect the kinematics of the partons participating in the hard-scattering process. The results are presented as a function of x_A for different H_T intervals in four z_γ ranges: $0.0023 < z_\gamma < 0.0043$, $0.0079 < z_\gamma < 0.015$, $0.0043 < z_\gamma < 0.0079$, and $0.015 < z_\gamma < 0.027$ in Figs. 19, 30, 20, and 31, respectively, where the latter two figures are shown

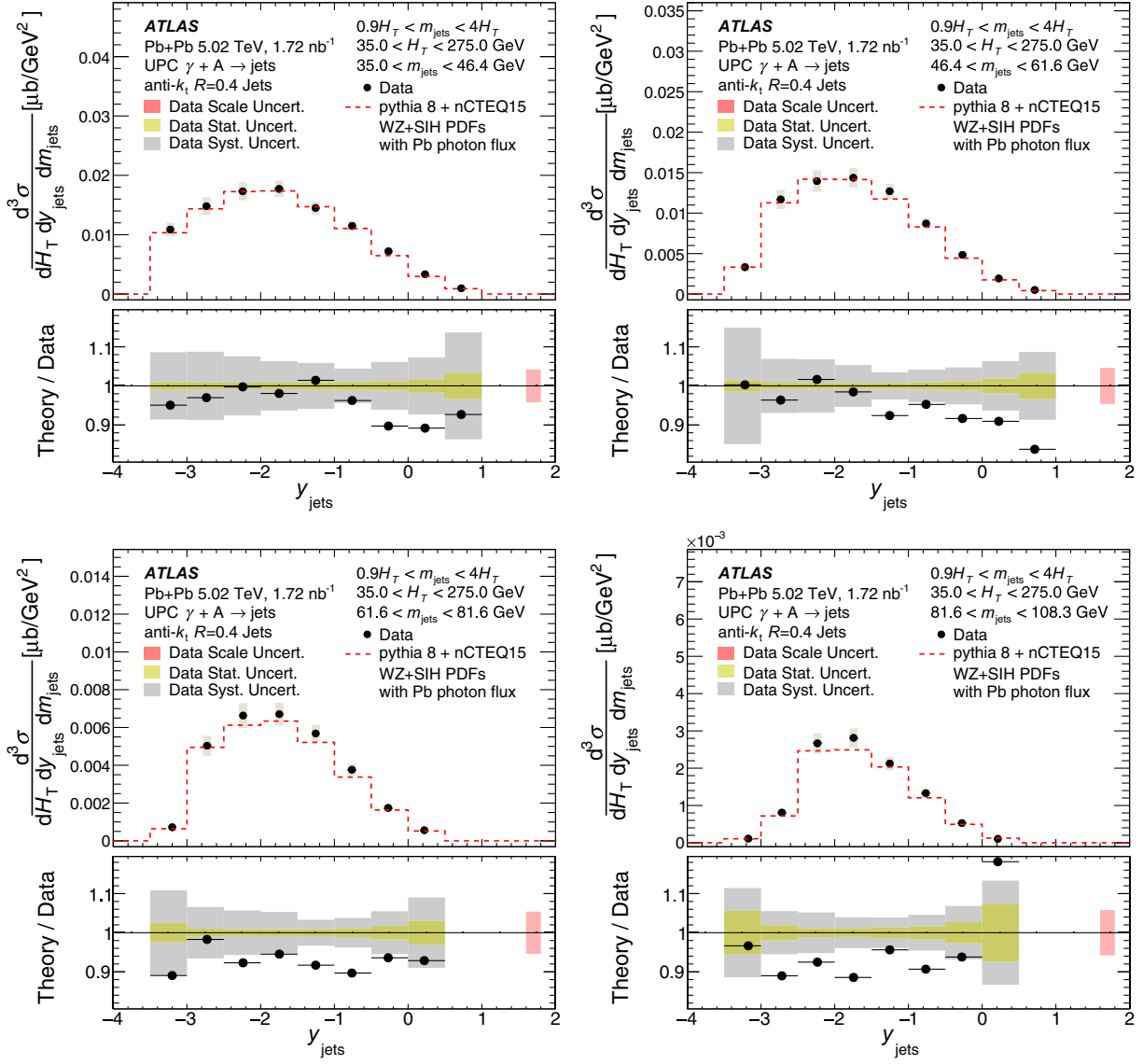


FIG. 17. Triple-differential cross sections, $\frac{d^3\sigma}{dH_T dy_{\text{jets}} dm_{\text{jets}}}$, as a function of y_{jets} , in four m_{jets} intervals with m_{jets} increasing from the top left to the bottom right. The cross sections are shown for the selected intervals in m_{jets} and integrated over the H_T acceptance. For each plot, systematic uncertainties are shown in the upper panel as shaded boxes, while statistical uncertainties shown as vertical lines are usually smaller than the size of the markers. A theoretical comparison is shown to cross sections computed using PYTHIA8 with nCTEQ15 WZ + SIH PDFs, a photon flux from STARLIGHT, and a z_γ -dependent data-driven breakup fraction. The bottom panels show the ratio between the theory prediction and the data. The light red bands in the ratio panels are the quadrature sum of scale uncertainties on the cross section, while the gray band shows the residual systematic uncertainty. The yellow band shows the point-to-point statistical uncertainty.

in Appendix C. Figure 21 demonstrates the impact of integrating over the full range in z_γ . The cross sections in the different H_T intervals are shown scaled by different powers of ten to allow them to be presented in the same figure. Due to the correlation of the acceptance in x_A with z_γ , measuring individual z_γ intervals illustrates the role of the nPDFs. These individual intervals also allow for a more robust separation of correlated systematic uncertainties.

The breakup-adjusted cross sections provide substantial information about differences between the data and PYTHIA8, where the uncertainties on the measurement are substantially smaller than the existing nPDF uncertainties. Broadly, the data suggest that the nPDFs in nCTEQ are too small at lower H_T and lower x_A , but that the agreement improves at higher x_A . From the lower z_γ intervals, it can be observed that the cross section in the antishadowing region from PYTHIA8 + nCTEQ agrees with the data, whereas at

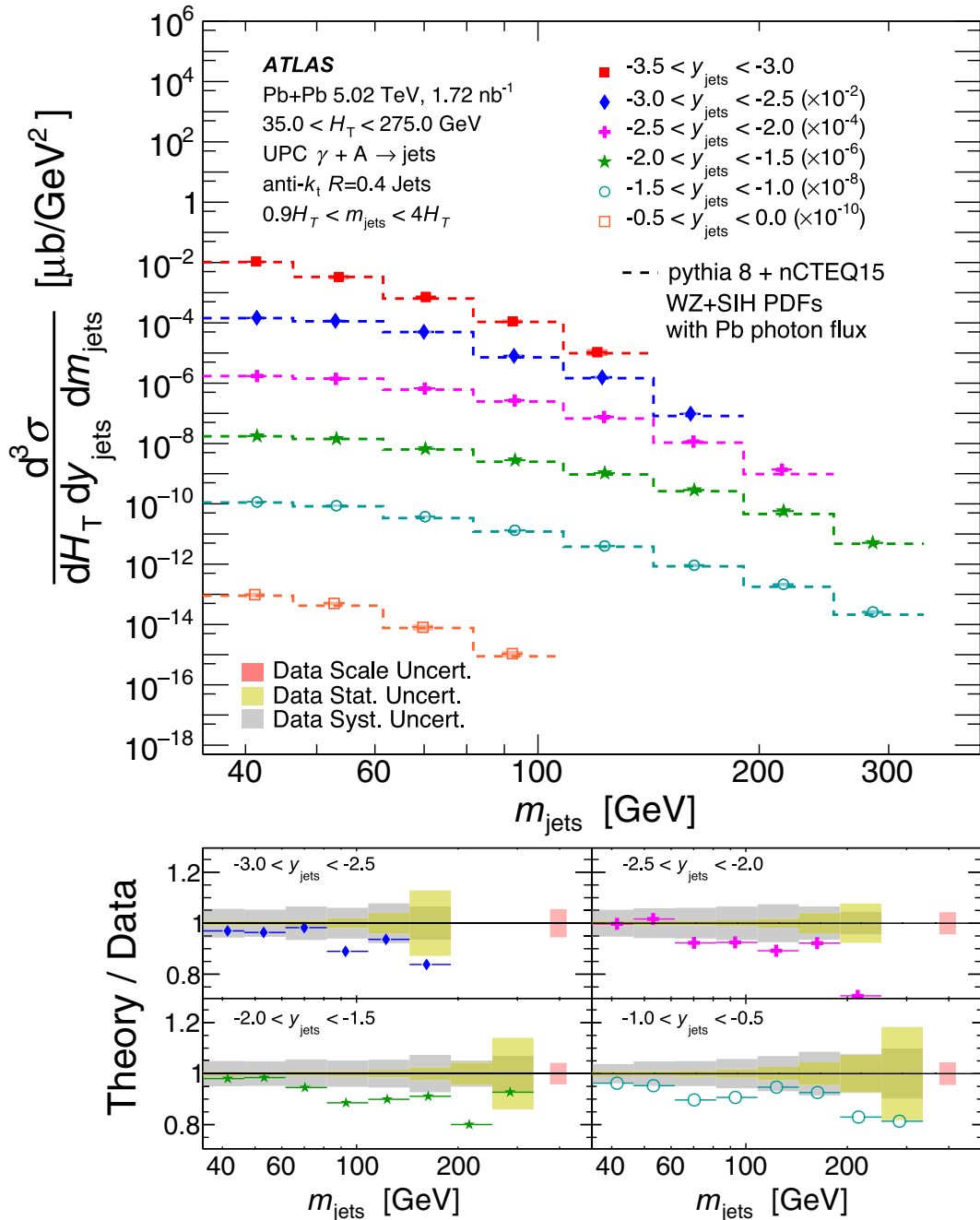


FIG. 18. Triple-differential cross sections, $\frac{d^3\sigma}{dH_T dy_{\text{jets}} dm_{\text{jets}}}$, as a function of m_{jets} , in several y_{jets} intervals. The cross sections are integrated over the H_T acceptance. Systematic uncertainties are shown in the upper panel as shaded boxes, while statistical uncertainties shown as vertical lines are usually smaller than the size of the markers. A theoretical comparison is shown to cross sections computed using PYTHIA8 with nCTEQ15 WZ + SIH PDFs, a photon flux from STARLIGHT, and a z_γ -dependent data-driven breakup fraction. The bottom panels show the ratio between the theory prediction and the data for a selection of the y_{jets} intervals. The light red bands in the ratio panels are the quadrature sum of scale uncertainties on the cross section, while the gray band shows the residual systematic uncertainty. The yellow band shows the point-to-point statistical uncertainty.

high z_γ , the theoretical calculation in the nuclear shadowing region underpredicts the data. These features are most prominent at low H_T , while the theory typically underpredicts the data for the higher H_T intervals without

substantial dependence on x_A . Only in the highest x_A interval, 0.288–0.5, is any substantial modification from the EMC effect expected, and it is typically in good agreement with the data.

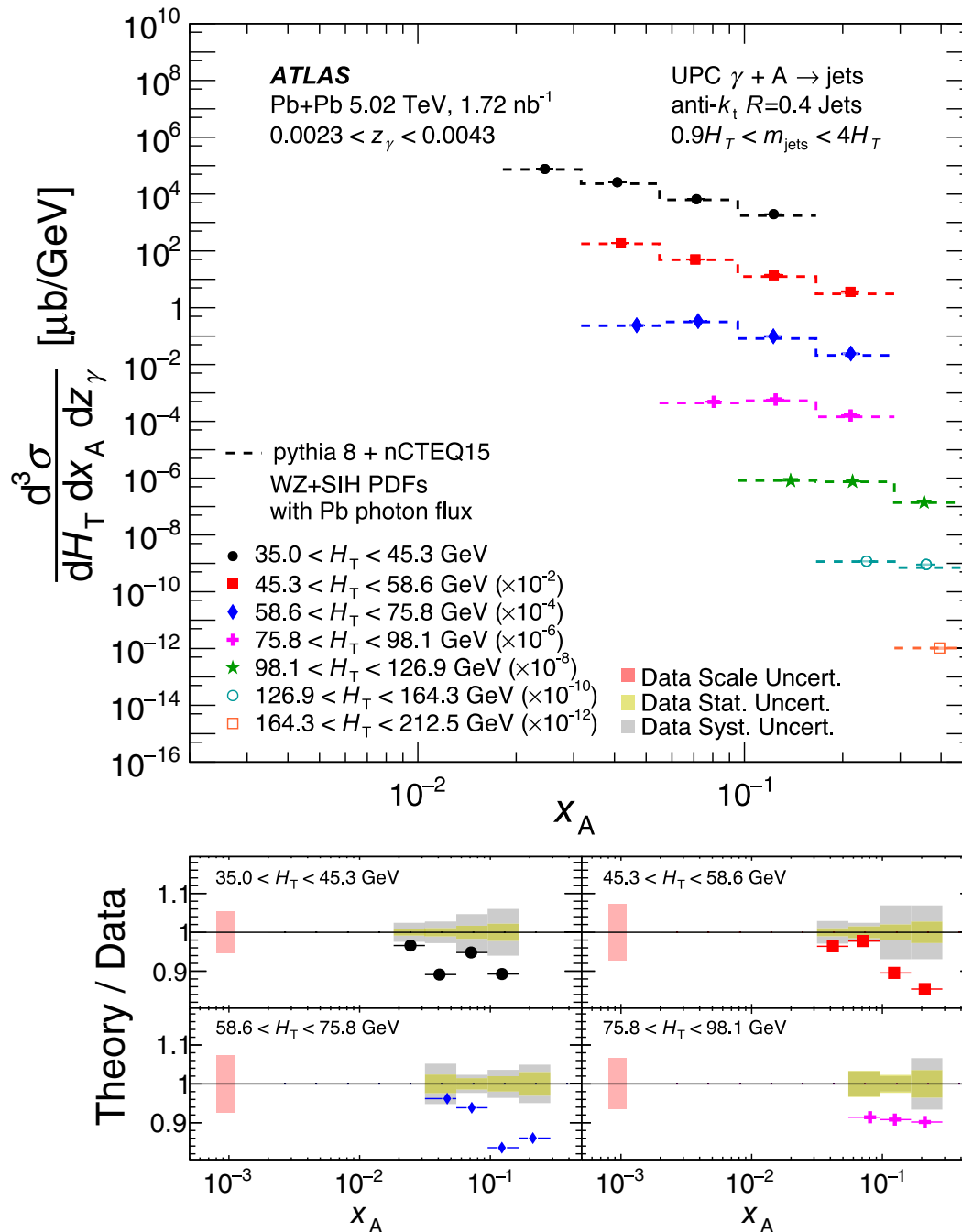


FIG. 19. Triple-differential cross sections, $\frac{d^3\sigma}{dH_T dx_A dz_\gamma}$, as a function of x_A for different bins of H_T for events with emitted photon energies in the kinematic range $0.0023 < z_\gamma < 0.0043$. In the upper panel, systematic uncertainties are shown as shaded boxes, while statistical uncertainties shown as vertical lines are usually smaller than the size of the markers. A theoretical comparison is shown to cross sections computed using PYTHIA8 with nCTEQ15 WZ + SIH PDFs, a photon flux from STARLIGHT, and a z_γ -dependent breakup fraction. The bottom panels show the ratio between the theory prediction and data for a representative subset of the bins of H_T . The Lorentz-invariant variables x_A , z_γ , and H_T are unambiguously defined in terms of the particle-level jet kinematics and correspond at leading order to the Bjorken- x , emitted photon energy fraction, and collision Q^2 , respectively. The light red bands in the ratio panels are the quadrature sum of scale uncertainties on the cross section, while the gray band shows the remaining systematic uncertainty. The yellow band shows the point-to-point statistical uncertainty.

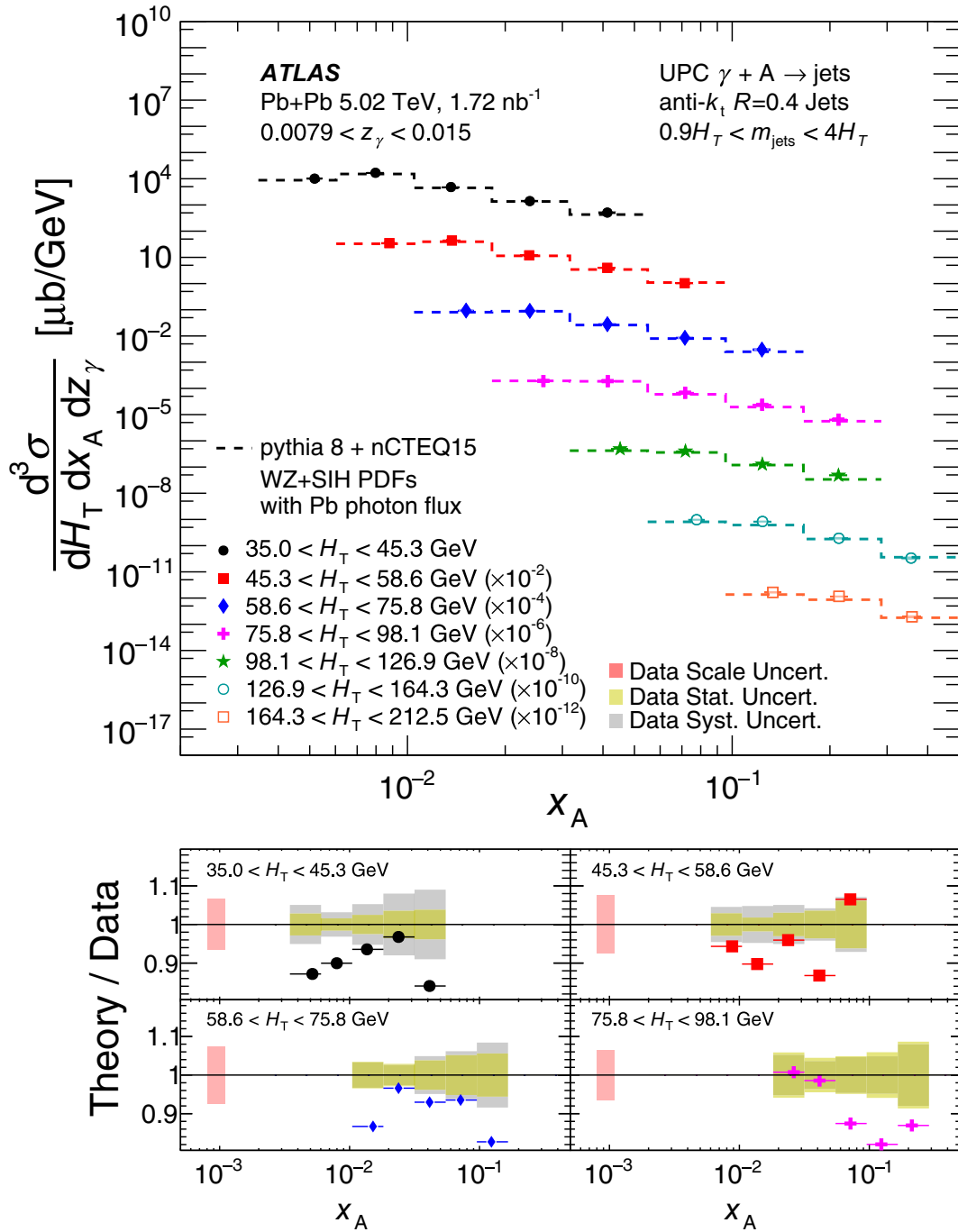


FIG. 20. Triple-differential cross sections, $\frac{d^3\sigma}{dH_T dx_A dz_\gamma}$, as a function of x_A for different bins of H_T for events with emitted photon energies in the kinematic range $0.0079 < z_\gamma < 0.015$. In the upper panel, systematic uncertainties are shown as shaded boxes, while statistical uncertainties shown as vertical lines are usually smaller than the size of the markers. A theoretical comparison is shown to cross sections computed using PYTHIA8 with nCTEQ15 WZ + SIH PDFs, a photon flux from STARLIGHT, and a z_γ -dependent breakup fraction. The bottom panels show the ratio between the theory prediction and data for a representative subset of the bins of H_T . The Lorentz-invariant variables x_A , z_γ , and H_T are unambiguously defined in terms of the particle-level jet kinematics and correspond at leading order to the Bjorken- x , emitted photon energy fraction, and collision Q^2 , respectively. The light red bands in the ratio panels are the quadrature sum of scale uncertainties on the cross section, while the gray band shows the remaining systematic uncertainty. The yellow band shows the point-to-point statistical uncertainty.

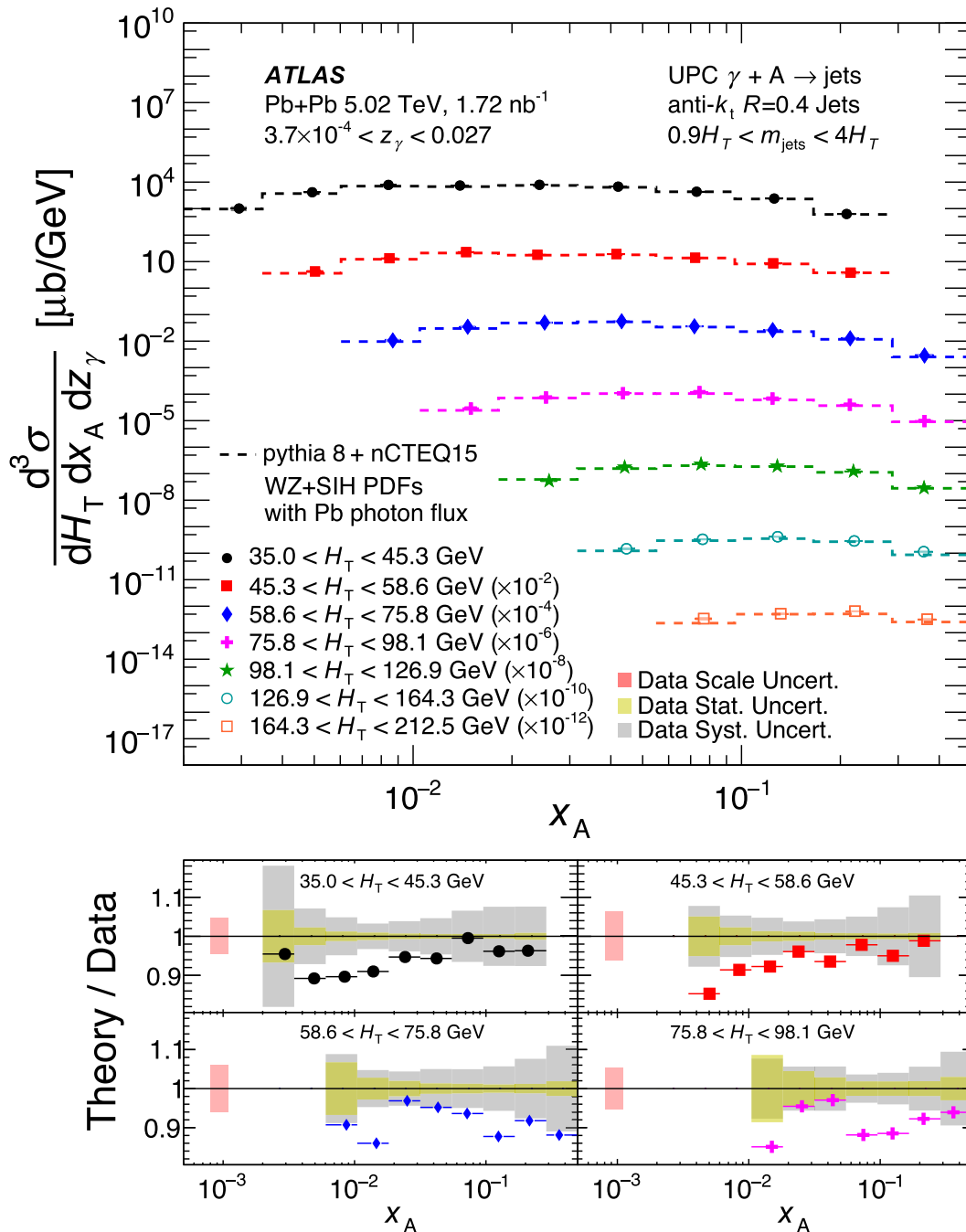


FIG. 21. Triple-differential cross sections, $\frac{d^3\sigma}{dH_T dx_A dz_\gamma}$, as a function of x_A for different bins of H_T for events with emitted photon energies in the kinematic range $3.7 \times 10^{-4} < z_\gamma < 0.027$. In the upper panel, systematic uncertainties are shown as shaded boxes, while statistical uncertainties shown as vertical lines are usually smaller than the size of the markers. A theoretical comparison is shown to cross sections computed using PYTHIA8 with nCTEQ15 WZ + SIH PDFs, a photon flux from STARLIGHT, and a z_γ -dependent breakup fraction. The bottom panels show the ratio between the theory prediction and data for a representative subset of the bins of H_T . The Lorentz-invariant variables x_A , z_γ , and H_T are unambiguously defined in terms of the particle-level jet kinematics and correspond at leading order to the Bjorken- x , emitted photon energy fraction, and collision Q^2 , respectively. The light red bands in the ratio panels are the quadrature sum of scale uncertainties on the cross section, while the gray band shows the remaining systematic uncertainty. The yellow band shows the point-to-point statistical uncertainty.

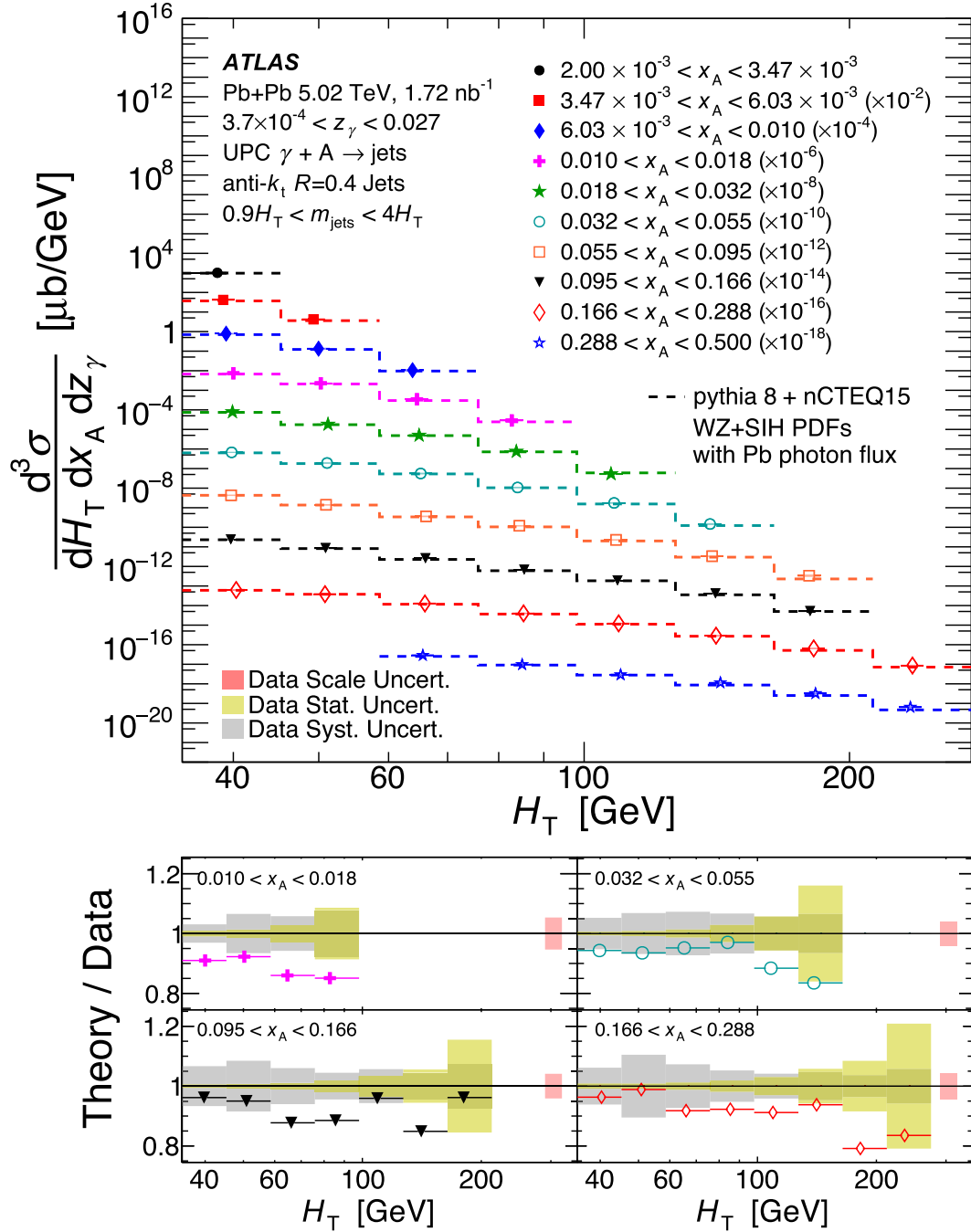


FIG. 22. Triple-differential cross sections, $\frac{d^3\sigma}{dH_T dx_A dz_\gamma}$, as a function of H_T for different bins of x_A for events with emitted photon energies in the kinematic range $3.7 \times 10^{-4} < z_\gamma < 0.027$. In the upper panel, systematic uncertainties are shown as shaded boxes, while statistical uncertainties shown as vertical lines are usually smaller than the size of the markers. A theoretical comparison is shown to cross sections computed using PYTHIA8 with nCTEQ15 WZ + SIH PDFs, a photon flux from STARLIGHT, and a z_γ -dependent breakup fraction. The bottom panels show the ratio between the theory prediction and data for a representative subset of the bins of x_A . The Lorentz-invariant variables x_A , z_γ , and H_T are unambiguously defined in terms of the particle-level jet kinematics and correspond at leading order to the Bjorken- x , emitted photon energy fraction, and collision Q^2 , respectively. The light red bands in the ratio panels are the quadrature sum of scale uncertainties on the cross section, while the gray band shows the remaining systematic uncertainty. The yellow band shows the point-to-point statistical uncertainty.

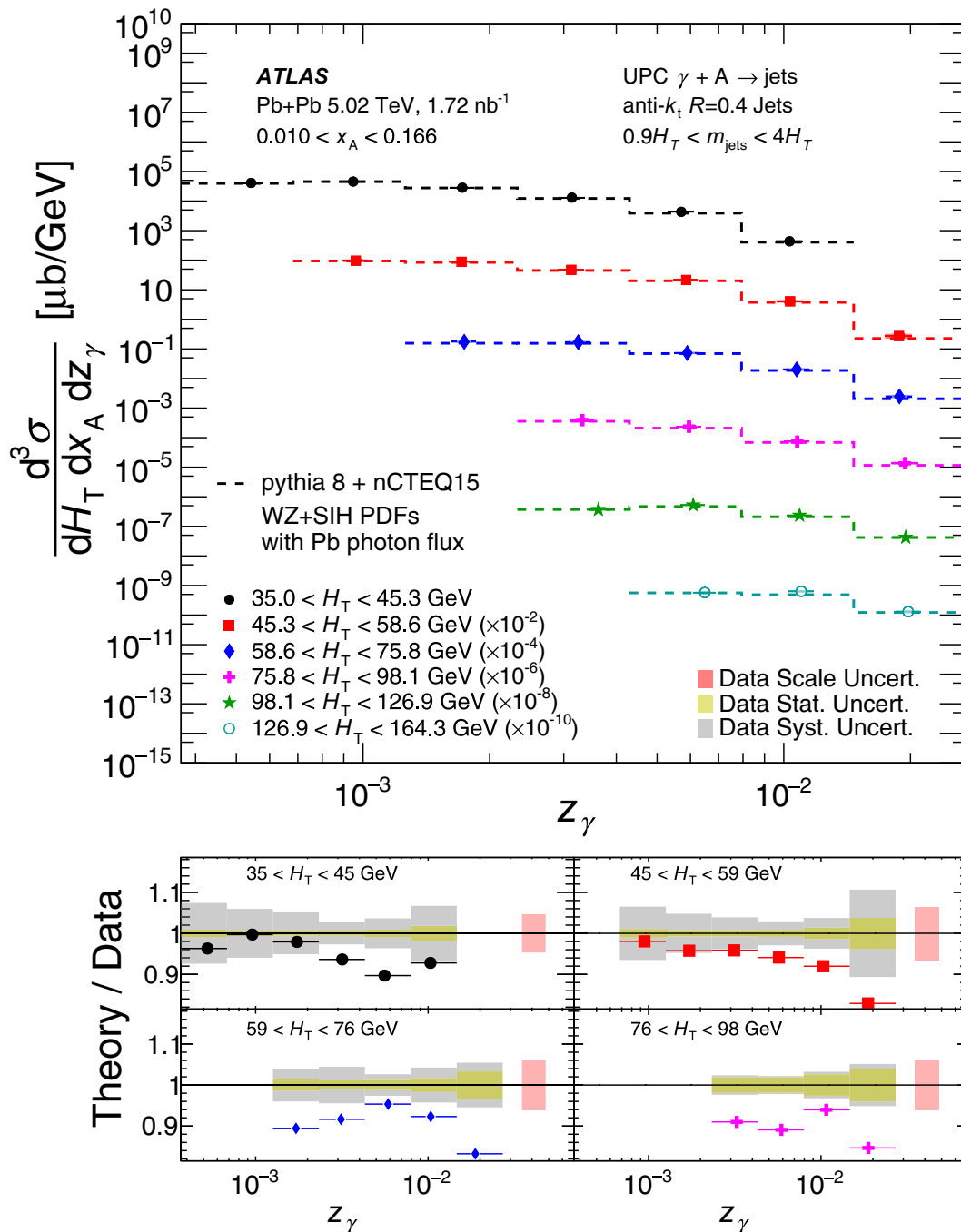


FIG. 23. Triple-differential cross sections, $\frac{d^3\sigma}{dH_T dx_A dz_\gamma}$, as a function of z_γ for different bins of H_T for events with struck parton energies in the kinematic range $0.010 < x_A < 0.166$. In the upper panel, systematic uncertainties are shown as shaded boxes, while statistical uncertainties shown as vertical lines are usually smaller than the size of the markers. A theoretical comparison is shown to cross sections computed using PYTHIA8 with nCTEQ15 WZ + SIH PDFs, a photon flux from STARLIGHT, and a z_γ -dependent breakup fraction. The bottom panels show the ratio between the theory prediction and data for a representative subset of intervals in H_T . The Lorentz-invariant variables x_A , z_γ , and H_T are unambiguously defined in terms of the particle-level jet kinematics and correspond at leading order to the Bjorken- x , emitted photon energy fraction, and collision Q^2 , respectively. The light red bands in the ratio panels are the quadrature sum of scale uncertainties on the cross section, while the gray band shows the remaining systematic uncertainty. The yellow band shows the point-to-point statistical uncertainty.

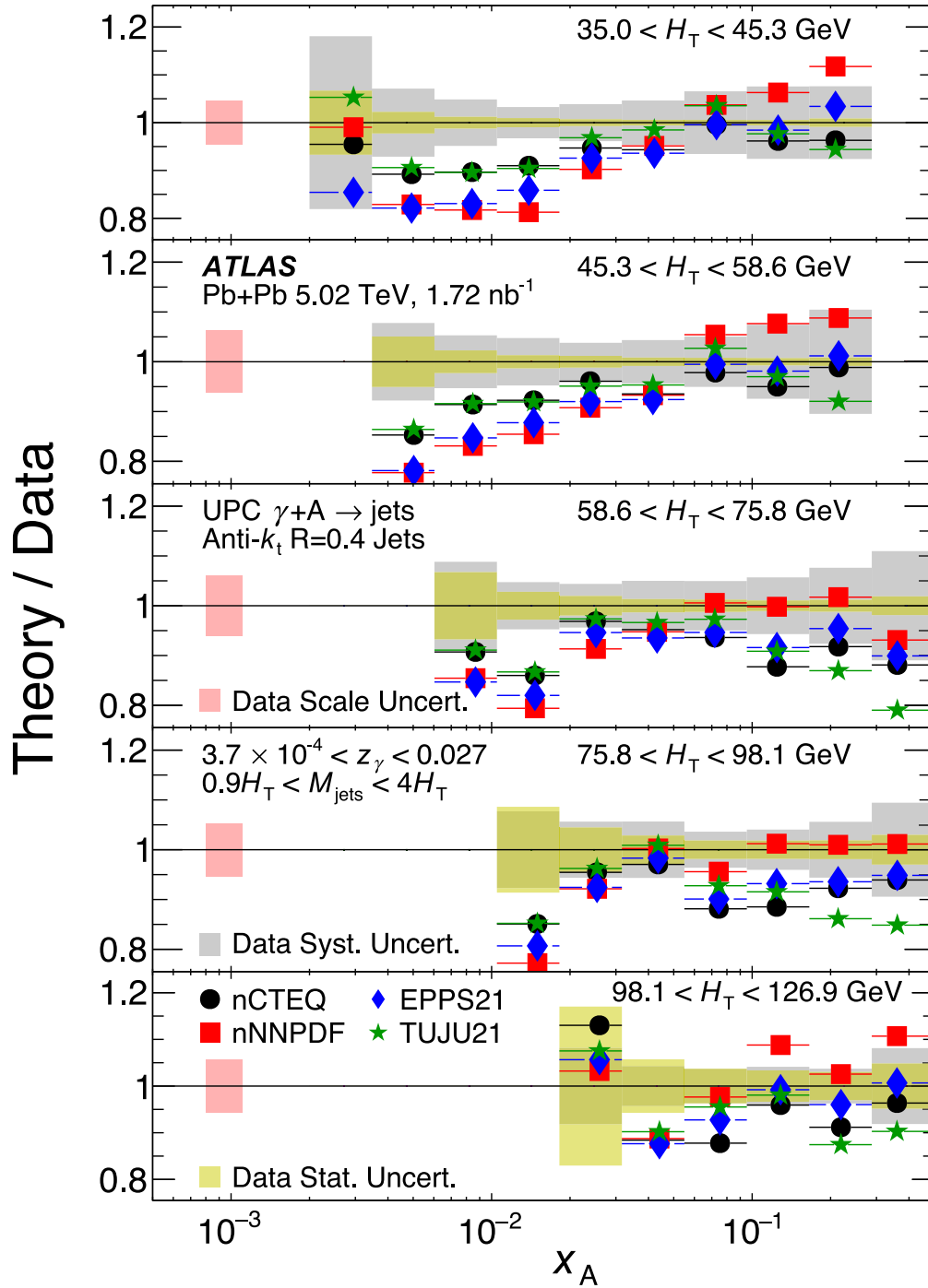


FIG. 24. Ratios of the triple-differential cross sections, $\frac{d^3\sigma}{dH_T dx_A dz_\gamma}$, to theoretical predictions using several nPDF models as a function of x_A for different bins of H_T for events with struck parton energies in the kinematic range $3.7 \times 10^{-4} < z_\gamma < 0.027$. The Lorentz-invariant variables x_A , z_γ , and H_T are unambiguously defined in terms of the particle-level jet kinematics and correspond at leading order to the Bjorken- x , emitted photon energy fraction, and collision Q^2 , respectively. Theoretical comparisons for the cross sections are computed using PYTHIA8 with a photon flux from STARLIGHT, and a z_γ -dependent data-driven breakup correction. Four different theoretical comparisons are shown corresponding to the nCTEQ 15 WZ + SIH, nNNPDF 3.0, EPPS21, and TUJU21 nPDF fits. The light red bands are the quadrature sum of scale uncertainties on the ratio, while the gray band shows the residual systematic uncertainty. The yellow band shows the point-to-point statistical uncertainty.

An alternative presentation of the results shown above plotted as a function of H_T instead of x_A is provided in Figs. 32, 33, 34, and 35 in Appendix C. Figure 22 shows the analogous results integrated over the full range in z_γ . The cross sections in the restricted intervals of z_γ and x_A vary slowly with H_T except at the upper limit of the H_T range.

Figure 23 shows the measured differential cross section as a function of z_γ in different intervals of H_T for a fixed x_A range, $0.010 < x_A < 0.166$. The z_γ dependence over a wide x_A interval should be determined, primarily, by the photon flux and the precision of the cross section calculation for the hard-scattering process. Thus, this comparison should primarily indicate the regions of phase space which are most impacted by the LO precision of PYTHIA8 or uncertainty on the photon flux. The results indicate that differences from PYTHIA8 arise without an obvious dependence on z_γ , and the discrepancies are slightly more significant at higher H_T .

Figure 24 shows the ratio between measured cross-sections and predictions using PYTHIA8 LO calculations with a simulated parton shower and a variety of leading global nPDF fits. These fits include nCTEQ15 WZ + SIH, nNNPDF 3.0, EPPS21 [13], and TUJU21 [12]. The former three fits include different global datasets and employ different methodologies, while the TUJU21 fit is unique for restricting its inputs to only measurements with NNLO theory calculations available. These comparisons demonstrate that no single fit describes the data best in all kinematic regions. At lower H_T , all models underpredict the shadowing region, while nNNPDF slightly overpredicts the antishadowing region. For intermediate H_T intervals, similar discrepancies persist at low x_A , while nNNPDF predicts the cross section in the antishadowing region better than other models. It shows signs of overprediction at high H_T , though, as observed for higher Q^2 in recent measurements of $t\bar{t}$ production in Pb + Pb collisions [75]. These observations may be modified when NLO corrections become available, or when theoretical uncertainties on the modeling of the photon flux are included.

IX. CONCLUSION

This paper presents measurements of photonuclear jet production in ultraperipheral Pb + Pb collisions at $\sqrt{s_{NN}} = 5.02$ TeV from a dataset collected with the ATLAS detector at the LHC corresponding to an integrated luminosity of 1.72 nb^{-1} . The measurement provides unique constraints on nuclear parton distributions in a region of x and Q^2 where currently available data provide very little information.

In the analysis, candidate $\gamma + A$ events are selected using a combination of requirements on the neutron yields in the zero-degree calorimeters and substantial rapidity gaps in the photon-going direction. The selection also has good

acceptance for resolved-photon events that can populate forward rapidities with particles. Triple-differential cross sections are measured using two sets of kinematic variables, $(y_{\text{jets}}, m_{\text{jets}}, H_T)$ and (x_A, z_γ, H_T) , the latter of which more directly reflect the kinematics of the partons in the hard-scattering process, allowing for a clear understanding of the kinematic ranges probed by this measurement. The measured cross sections are corrected for trigger and event selection efficiencies and are unfolded to the particle level using an evaluation of the detector response obtained from a PYTHIA8 $8\gamma + A \rightarrow \text{jets}$ MC sample. These PYTHIA8 events were generated using nCTEQ15 nuclear PDFs and a coherent nuclear photon flux. The resulting sample of events was reweighted to account for modifications to the photon flux resulting from the ultraperipheral (i.e. non-hadronic) event selection and the real impact parameter distribution of $\gamma + A$ processes.

The measured cross sections are compared to LO PYTHIA8 predictions, which are corrected by the probability that the photon-emitting nucleus does not break up due to additional soft photons exchanges that can excite, for example, the giant dipole resonance in the nucleus. This no-breakup probability for $\gamma + A$ processes was measured in data using a sample of events with forward neutron emission in both directions. The comparisons between data and PYTHIA8 show systematic deviations as a function of both z_γ and x_A that may indicate limitations in the theoretical description of the photon flux but also, at fixed z_γ , deviations in the lead PDF relative to the nCTEQ15 WZ + SIH nPDF set used to produce the PYTHIA8 sample. LO PYTHIA8 predictions using all included fits underpredict the data in the shadowing region, while most fits exhibit better agreement with the data in the antishadowing and EMC regions. Extraction of information about nPDFs from this data, however, will rely on more precise NLO pQCD calculations directly comparable to these results. Such theoretical results should offer a direct path for including the data presented here in global nuclear PDF fits, although the inclusion of parton shower corrections is also important for a robust extraction of nPDF effects.

ACKNOWLEDGMENTS

We thank CERN for the very successful operation of the LHC and its injectors, as well as the support staff at CERN and at our institutions worldwide without whom ATLAS could not be operated efficiently. The crucial computing support from all WLCG partners is acknowledged gratefully, in particular from CERN, the ATLAS Tier-1 facilities at TRIUMF/SFU (Canada), NDGF (Denmark, Norway, Sweden), CC-IN2P3 (France), KIT/GridKA (Germany), INFN-CNAF (Italy), NL-T1 (Netherlands), PIC (Spain), RAL (UK) and BNL (USA), the Tier-2 facilities worldwide and large non-WLCG resource providers. Major contributors of computing resources are listed in Ref. [76]. We gratefully acknowledge the support of ANPCyT,

Argentina; YerPhI, Armenia; ARC, Australia; BMWFW and FWF, Austria; ANAS, Azerbaijan; CNPq and FAPESP, Brazil; NSERC, NRC and CFI, Canada; CERN; ANID, Chile; CAS, MOST and NSFC, China; Minciencias, Colombia; MEYS CR, Czech Republic; DNRF and DNSRC, Denmark; IN2P3-CNRS and CEA-DRF/IRFU, France; SRNSFG, Georgia; BMBF, HGF and MPG, Germany; GSRI, Greece; RGC and Hong Kong SAR, China; ISF and Benoziyo Center, Israel; INFN, Italy; MEXT and JSPS, Japan; CNRST, Morocco; NWO, Netherlands; RCN, Norway; MNiSW, Poland; FCT, Portugal; MNE/IFA, Romania; MSTDI, Serbia; MSSR, Slovakia; ARIS and MVZI, Slovenia; DSI/NRF, South Africa; MICIU/AEI, Spain; SRC and Wallenberg Foundation, Sweden; SERI, SNSF and Cantons of Bern and Geneva, Switzerland; NSTC, Taipei; TENMAK, Türkiye; STFC/UKRI, United Kingdom; DOE and NSF, United States of America. Individual groups and members have received support from BCKDF, CANARIE, CRC and DRAC, Canada; CERN-CZ, FORTE and PRIMUS, Czech Republic; COST, ERC, ERDF, Horizon 2020, ICSC-NextGenerationEU and Marie Skłodowska-Curie Actions, European Union; Investissements d’Avenir Labex, Investissements d’Avenir IDEX and ANR, France; DFG and AvH Foundation, Germany; Herakleitos, Thales and Aristeia programmes co-financed by EU-ESF and the Greek NSRF, Greece; BSF-NSF and MINERVA, Israel; NCN and NAWA, Poland; La Caixa Banking Foundation, CERCA Programme Generalitat de Catalunya and PROMETEO and GenT Programmes Generalitat Valenciana, Spain; Göran Gustafssons Stiftelse, Sweden; The Royal Society and Leverhulme Trust, United Kingdom. In addition, individual members wish to acknowledge support from Armenia: Yerevan Physics Institute (FAPERJ); CERN: European Organization for Nuclear Research (CERN PJAS); Chile: Agencia Nacional de Investigación y Desarrollo (Grants No. FONDECYT 1230812, No. FONDECYT 1230987, No. FONDECYT 1240864); China: Chinese Ministry of Science and Technology (Grants No. MOST-2023YFA1605700, No. MOST-2023YFA1609300), National Natural Science Foundation of China (Grants No. NSFC-12175119, No. NSFC-12275265, No. NSFC-12075060); Czech Republic: Czech Science Foundation (Grant No. GACR—24-11373S), Ministry of Education Youth and Sports (Grant No. FORTE CZ.02.01.01/00/22_008/0004632), PRIMUS Research Programme (Grant No. PRIMUS/21/SCI/017); EU: H2020 European Research Council (Grant No. ERC-101002463); European Union: European Research Council (Grants No. ERC-948254, No. ERC-101089007), Horizon 2020 Framework Programme (Grant No. MUCCA—CHIST-ERA-19-XAI-00), European Union, Future Artificial Intelligence Research (FAIR-NextGenerationEU Grant No. PE00000013), Italian Center for High Performance Computing, Big Data and Quantum Computing (ICSC,

NextGenerationEU); France: Agence Nationale de la Recherche (Grants No. ANR-20-CE31-0013, No. ANR-21-CE31-0013, No. ANR-21-CE31-0022, No. ANR-22-EDIR-0002), Investissements d’Avenir Labex (Grant No. ANR-11-LABX-0012); Germany: Baden-Württemberg Stiftung (BW Stiftung-Postdoc Eliteprogramme), Deutsche Forschungsgemeinschaft (Grants No. DFG—469666862, No. DFG—CR 312/5-2); Italy: Istituto Nazionale di Fisica Nucleare (ICSC, NextGenerationEU), Ministero dell’Università e della Ricerca (Grant No. PRIN—20223N7F8K—PNRR M4.C2.1.1); Japan: Japan Society for the Promotion of Science (Grants No. JSPS KAKENHI JP22H01227, No. JSPS KAKENHI JP22H04944, No. JSPS KAKENHI JP22KK0227, No. JSPS KAKENHI JP23KK0245); Netherlands: Netherlands Organisation for Scientific Research (Grant No. NWO Veni 2020—VI.Veni.202.179); Norway: Research Council of Norway (Grant No. RCN-314472); Poland: Ministry of Science and Higher Education (IDUB AGH, POB8, D4 no 9722), Polish National Agency for Academic Exchange (Grant No. PPN/PPO/2020/1/00002/U/00001), Polish National Science Centre (Grants No. NCN-2021/42/E/ST2/00350, No. NCN-OPUS-2022/47/B/ST2/03059, No. NCN-UMO-2019/34/E/ST2/00393, No. NCN & H2020 MSCA 945339, No. UMO-2020/37/B/ST2/01043, No. UMO-2021/40/C/ST2/00187, No. UMO-2022/47/O/ST2/00148, No. UMO-2023/49/B/ST2/04085, No. UMO-2023/51/B/ST2/00920); Slovenia: Slovenian Research Agency (ARIS Grant No. J1-3010); Spain: Generalitat Valenciana (Artemisa, FEDER, IDIFEDER/2018/048), Ministry of Science and Innovation (MCIN & NextGenEU Grants No. PCI2022-135018-2, MICIN & FEDER No. PID2021-125273NB, No. RYC2019-028510-I, No. RYC2020-030254-I, No. RYC2021-031273-I, No. RYC2022-038164-I); Sweden: Carl Trygger Foundation Grant No. CTS-22:2312, Swedish Research Council (Grants No. VR 2023-04654, No. VR 2018-00482, No. VR 2022-03845, No. VR 2022-04683, No. VR 2023-03403, No. VR 2021-03651), Knut and Alice Wallenberg Foundation (Grants No. KAW 2018.0458, No. KAW 2019.0447, No. KAW 2022.0358); Switzerland: Swiss National Science Foundation (Grant No. SNSF—PCEFP2_194658); United Kingdom: Leverhulme Trust (Leverhulme Trust Grant No. RPG-2020-004), Royal Society (Grant No. NIF-R1-231091); United States of America: U.S. Department of Energy (Grant No. ECA DE-AC02-76SF00515), Neubauer Family Foundation.

DATA AVAILABILITY

The data that support the findings of this article are not publicly available. More information on the CERN Open Data Policy can be found in Ref. [77]. The values in the plots and tables associated with this article are stored in HEPData [78].

APPENDIX A: *In situ* MEASUREMENT OF THE JET ENERGY SCALE AND RESOLUTION

1. Samples used for calibration

In situ studies of the jet energy scale and resolution were performed using 334 pb^{-1} of 13 TeV pp data taken by ATLAS in 2017 and 2018. Performing calibration studies in this different collision system is necessary for two reasons: UPCs are not energetic enough to produce the $Z + \text{jet}$ pairs needed to derive the absolute energy scale and alternative MC generators are not available for UPCs in order to test the impact of the MC model on the JES corrections. The pp data were taken in a period where the typical number of interactions per bunch crossing was $\mu = 2$, allowing the data to be taken using the same detector configuration as the UPC data sample. Two sets of triggers were used to collect the data for these studies: a sample requiring at least one high- p_T lepton for studies of $Z + \text{jet}$ balance and a sample requiring at least one high- p_T jet in order to study dijet balance for measures of η -dependence of the JES and to study the JER.

These studies also involved the use of MC samples generated using some combination of PYTHIA8 [25], HERWIG++ [79], POWHEG [80,81], and SHERPA [82]. Samples with the jet cross section calculated at NLO were produced using either SHERPA or a combination of POWHEG with either PYTHIA8 or HERWIG++ to model the parton shower and hadronization. Each sample was produced with the A14 tune [55] and NNPDF 2.3 free proton PDFs [83]. For simulating $Z + \text{jet}$ production, two NLO samples were produced. The first sampled used POWHEG+PYTHIA8, where POWHEG was used to compute the matrix element and PYTHIA8 was used to simulate the parton shower and hadronization. The second sample used SHERPA for both aspects of the event generation. For dijet balance, two samples were used: POWHEG+PYTHIA8 and POWHEG+ HERWIG++.

2. Jet energy scale

The strategy used in this measurement for calibrating the jet energy scale follows previous work from ATLAS [60], and it involves two steps: studies of the absolute energy scale using $Z + \text{jet}$ balance and studies of η -dependent variation of the JES using dijet balance (η intercalibration). This procedure works by first establishing the absolute jet energy scale in a reference rapidity interval ($|\eta| < 0.8$) by studying the balance of jets against a well-measured reference object, the Z boson in this case. Then, the much higher-rate process of dijet production is used to calibrate other η regions relative to this reference region.

a. Absolute energy scale

Studies of the absolute energy scale begin with a sample of events which are required to have at least two

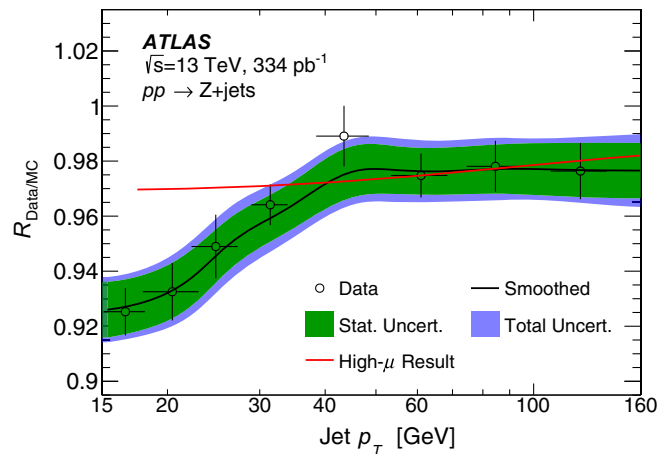


FIG. 25. *In situ* correction to the absolute JES as a function of p_T^{jet} derived from data and MC evaluation of the $Z + \text{jet}$ balance in low- μ ($\mu \sim 2$) pp collisions at 13 TeV. The binned results are smoothed with a Gaussian kernel smoothing procedure, the result of which is shown as a black line. The red line shows the result from high- μ pp collisions.

opposite-charge leptons (either e^+e^- or $\mu^+\mu^-$), where both leptons have $p_T > 20 \text{ GeV}$. Additionally, the dilepton invariant mass is selected to be within the Z peak, and events are required to have at least one jet that balances the Z boson in azimuth with no additional jets in the event. After applying these selections, data distributions of $r = p_T^{\text{jet}}/p_T^Z$ are constructed in bins of p_T^Z . In these studies, a new approach was taken to the fitting procedure, since data taken with low μ is statistically limited. In this approach, the data e^+e^- and $\mu^+\mu^-$ channel distributions are fitted simultaneously by constructing distributions of $r = R_{\text{Data/MC}} p_T^{\text{jet}}/p_T^Z$ using the MC simulation, where $R_{\text{Data/MC}}$ is a rescaling factor used to calibrate the jet p_T in data, in order to account for data-to-MC differences in the absolute JES. This *in situ* correction factor is extracted by iterative χ^2 minimization fitting of these rescaled MC distributions to match the binned data distribution.

This fitting procedure is then performed in bins of p_T^{jet} , with statistical uncertainties derived using the bootstrap method [84], and the binned results are smoothed using a Gaussian kernel smoothing procedure. The results of this calibration procedure, compared to the same calibration factors derived in $\mu = 40$ pp collisions, are shown in Fig. 25. The shaded bands show the statistical and systematic uncertainties, indicating that the primary differences in the *in situ* JES arise at low p_T , likely due to increased sensitivity to low energy topo-clusters most impacted by the different calorimeter conditions. The systematic uncertainties are assigned by comparing the results of two different MC simulation models (POWHEG+PYTHIA8 and SHERPA), varying the event

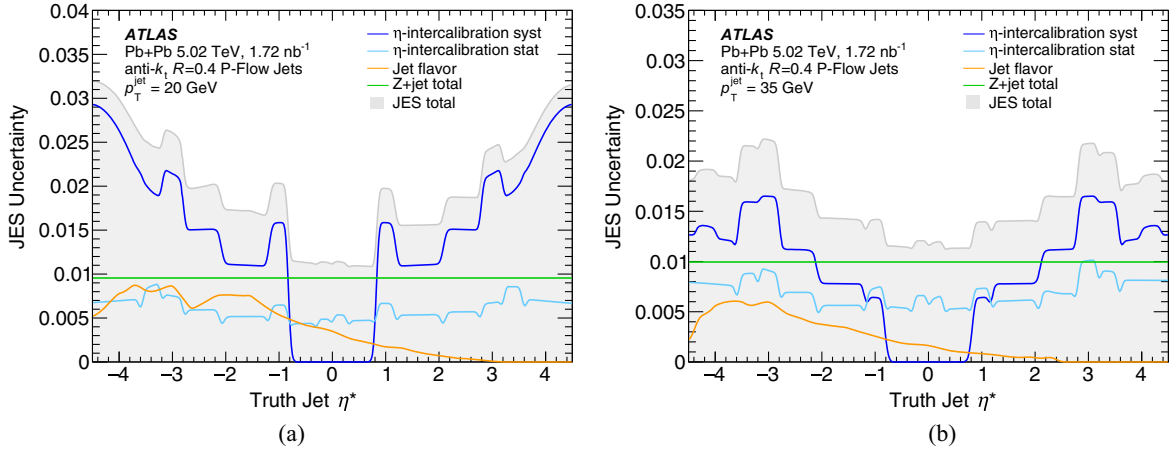


FIG. 26. A summary of all sources of JES systematic uncertainties as a function of η^* for (a) $p_T^{\text{jet}} = 20$ GeV and (b) $p_T^{\text{jet}} = 35$ GeV.

selection criteria, and propagating uncertainty on the electron or muon energy scales. An additional uncertainty is assigned for MC modeling of out-of-cone radiation, which may impact the relative balance between Z bosons and jets in these studies.

b. η intercalibration

The η intercalibration uses a sample of events that are selected by requiring two jets, each with $p_T^{\text{jet}} > 10$ GeV. Further selections are applied in order to ensure the pair should be balanced in p_T , including that the leading dijet pair be azimuthally balanced and that there are no other jets in the event. Then, using this sample, distributions of $(p_{T_1} - p_{T_2})/\langle p_T \rangle$ are constructed in bins of η_1 , η_2 , and $\langle p_T \rangle$, where $\langle p_T \rangle = (p_{T_1} + p_{T_2})/2$. In order to derive η -dependent scale factors from these distributions, the ATLAS matrix method [85] is employed, where a Gaussian fit to each bin in η_1 and η_2 provides a measurement of the product of the relative scale factors in both bins. The results from all bins in η_1 and η_2 are combined via a linear regression procedure to extract a scale factor in each η and $\langle p_T \rangle$ bin.

This same procedure is repeated in data and MC simulation, where the ratio of the scale factors between data and MC measures the relevant data-MC difference in jet response, providing the *in situ* correction factor. These correction factors are then rescaled in each p_T bin so that the correction in the reference region, where the absolute energy scale is determined by $Z + \text{jet}$ balance, is unity. Systematic uncertainties in the η -intercalibration are assessed by varying event selections and the MC generator (POWHEG+PYTHIA8 vs POWHEG+HERWIG++). Statistical uncertainties are determined via the bootstrap method [84]. The resulting calibration factors and systematic uncertainties are smoothed using a two-dimensional

Gaussian kernel smoothing procedure, and an additional uncertainty is assessed for the nonclosure of the procedure, using a combination of studies in $\gamma + A \rightarrow \text{jets}$ events and pp collisions. While the η -intercalibration uncertainties are symmetrized with respect to η , the uncertainties related to the jet flavor composition and response depend on η^* , which is chosen to be positive in the photon-going direction. The total η^* -dependent systematic uncertainties for two particularly relevant values of p_T^{jet} are summarized in Fig. 26.

c. MC-derived UPC correction

In order to translate results on the jet energy calibration in $\mu = 2$ pp to photonuclear jets, an additional correction must be derived from MC simulations to account for differences in the jet energy scale between these two systems. These differences primarily arise from three sources: the different jet flavor compositions of the two samples, the difference in μ between the two systems, and the different underlying event in pp and $\gamma + A$ events. In order to determine a correction accounting for these differences, the calibration derived in $\mu = 2$ pp collisions is applied in photonuclear Pb + Pb event generated with PYTHIA8, and truth jets are matched to their nearest reconstructed jet within $\Delta R < 0.3$. Then, using matched pairs, $p_T^{\text{reco}}/p_T^{\text{true}}$ distributions are constructed in intervals of p_T^{true} and η^{truth} . Then, the mean jet response in each bin is determined by a Gaussian fit to the distribution, and a correction factor is derived from the mean responses via a numerical inversion procedure [86]. The results of this procedure are shown in Fig. 27.

3. Jet energy resolution

In addition to correcting for differences between the JES in data and MC samples, any differences in the jet energy

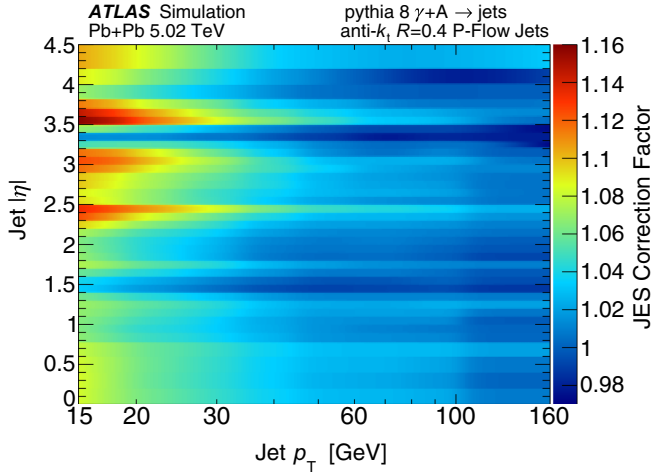


FIG. 27. Correction factors to the jet energy scale, derived in low- μ ($\mu \sim 2$) 13 TeV pp collisions, used to translate the JES to jets in photonuclear Pb + Pb events. The η -dependence of the correction is largely driven by the structure of the ATLAS calorimeter.

resolution [60] may also impact this measurement, thus a direct measurement of any difference and its associated systematic uncertainties is essential for a precise measurement of the cross sections. Unlike the case for the JES, only dijets are necessary to measure the resolution, so these studies are performed directly in UPC jet events. Events are selected with a dijet pair, each with $p_T^{\text{jct}} > 10$ GeV. The jets are required to be nearly back-to-back in azimuth and a veto is applied on events with extra jets, in order to ensure the p_T balance of the pair. The JER is measured in regions of η , and for each region, one jet in the pair (the probe jet) is required to be in that region, while the other jet must be in the designated reference region for the probe jet's η . For jets with $|\eta| < 2.8$, reference regions are the same as the probe regions, but more forward bins use the reference region $1.8 < |\eta| < 2.5$, in order to reduce the statistical uncertainty on the JER measurement. Distributions of $(p_T^{\text{probe}} - p_T^{\text{ref}})/\langle p_T \rangle$ are then constructed for all probe/reference jet pairs.

Binned measurements of the jet energy resolution are then extracted via a convolution fitting procedure [60]. First, the asymmetry distribution of particle-level jets is fitted with a Gaussian times exponential distribution, and then this distribution is convolved with a Gaussian, whose mean and standard deviation are fitted to describe the measured distribution. The width of this convolved Gaussian corresponds to the quadrature sum of the probe and reference resolutions. In η bins where the same region is used as a reference, the extracted resolution therefore must be divided by $\sqrt{2}$. For bins using an external reference, the resolution of the reference bin is subtracted in quadrature. Then, for each η interval, the binned results are fitted as a function of p_T using

$$\sigma(p_T) = \frac{N}{p_T} \oplus \frac{S}{\sqrt{p_T}} \oplus C, \quad (\text{A1})$$

where the N term, corresponding to the contribution from detector noise, is fixed independently via random cone studies. In those studies, the noise contribution is directly measured by sampling $R = 0.4$ random cones of track or cluster energy. Data events are selected with a trigger requiring only energy in exactly one ZDC, which is dominated by empty events, while a sample of minimum-bias $\gamma + A$ collisions simulated with PYTHIA8 are used to perform the studies in the MC simulation. Differences in the results of these p_T -dependent fits of the JER are treated as a systematic uncertainty, and additional uncertainties are assessed by varying the event selections, the MC generator (PYTHIA8 vs SHERPA), and random cone noise term. Additional uncertainties are also assessed for the impact of JES uncertainties on this determination and differences between the estimated JER in the MC simulation via this procedure and the truth-matched JER.

The results for the JER in certain η intervals are shown in the right panel of Fig. 5. Due to the lack of pileup in this sample, the noise contribution from Eq. (A1) is negligible in all bins, so the stochastic and constant terms dominate. For this reason, the η dependence of the JER is the same as at high μ , but it grows much less rapidly with $1/p_T^{\text{jct}}$, allowing for much more precise measurements at low p_T^{jct} . Systematic uncertainties in the *in situ* measurement of the JER are typically a bit larger in this sample than in the high- μ calibration, but the total uncertainty in the measurement is still reduced due to the smaller overall JER values.

APPENDIX B: FIDUCIAL AND GEOMETRIC ACCEPTANCE DEFINITION

The jet and event selections described in Table II limit the kinematic acceptance of this measurement at the particle level in both sets of kinematic variables, $(y_{\text{jets}}, m_{\text{jets}}, H_T)$ and (x_A, z_γ, H_T) . To determine the true acceptance of the measurement, each of the intervals defined in Table I is subdivided into much finer intervals in each of the three dimensions. For each of the resulting finer volumes in $(y_{\text{jets}}, m_{\text{jets}}, H_T)$ or (x_A, z_γ, H_T) , the fraction of MC $\gamma + A$ events falling within the subvolume that satisfy the event selection is determined using particle-level kinematics and selections. The resulting acceptance functions, $A(y_{\text{jets}}, m_{\text{jets}}, H_T)$ and $A(x_A, z_\gamma, H_T)$, are used to determine the geometric acceptance region, which is defined to contain all subdivided volumes that have $A > 0.1$. The segmentation of the volume elements is chosen to be sufficiently fine that varying it has negligible impact on the resulting procedure. Two effects that impact the differential cross section are considered in the following

section: the missing acceptance within the accepted regions and the accepted volume covering only a fraction of the total bin volume.

Using the result of the geometric acceptance determination, the accepted volumes in $\Delta V(y_{\text{jets}}, m_{\text{jets}}, H_{\text{T}})$ and $\Delta V(x_{\text{A}}, z_{\gamma}, H_{\text{T}})$ in the nominal binning (bins i, j, k in each dimension) are calculated according to

$$\begin{aligned} \Delta V(y_{\text{jets}}, m_{\text{jets}}, H_{\text{T}}) &= \sum_i \sum_j \sum_k \Delta H_{\text{T}}^i \Delta y_{\text{jets}}^j \Delta m_{\text{jets}}^k \Theta[A(y_{\text{jets}}, m_{\text{jets}}, H_{\text{T}}) - 0.1], \end{aligned} \quad (\text{B1})$$

$$\begin{aligned} \Delta V(x_{\text{A}}, z_{\gamma}, H_{\text{T}}) &= \sum_i \sum_j \sum_k \Delta H_{\text{T}}^i \Delta x_{\text{A}}^j \Delta z_{\gamma}^k \Theta[A(x_{\text{A}}, z_{\gamma}, H_{\text{T}}) - 0.1], \end{aligned} \quad (\text{B2})$$

where ΔH_{T}^i , Δy_{jets}^j , Δm_{jets}^k , Δx_{A}^j , and Δz_{γ}^k are the widths of sub-bin (i, j, k) for the nominal bin in these variables. This more detailed calculation of the accepted phase-space volume from Eqs. (B1) and (B2) is used to normalize the differential cross section, as described in Sec. VD. The accepted volume fraction, f_{vol} , is defined for either variable set as

$$f_{\text{vol}}(y_{\text{jets}}, m_{\text{jets}}, H_{\text{T}}) \equiv \frac{\Delta V(y_{\text{jets}}, m_{\text{jets}}, H_{\text{T}})}{\Delta H_{\text{T}} \Delta y_{\text{jets}} \Delta m_{\text{jets}}}, \quad (\text{B3})$$

$$f_{\text{vol}}(x_{\text{A}}, z_{\gamma}, H_{\text{T}}) \equiv \frac{\Delta V(x_{\text{A}}, z_{\gamma}, H_{\text{T}})}{\Delta H_{\text{T}} \Delta x_{\text{A}} \Delta z_{\gamma}}. \quad (\text{B4})$$

The volume fractions are then used to impose two requirements on the bins that are reported in this measurement. First, any bin where more than 2.5% of the total cross section in that bin falls outside of the geometric acceptance region is excluded from the reported results. Second, any bin is excluded if $f_{\text{vol}} < 0.5$.

An additional correction is applied, which accounts for the difference between the measured fiducial cross section and the total $\gamma + A \rightarrow \text{jets}$ cross section. This correction accounts for events that fall into a given kinematic bin but fail the single-jet rapidity ($|\eta^{\text{jet}}| < 4.4$) or jet system mass ($0.9 < m_{\text{jets}}/H_{\text{T}} < 4$) requirements. These corrections do not attempt to account for the single-jet p_{T} ($p_{\text{T}}^{\text{jet}} > 15$ GeV) requirement or the requirement of at least two jets in the event. For any bin with $A < 0.975$, the bin is excluded from the results reported in the measurement, while bins with $A > 0.975$ are corrected

for their partial acceptance. This approach limits the impact of potential mismodeling of the fiducial acceptance on this correction.

The results of the acceptance calculation using the subdivided volumes are also used to determine the average values for each of the kinematic variables within the larger volumes defined in Table I. These averages are calculated according to

$$\langle k \rangle = \frac{\sum_i k_i \sigma_i}{\sum_i \sigma_i}, \quad (\text{B5})$$

where k represents one of the kinematic variables, i runs over the subvolumes that pass the $A > 0.1$ criterion, k_i represents the value of k at the middle of the subvolume, and σ_i represents the total cross section in subvolume i in $(y_{\text{jets}}, m_{\text{jets}}, H_{\text{T}})$ or $(x_{\text{A}}, z_{\gamma}, H_{\text{T}})$ space. This calculation assumes that events populate the accepted region in each subvolume uniformly. It also relies on the shape of the PYTHIA8 cross section distribution in order to determine the bin mean values, but no such dependence is built into the actual reported cross sections. Figures 28 and 29 display all the different calculations and selections described in this section, showing f_{vol} for all bins that pass the requirements on fiducial acceptance within the geometric acceptance region. For bins with $f_{\text{vol}} > 0.5$, the bin means are shown, as calculated by Eq. (B5). These figures demonstrate that most bins have $f_{\text{vol}} = 1$, with smaller acceptance fractions occurring near acceptance edges. The $|\eta^{\text{jet}}| < 4.4$ requirement limits the acceptance at high x_{A} and y_{jets} , especially at low H_{T} . The loss of acceptance near the diagonal acceptance edges in $x_{\text{A}}-z_{\gamma}$ space arise due to both the mass requirements and geometric effects from the three-dimensional binning combined with single-jet p_{T} requirements.

APPENDIX C: RESULTS FOR ADDITIONAL z_{γ} INTERVALS

Several additional figures demonstrating the measured cross sections described in Sec. VIII B are shown here. These figures include the x_{A} dependence of the cross section in two additional z_{γ} intervals in Figs. 30 and 31, as well as the H_{T} dependence for four z_{γ} intervals in Figs. 32, 33, 34, and 35. These additional intervals in z_{γ} allow for a more robust separation of the correlated and uncorrelated uncertainty components, helping to demonstrate the size of point-to-point uncertainties most relevant for constraining nPDF effects.

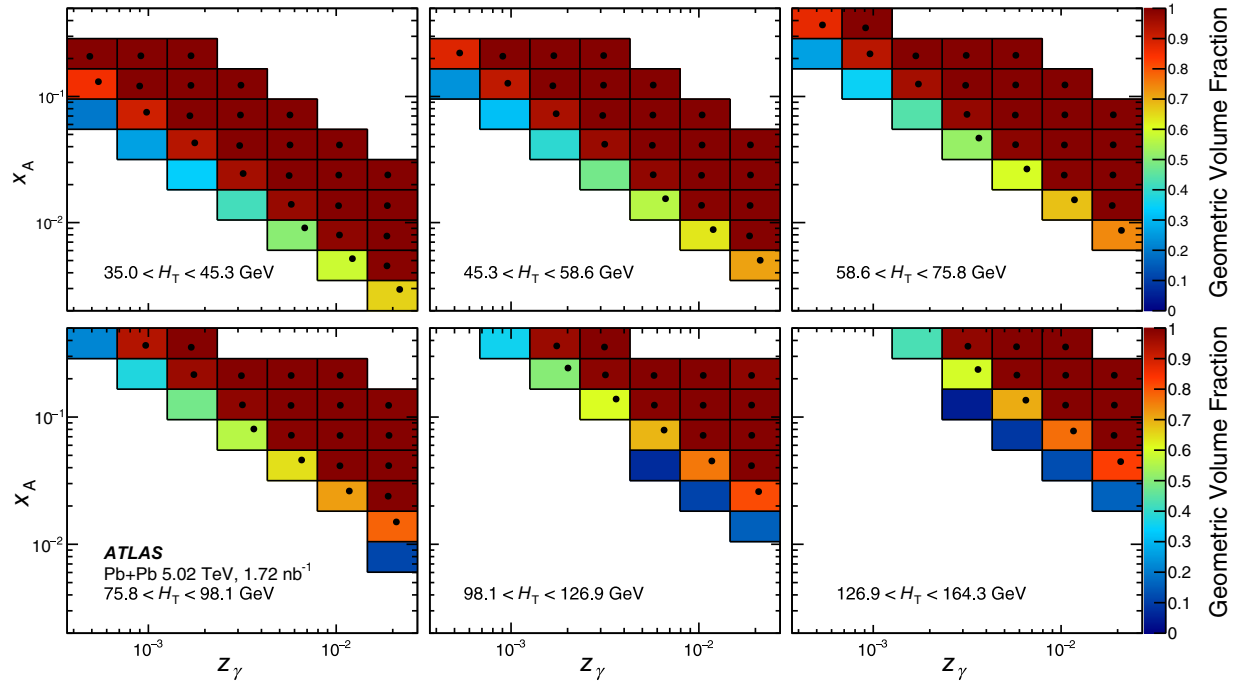


FIG. 28. The fraction of each bin volume that is included in the geometric acceptance region for the hard-scattering kinematic variables. Recomputed bin means for each bin are shown as markers. Only bins that pass a minimum threshold on the fiducial and geometric acceptance are shown, and the means are only shown for bins with $f_{\text{vol}} > 50\%$.

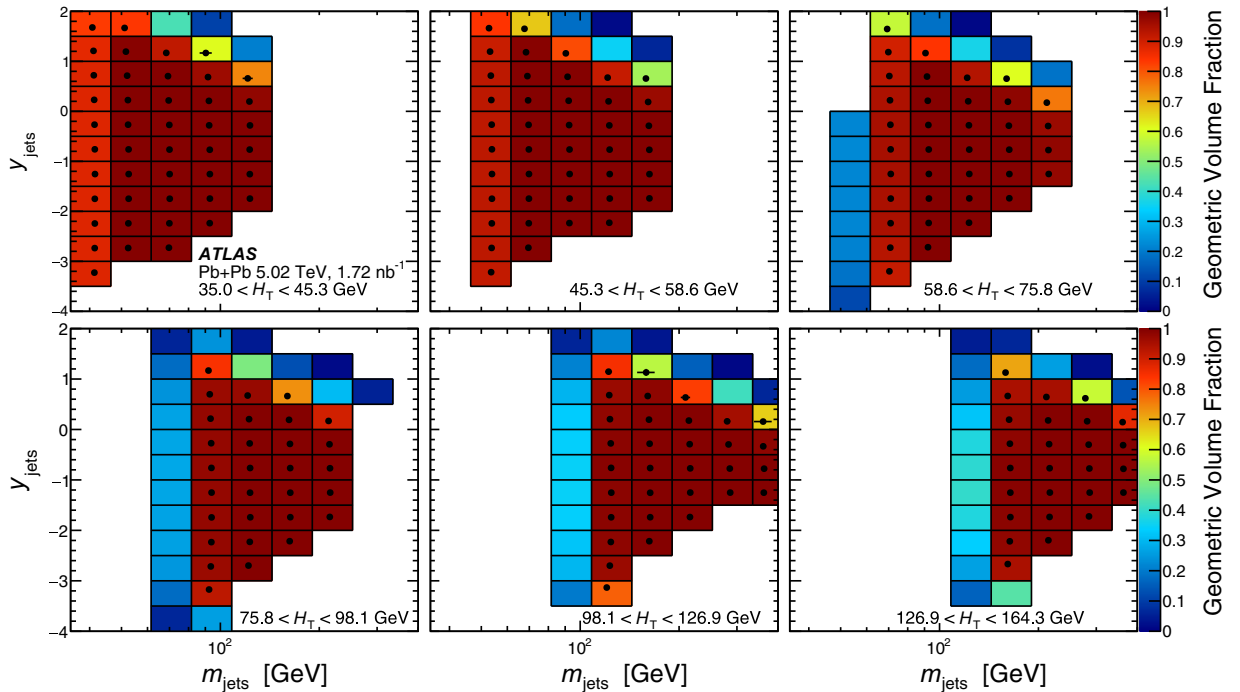


FIG. 29. The fraction of each bin volume that is included in the geometric acceptance region for the jet system kinematic variables. Recomputed bin means for each bin are shown as markers. Only bins that pass a minimum threshold on the fiducial and geometric acceptance are shown, and the means are only shown for bins with $f_{\text{vol}} > 50\%$.

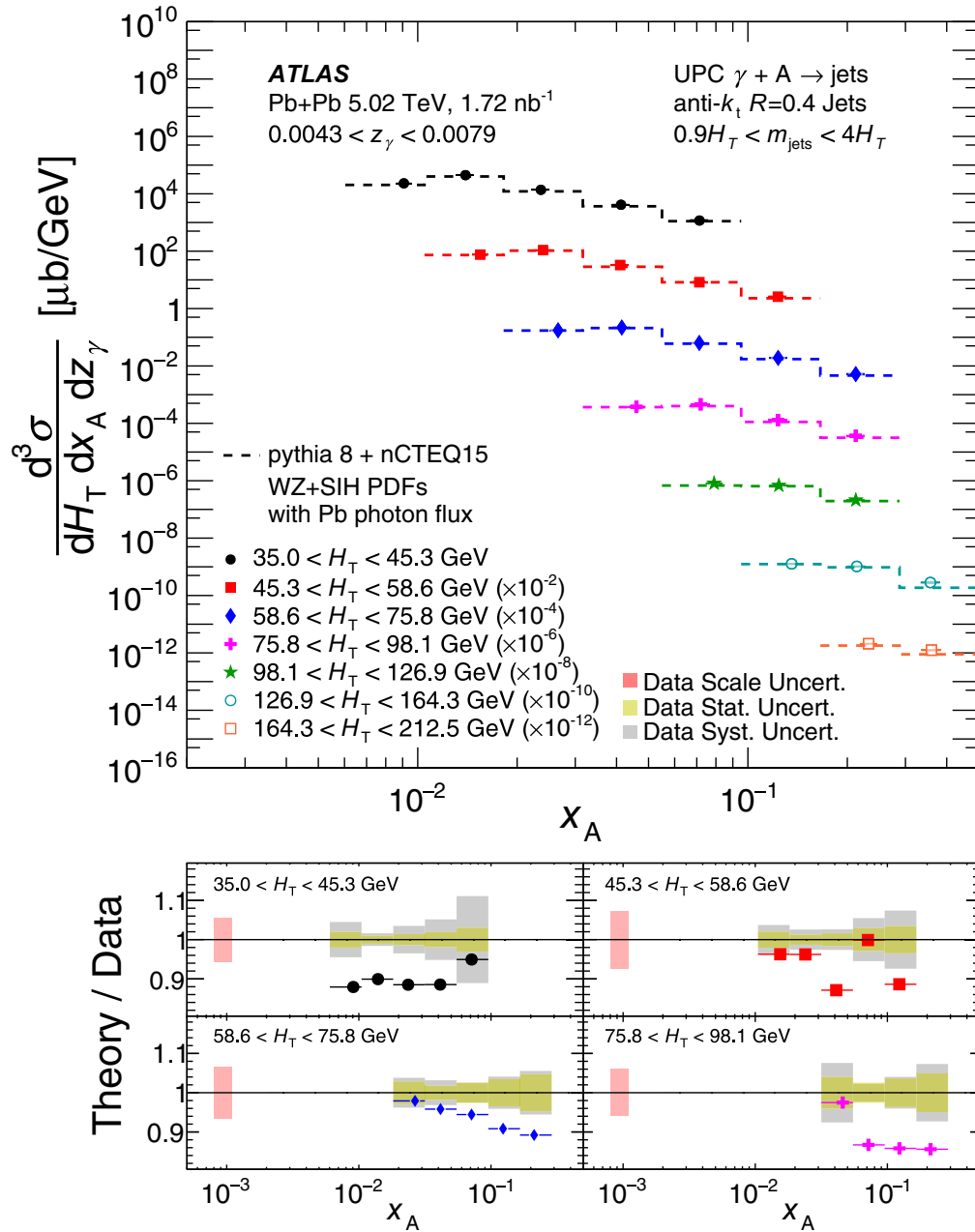


FIG. 30. Triple-differential cross sections, $\frac{d^3\sigma}{dH_T dx_A dz_\gamma}$, as a function of x_A for different bins of H_T for events with emitted photon energies in the kinematic range $0.0043 < z_\gamma < 0.0079$. In the upper panel, systematic uncertainties are shown as shaded boxes, while statistical uncertainties shown as vertical lines are usually smaller than the size of the markers. A theoretical comparison is shown to cross sections computed using PYTHIA8 with nCTEQ15 WZ + SIH PDFs, a photon flux from STARLIGHT, and a z_γ -dependent breakup fraction. The bottom panels show the ratio between the theory prediction and data for a representative subset of the bins of H_T . The Lorentz-invariant variables x_A , z_γ , and H_T are unambiguously defined in terms of the particle-level jet kinematics and correspond at leading order to the Bjorken- x , emitted photon energy fraction, and collision Q^2 , respectively. The light red bands in the ratio panels are the quadrature sum of scale uncertainties on the cross section, while the gray band shows the remaining systematic uncertainty. The yellow band shows the point-to-point statistical uncertainty.

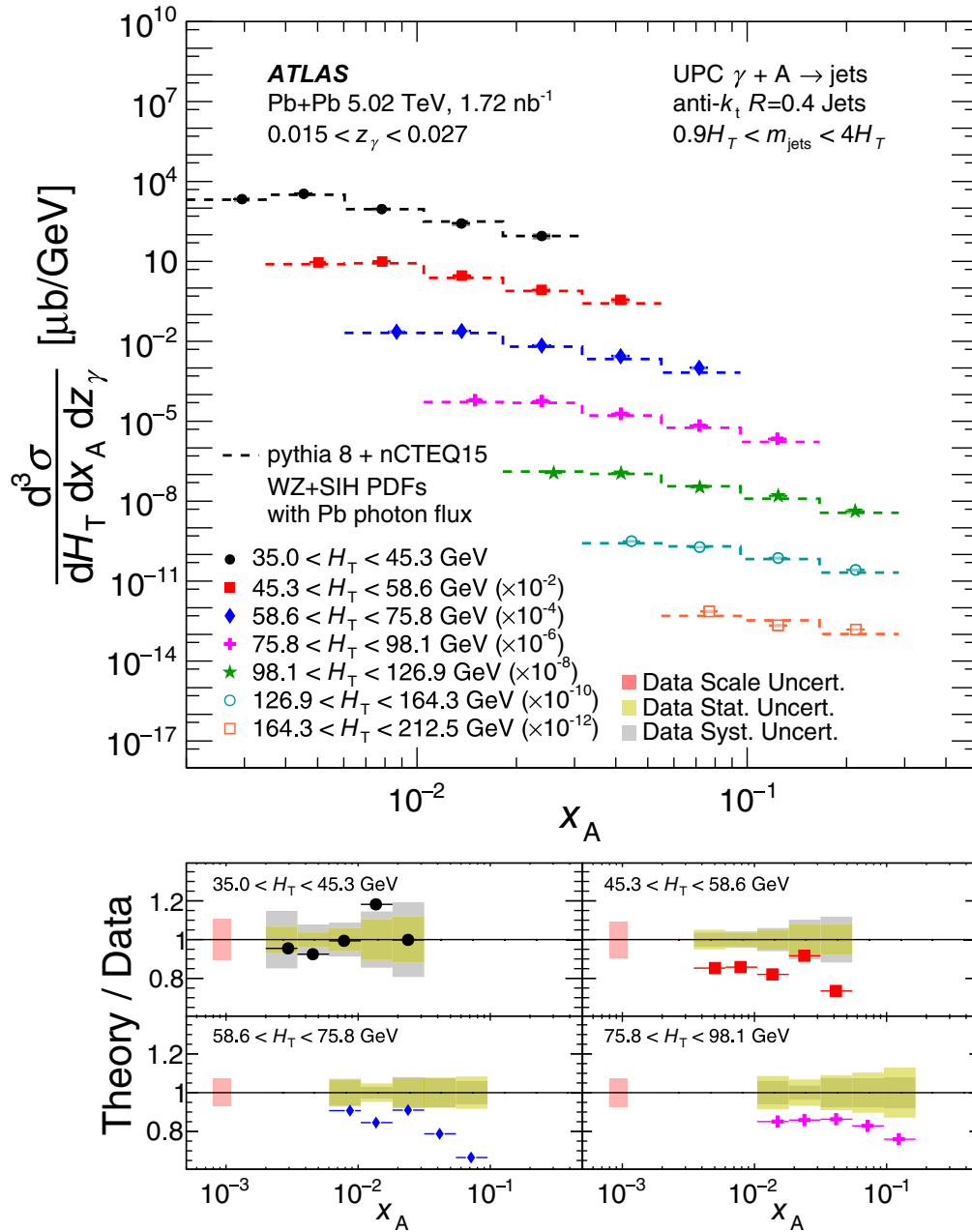


FIG. 31. Triple-differential cross sections, $\frac{d^3\sigma}{dH_T dx_A dz_\gamma}$, as a function of x_A for different bins of H_T for events with emitted photon energies in the kinematic range $0.015 < z_\gamma < 0.027$. In the upper panel, systematic uncertainties are shown as shaded boxes, while statistical uncertainties shown as vertical lines are usually smaller than the size of the markers. A theoretical comparison is shown to cross sections computed using PYTHIA8 with nCTEQ15 WZ + SIH PDFs, a photon flux from STARLIGHT, and a z_γ -dependent breakup fraction. The bottom panels show the ratio between the theory prediction and data for a representative subset of the bins of H_T . The Lorentz-invariant variables x_A , z_γ , and H_T are unambiguously defined in terms of the particle-level jet kinematics and correspond at leading order to the Bjorken- x , emitted photon energy fraction, and collision Q^2 , respectively. The light red bands in the ratio panels are the quadrature sum of scale uncertainties on the cross section, while the gray band shows the remaining systematic uncertainty. The yellow band shows the point-to-point statistical uncertainty.

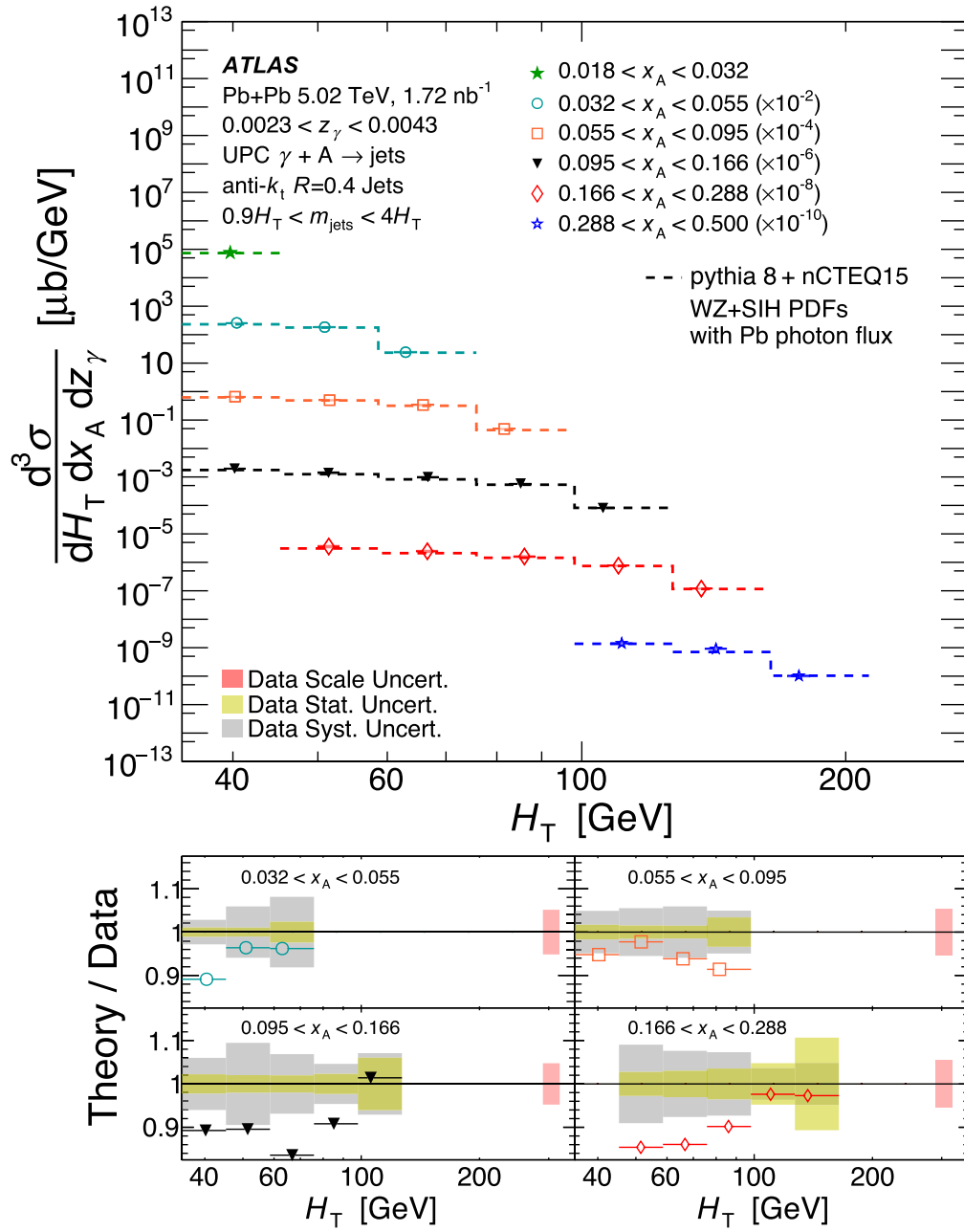


FIG. 32. Triple-differential cross sections, $\frac{d^3\sigma}{dH_T dx_A dz_\gamma}$, as a function of H_T for different bins of x_A for events with emitted photon energies in the kinematic range $0.0023 < z_\gamma < 0.0043$. In the upper panel, systematic uncertainties are shown as shaded boxes, while statistical uncertainties shown as vertical lines are usually smaller than the size of the markers. A theoretical comparison is shown to cross-sections computed using PYTHIA8 with nCTEQ15 WZ + SIH PDFs, a photon flux from STARLIGHT, and a z_γ -dependent breakup fraction. The bottom panels show the ratio between the theory prediction and data for a representative subset of the bins of x_A . The Lorentz-invariant variables x_A , z_γ , and H_T are unambiguously defined in terms of the particle-level jet kinematics and correspond at leading order to the Bjorken- x , emitted photon energy fraction, and collision Q^2 , respectively. The light red bands in the ratio panels are the quadrature sum of scale uncertainties on the cross section, while the gray band shows the remaining systematic uncertainty. The yellow band shows the point-to-point statistical uncertainty.

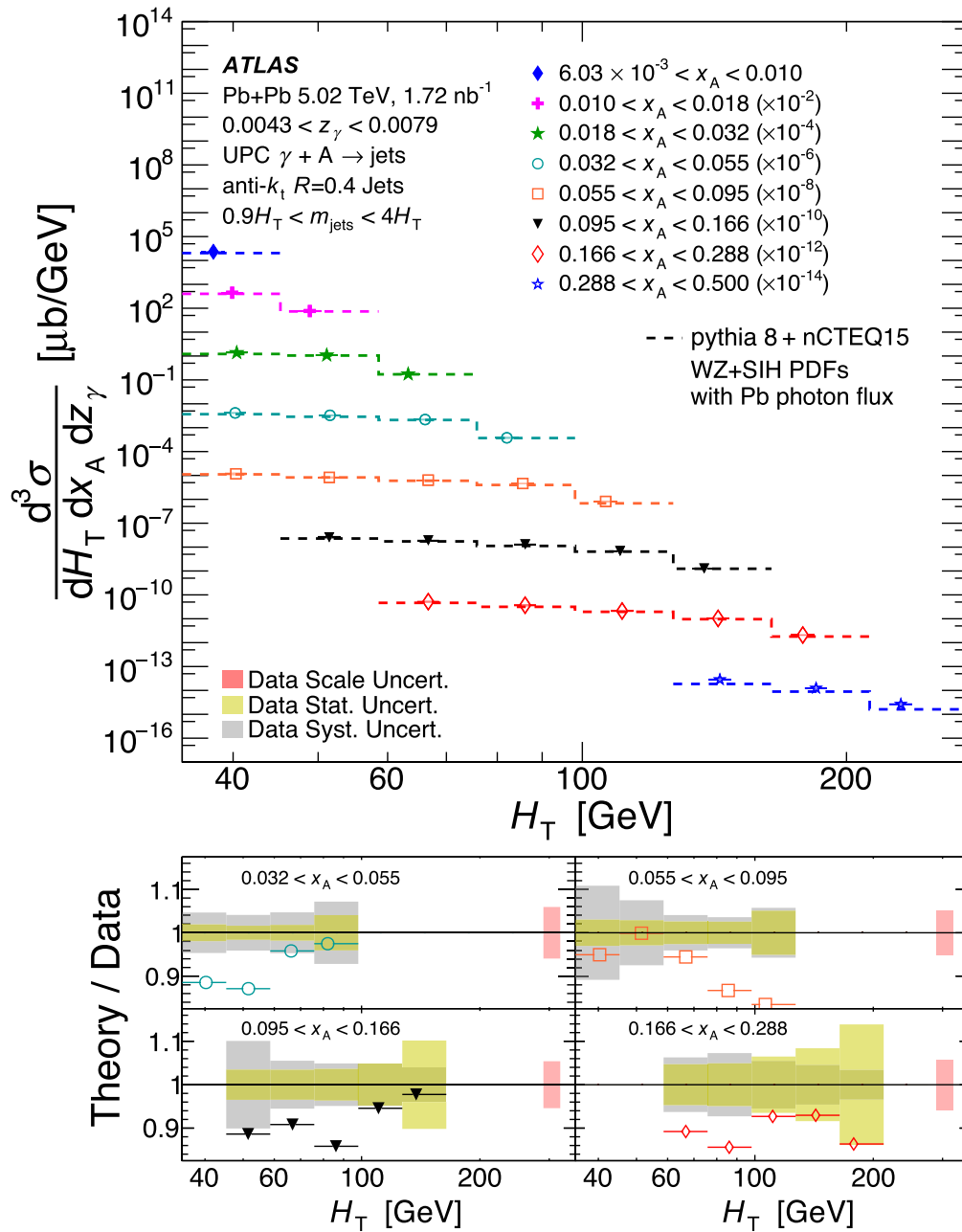


FIG. 33. Triple-differential cross sections, $\frac{d^3\sigma}{dH_T dx_A dz_\gamma}$, as a function of H_T for different bins of x_A for events with emitted photon energies in the kinematic range $0.0043 < z_\gamma < 0.079$. In the upper panel, systematic uncertainties are shown as shaded boxes, while statistical uncertainties shown as vertical lines are usually smaller than the size of the markers. A theoretical comparison is shown to cross sections computed using PYTHIA8 with nCTEQ15 WZ + SIH PDFs, a photon flux from STARLIGHT, and a z_γ -dependent breakup fraction. The bottom panels show the ratio between the theory prediction and data for a representative subset of the bins of x_A . The Lorentz-invariant variables x_A , z_γ , and H_T are unambiguously defined in terms of the particle-level jet kinematics and correspond at leading order to the Bjorken- x , emitted photon energy fraction, and collision Q^2 , respectively. The light red bands in the ratio panels are the quadrature sum of scale uncertainties on the cross section, while the gray band shows the remaining systematic uncertainty. The yellow band shows the point-to-point statistical uncertainty.

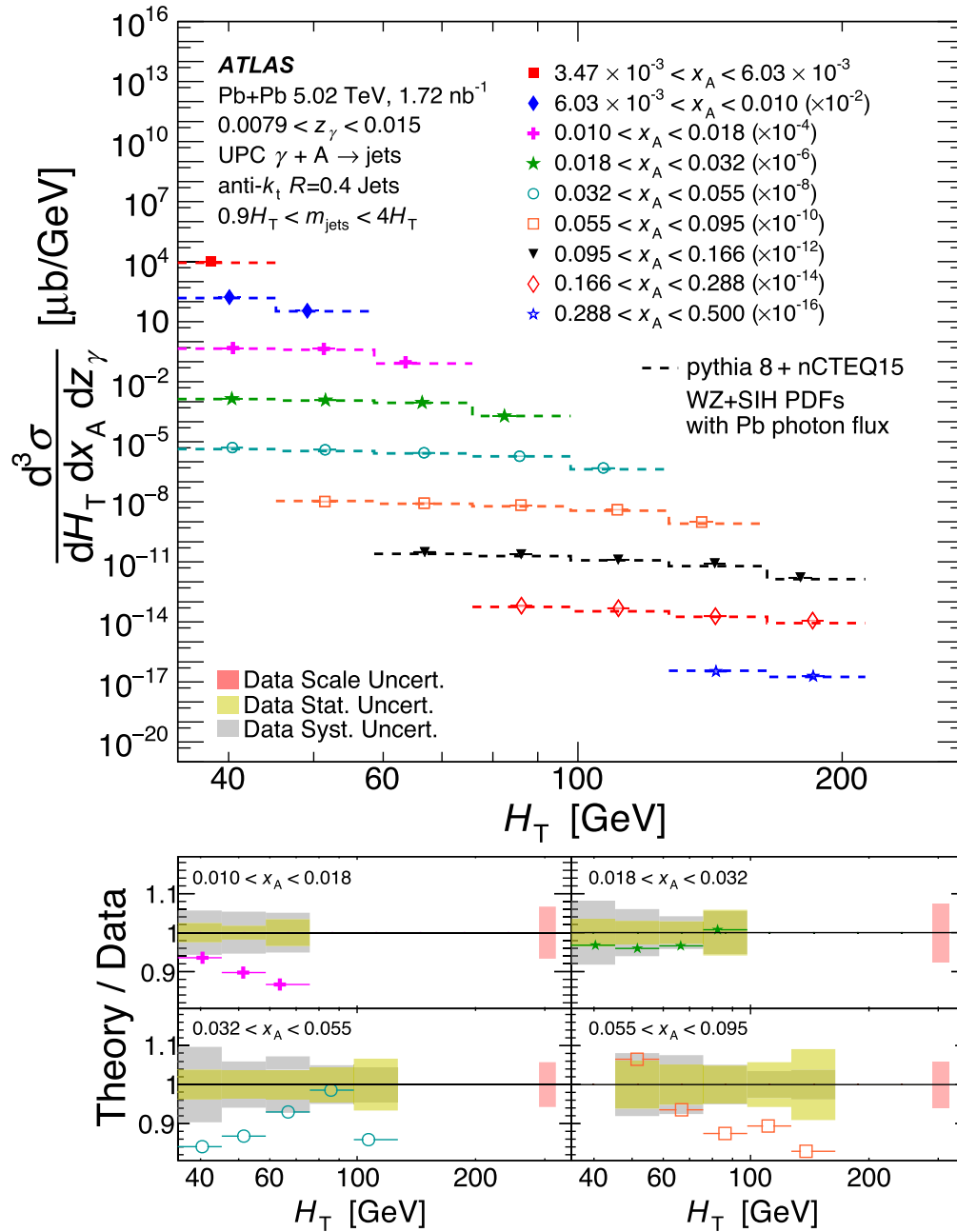


FIG. 34. Triple-differential cross sections, $\frac{d^3\sigma}{dH_T dx_A dz_\gamma}$, as a function of H_T for different bins of x_A for events with emitted photon energies in the kinematic range $0.0079 < z_\gamma < 0.015$. In the upper panel, systematic uncertainties are shown as shaded boxes, while statistical uncertainties shown as vertical lines are usually smaller than the size of the markers. A theoretical comparison is shown to cross sections computed using PYTHIA8 with nCTEQ15 WZ + SIH PDFs, a photon flux from STARLIGHT, and a z_γ -dependent breakup fraction. The bottom panels show the ratio between the theory prediction and data for a representative subset of the bins of x_A . The Lorentz-invariant variables x_A , z_γ , and H_T are unambiguously defined in terms of the particle-level jet kinematics and correspond at leading order to the Bjorken- x , emitted photon energy fraction, and collision Q^2 , respectively. The light red bands in the ratio panels are the quadrature sum of scale uncertainties on the cross section, while the gray band shows the remaining systematic uncertainty. The yellow band shows the point-to-point statistical uncertainty.

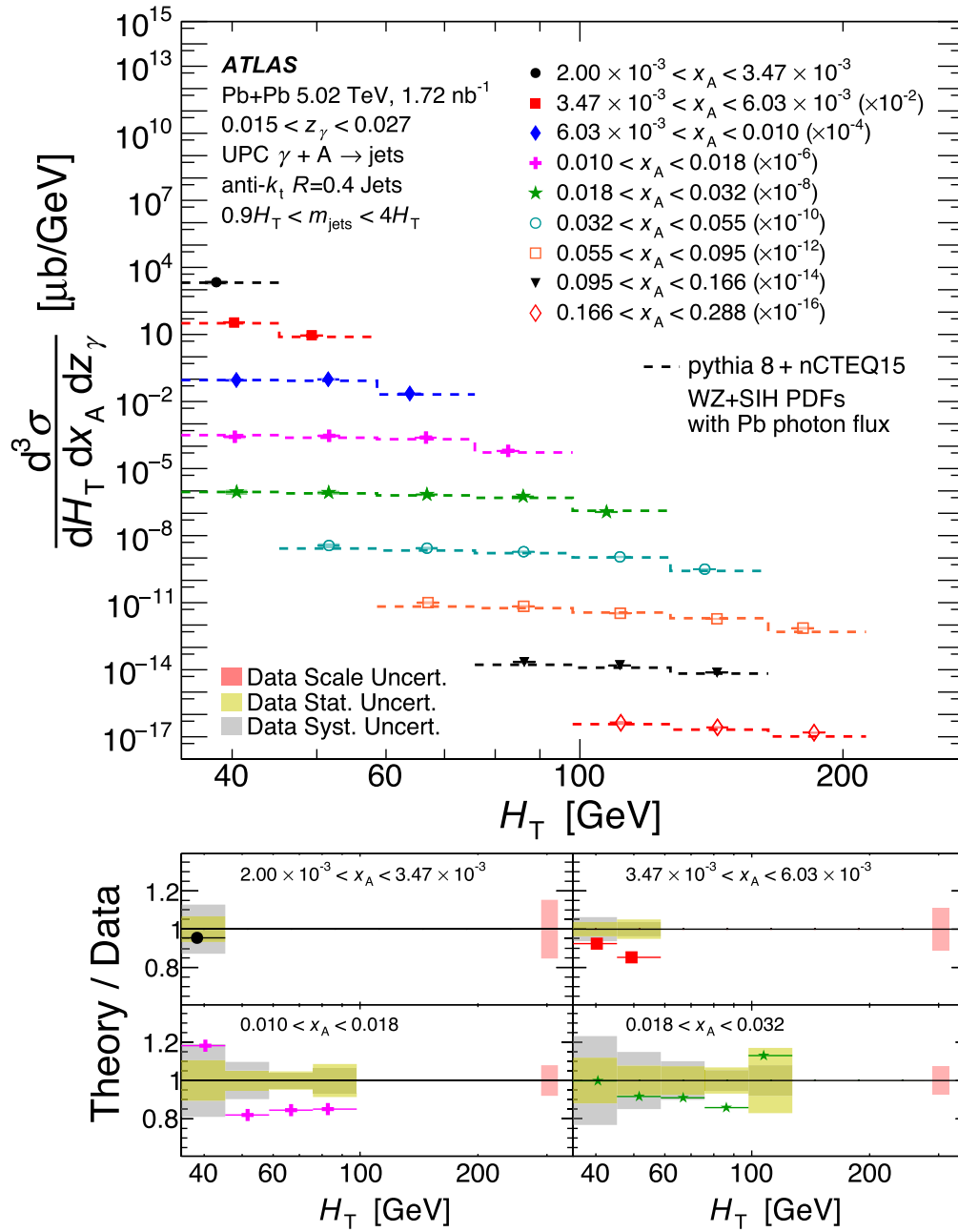


FIG. 35. Triple-differential cross sections, $\frac{d^3\sigma}{dH_T dx_A dz_\gamma}$, as a function of H_T for different bins of x_A for events with emitted photon energies in the kinematic range $0.015 < z_\gamma < 0.027$. In the upper panel, systematic uncertainties are shown as shaded boxes, while statistical uncertainties shown as vertical lines are usually smaller than the size of the markers. A theoretical comparison is shown to cross sections computed using PYTHIA8 with nCTEQ15 WZ + SIH PDFs, a photon flux from STARLIGHT, and a z_γ -dependent breakup fraction. The bottom panels show the ratio between the theory prediction and data for a representative subset of the bins of x_A . The Lorentz-invariant variables x_A , z_γ , and H_T are unambiguously defined in terms of the particle-level jet kinematics and correspond at leading order to the Bjorken- x , emitted photon energy fraction, and collision Q^2 , respectively. The light red bands in the ratio panels are the quadrature sum of scale uncertainties on the cross section, while the gray band shows the remaining systematic uncertainty. The yellow band shows the point-to-point statistical uncertainty.

- [1] H. Paukkunen and C. A. Salgado, Constraints for the nuclear parton distributions from Z and W^\pm production at the LHC, *J. High Energy Phys.* **03** (2011) 071.
- [2] K. J. Eskola, I. Helenius, P. Paakkinen, and H. Paukkunen, A QCD analysis of LHCb D-meson data in p+Pb collisions, *J. High Energy Phys.* **05** (2020) 037.
- [3] K. J. Eskola, P. Paakkinen, and H. Paukkunen, Non-quadratic improved Hessian PDF reweighting and application to CMS dijet measurements at 5.02 TeV, *Eur. Phys. J. C* **79**, 511 (2019).
- [4] J. J. Aubert *et al.*, The ratio of the nucleon structure functions F_2^N for iron and deuterium, *Phys. Lett.* **123B**, 275 (1983).
- [5] J. Pumplin, D. R. Stump, J. Huston, H.-L. Lai, P. Nadolsky, and W.-K. Tung, New generation of parton distributions with uncertainties from global QCD analysis, *J. High Energy Phys.* **07** (2002) 012.
- [6] A. D. Martin, W. J. Stirling, R. S. Thorne, and G. Watt, Parton distributions for the LHC, *Eur. Phys. J. C* **63**, 189 (2009).
- [7] L. A. Harland-Lang, A. D. Martin, P. Motylinski, and R. S. Thorne, Parton distributions in the LHC era: MMHT 2014 PDFs, *Eur. Phys. J. C* **75**, 204 (2015).
- [8] R. D. Ball *et al.* (NNPDF Collaboration), Parton distributions for the LHC run II, *J. High Energy Phys.* **04** (2015) 040.
- [9] M. Walt, I. Helenius, and W. Vogelsang, Open-source QCD analysis of nuclear parton distribution functions at NLO and NNLO, *Phys. Rev. D* **100**, 096015 (2019).
- [10] H. Khanpour, M. Soleymaninia, S. A. Tehrani, H. Spiesberger, and V. Guzey, Nuclear parton distribution functions with uncertainties in a general mass variable flavor number scheme, *Phys. Rev. D* **104**, 034010 (2021).
- [11] R. A. Khalek, J. J. Ethier, J. Rojo, and G. van Weelden, nNNPDF2.0: Quark flavor separation in nuclei from LHC data, *J. High Energy Phys.* **09** (2020) 183.
- [12] I. Helenius, M. Walt, and W. Vogelsang, NNLO nuclear parton distribution functions with electroweak-boson production data from the LHC, *Phys. Rev. D* **105**, 094031 (2022).
- [13] K. J. Eskola, P. Paakkinen, H. Paukkunen, and C. A. Salgado, EPPS21: A global QCD analysis of nuclear PDFs, *Eur. Phys. J. C* **82**, 413 (2022).
- [14] A. Accardi *et al.*, Electron-ion collider: The next QCD frontier, *Eur. Phys. J. A* **52**, 268 (2016).
- [15] M. Klasen and H. Paukkunen, Nuclear PDFs after the first decade of LHC data, *Annu. Rev. Part. Nucl. Sci.* **74**, 49 (2023).
- [16] C. A. Bertulani, S. R. Klein, and J. Nystrand, Physics of ultra-peripheral nuclear collisions, *Annu. Rev. Nucl. Part. Sci.* **55**, 271 (2005).
- [17] A. J. Baltz, The physics of ultraperipheral collisions at the LHC, *Phys. Rep.* **458**, 1 (2008).
- [18] S. Klein and P. Steinberg, Photonuclear and two-photon interactions at high-energy nuclear colliders, *Annu. Rev. Nucl. Part. Sci.* **70**, 323 (2020).
- [19] M. Strikman, R. Vogt, and S. N. White, Probing small x parton densities in ultraperipheral AA and pA collisions at the CERN large hadron collider, *Phys. Rev. Lett.* **96**, 082001 (2006).
- [20] V. Guzey and M. Klasen, Inclusive dijet photoproduction in ultraperipheral heavy ion collisions at the CERN Large Hadron Collider in next-to-leading order QCD, *Phys. Rev. C* **99**, 065202 (2019).
- [21] V. Guzey and M. Klasen, Constraints on nuclear parton distributions from dijet photoproduction at the LHC, *Eur. Phys. J. C* **79**, 396 (2019).
- [22] CMS Collaboration, Constraining gluon distributions in nuclei using dijets in proton–proton and proton–lead collisions at $\sqrt{s_{NN}} = 5.02$ TeV, *Phys. Rev. Lett.* **121**, 062002 (2018).
- [23] ATLAS Collaboration, Measurement of the centrality dependence of the dijet yield in $p + \text{Pb}$ collisions at $\sqrt{s_{NN}} = 8.16$ TeV with the ATLAS detector, *Phys. Rev. Lett.* **132**, 102301 (2023).
- [24] J. D. Jackson, *Classical Electrodynamics*, 3rd ed. (Wiley, New York, NY, 1999), ISBN: 9780471309321.
- [25] T. Sjöstrand, S. Ask, J. R. Christiansen, R. Corke, N. Desai, P. Ilten, S. Mrenna, S. Prestel, C. O. Rasmussen, and P. Z. Skands, An introduction to PYTHIA 8.2, *Comput. Phys. Commun.* **191**, 159 (2015).
- [26] ATLAS Collaboration, Exclusive dimuon production in ultraperipheral Pb + Pb collisions at $\sqrt{s_{NN}} = 5.02$ TeV with ATLAS, *Phys. Rev. C* **104**, 024906 (2021).
- [27] ATLAS Collaboration, Exclusive dielectron production in ultraperipheral Pb + Pb collisions at $\sqrt{s_{NN}} = 5.02$ TeV with ATLAS, *J. High Energy Phys.* **06** (2023) 182.
- [28] CMS Collaboration, Observation of forward neutron multiplicity dependence of dimuon acoplanarity in ultraperipheral Pb–Pb collisions at $\sqrt{s_{NN}} = 5.02$ TeV, *Phys. Rev. Lett.* **127**, 122001 (2021).
- [29] ATLAS Collaboration, Observation of the $\gamma\gamma \rightarrow \tau\tau$ process in Pb + Pb collisions and constraints on the τ -lepton anomalous magnetic moment with the ATLAS detector, *Phys. Rev. Lett.* **131**, 151802 (2023).
- [30] L. A. Harland-Lang, M. Tasevsky, V. A. Khoze, and M. G. Ryskin, A new approach to modelling elastic and inelastic photon-initiated production at the LHC: SuperChic 4, *Eur. Phys. J. C* **80**, 925 (2020).
- [31] L. A. Harland-Lang, V. A. Khoze, and M. G. Ryskin, Elastic photon-initiated production at the LHC: The role of hadron-hadron interactions, *SciPost Phys.* **11**, 064 (2021).
- [32] L. A. Harland-Lang, Exciting ions: A systematic treatment of ultraperipheral heavy ion collisions with nuclear breakup, *Phys. Rev. D* **107**, 093004 (2023).
- [33] F. Cornet, P. Jankowski, M. Krawczyk, and A. Lorca, A new five flavor LO analysis and parametrization of parton distributions in the real photon, *Phys. Rev. D* **68**, 014010 (2003).
- [34] ATLAS Collaboration, Two-particle azimuthal correlations in photonuclear ultraperipheral Pb + Pb collisions at 5.02 TeV with ATLAS, *Phys. Rev. C* **104**, 014903 (2021).
- [35] G. Baur, K. Hencken, and D. Trautmann, Photon-photon physics in very peripheral collisions of relativistic heavy ions, *J. Phys. G* **24**, 1657 (1998).
- [36] G. Baur, K. Hencken, D. Trautmann, S. Sadovsky, and Y. Kharlov, Coherent $\gamma\gamma$ and γ -A interactions in very peripheral collisions at relativistic ion colliders, *Phys. Rep.* **364**, 359 (2002).

- [37] I. A. Pshenichnov, I. N. Mishustin, J. P. Bondorf, A. S. Botvina, and A. S. Ilinov, Nuclear multifragmentation induced by electromagnetic fields of ultrarelativistic heavy ions, *Phys. Rev. C* **57**, 1920 (1998).
- [38] A. Veysi, H. Beil, R. Bergere, P. Carlos, and A. Lepretre, Photoneutron cross sections of ^{208}Pb and ^{197}Au , *Nucl. Phys.* **A159**, 561 (1970).
- [39] A. J. Baltz, S. R. Klein, and J. Nystrand, Coherent vector-meson photoproduction with nuclear breakup in relativistic heavy-ion collisions, *Phys. Rev. Lett.* **89**, 012301 (2002).
- [40] M. Cacciari, G. P. Salam, and G. Soyez, The anti- k_t jet clustering algorithm, *J. High Energy Phys.* **04** (2008) 063.
- [41] M. Cacciari, G. P. Salam, and G. Soyez, FastJet user manual, *Eur. Phys. J. C* **72**, 1896 (2012).
- [42] ATLAS Collaboration, The ATLAS experiment at the CERN large hadron collider, *J. Instrum.* **3**, S08003 (2008).
- [43] ATLAS Collaboration, ATLAS insertable B-layer: Technical design report, Reports No. ATLAS-TDR-19, No. CERN-LHCC-2010-013, 2010, <https://cds.cern.ch/record/1291633>; Addendum: Reports No. ATLAS-TDR-19-ADD-1, No. CERN-LHCC-2012-009, 2012, <https://cds.cern.ch/record/1451888>.
- [44] B. Abbott *et al.*, Production and integration of the ATLAS insertable B-layer, *J. Instrum.* **13**, T05008 (2018).
- [45] G. Avoni *et al.*, The new LUCID-2 detector for luminosity measurement and monitoring in ATLAS, *J. Instrum.* **13**, P07017 (2018).
- [46] ATLAS Collaboration, Performance of the ATLAS trigger system in 2015, *Eur. Phys. J. C* **77**, 317 (2017).
- [47] ATLAS Collaboration, Software and computing for Run 3 of the ATLAS experiment at the LHC, [arXiv:2404.06335](https://arxiv.org/abs/2404.06335).
- [48] ALICE Collaboration, Measurement of the cross section for electromagnetic dissociation with neutron emission in Pb-Pb collisions at $\sqrt{s_{\text{NN}}}=2.76$ TeV, *Phys. Rev. Lett.* **109**, 252302 (2012).
- [49] H. H. Braun, A. Fassò, A. Ferrari, J. M. Jowett, P. R. Sala, and G. I. Smirnov, Hadronic and electromagnetic fragmentation of ultrarelativistic heavy ions at LHC, *Phys. Rev. ST Accel. Beams* **17**, 021006 (2014).
- [50] M. Klusek-Gawenda, M. Ciemala, W. Schäfer, and A. Szczurek, Electromagnetic excitation of nuclei and neutron evaporation in ultrarelativistic ultraperipheral heavy ion collisions, *Phys. Rev. C* **89**, 054907 (2014).
- [51] ATLAS Collaboration, Topological cell clustering in the ATLAS calorimeters and its performance in LHC Run 1, *Eur. Phys. J. C* **77**, 490 (2017).
- [52] I. Helenius, Simulations of photo-nuclear dijets with Pythia 8 and their sensitivity to nuclear PDFs, *Proc. Sci.*, DIS2018 (2018) 113 [[arXiv:1806.07326](https://arxiv.org/abs/1806.07326)].
- [53] S. R. Klein, J. Nystrand, J. Seger, Y. Gorbunov, and J. Butterworth, STARlight: A Monte Carlo simulation program for ultra-peripheral collisions of relativistic ions, *Comput. Phys. Commun.* **212**, 258 (2017).
- [54] K. Kovarik *et al.*, nCTEQ15: Global analysis of nuclear parton distributions with uncertainties in the CTEQ framework, *Phys. Rev. D* **93**, 085037 (2016).
- [55] ATLAS Collaboration, ATLAS Pythia 8 tunes to 7 TeV data, Report No. ATL-PHYS-PUB-2014-021, 2014, <https://cds.cern.ch/record/1966419>.
- [56] S. Agostinelli *et al.*, GEANT4—a simulation toolkit, *Nucl. Instrum. Methods Phys. Res., Sect. A* **506**, 250 (2003).
- [57] ATLAS Collaboration, The ATLAS simulation infrastructure, *Eur. Phys. J. C* **70**, 823 (2010).
- [58] ATLAS Collaboration, Charged-particle distributions in $\sqrt{s} = 13$ TeV pp interactions measured with the ATLAS detector at the LHC, *Phys. Lett. B* **758**, 67 (2016).
- [59] ATLAS Collaboration, Jet reconstruction and performance using particle flow with the ATLAS detector, *Eur. Phys. J. C* **77**, 466 (2017).
- [60] ATLAS Collaboration, Jet energy scale and resolution measured in proton-proton collisions at $\sqrt{s} = 13$ TeV with the ATLAS detector, *Eur. Phys. J. C* **81**, 689 (2021).
- [61] ATLAS Collaboration, Rapidity gap cross sections measured with the ATLAS detector in pp collisions at $\sqrt{s} = 7$ TeV, *Eur. Phys. J. C* **72**, 1926 (2012).
- [62] ATLAS Collaboration, ATLAS data quality operations and performance for 2015–2018 data-taking, *J. Instrum.* **15**, P04003 (2020).
- [63] ATLAS Collaboration, Reconstruction of primary vertices at the ATLAS experiment in Run 1 proton-proton collisions at the LHC, *Eur. Phys. J. C* **77**, 332 (2017).
- [64] ATLAS Collaboration, Comparison between simulated and observed LHC beam backgrounds in the ATLAS experiment at $E_{\text{beam}} = 4$ TeV, *J. Instrum.* **13**, P12006 (2018).
- [65] ATLAS Collaboration, Luminosity determination in pp collisions at $\sqrt{s} = 13$ TeV using the ATLAS detector at the LHC, *Eur. Phys. J. C* **83**, 982 (2023).
- [66] G. D'Agostini, A multidimensional unfolding method based on Bayes' theorem, *Nucl. Instrum. Methods Phys. Res., Sect. A* **362**, 487 (1995).
- [67] L. B. Lucy, An iterative technique for the rectification of observed distributions, *Astron. J.* **79**, 745 (1974).
- [68] W. H. Richardson, Bayesian-based iterative method of image restoration, *J. Opt. Soc. Am.* **62**, 55 (1972).
- [69] T. Adye, Unfolding algorithms and tests using RooUnfold, *Proceedings, 2011 Workshop on Statistical Issues Related to Discovery Claims in Search Experiments and Unfolding (PHYSTAT 2011)* (CERN, Geneva, Switzerland, 2011), p. 313.
- [70] K. J. Eskola, V. Guzey, I. Helenius, P. Paakkinen, and H. Paukkunen, Spatial resolution of dijet photoproduction in near-encounter ultraperipheral nuclear collisions, *Phys. Rev. C* **110**, 054906 (2024).
- [71] P. Duwentäster, L. A. Husová, T. Ježo, M. Klasen, K. Kovařík, A. Kusina, K. F. Muzakka, F. I. Olness, I. Schienbein, and J. Y. Yu, Impact of inclusive hadron production data on nuclear gluon PDFs, *Phys. Rev. D* **104**, 094005 (2021).
- [72] R. Abdul Khalek, R. Gauld, T. Giani, E. R. Nocera, T. R. Rabemananjara, and J. Rojo, nNNPDF3.0: Evidence for a modified partonic structure in heavy nuclei, *Eur. Phys. J. C* **82**, 507 (2022).
- [73] T.-J. Hou *et al.*, New CTEQ global analysis of quantum chromodynamics with high-precision data from the LHC, *Phys. Rev. D* **103**, 014013 (2021).
- [74] R. D. Ball *et al.*, The PDF4LHC21 combination of global PDF fits for the LHC Run III, *J. Phys. G* **49**, 080501 (2022).

- [75] ATLAS Collaboration, Observation of $t\bar{t}$ production in the lepton + jets and dilepton channels in $p + \text{Pb}$ collisions at $\sqrt{s_{\text{NN}}} = 8.16$ TeV with the ATLAS detector, *J. High Energy Phys.* **11** (2024) 101.
- [76] ATLAS Collaboration, ATLAS computing acknowledgements, Report No. ATL-SOFT-PUB-2023-001, 2023, <https://cds.cern.ch/record/2869272>.
- [77] CERN Open Data Policy for the LHC Experiments, Report No. CERN-OPEN-2020-013, CERN, Geneva, 2020, <https://cds.cern.ch/record/2745133>.
- [78] <https://www.hepdata.net/record/156979>
- [79] J. Bellm *et al.*, Herwig 7.0/Herwig++ 3.0 release note, *Eur. Phys. J. C* **76**, 196 (2016).
- [80] S. Alioli, P. Nason, C. Oleari, and E. Re, A general framework for implementing NLO calculations in shower Monte Carlo programs: the POWHEG BOX, *J. High Energy Phys.* **06** (2010) 043.
- [81] S. Alioli, P. Nason, C. Oleari, and E. Re, NLO vector-boson production matched with shower in POWHEG, *J. High Energy Phys.* **07** (2008) 060.
- [82] E. Bothmann *et al.*, Event generation with Sherpa 2.2, *SciPost Phys.* **7**, 034 (2019).
- [83] R. D. Ball *et al.* (NNPDF Collaboration), Parton distributions with LHC data, *Nucl. Phys.* **B867**, 244 (2013).
- [84] ATLAS Collaboration, Evaluating statistical uncertainties and correlations using the bootstrap method, Report No. ATL-PHYS-PUB-2021-011, 2021, <https://cds.cern.ch/record/2759945>.
- [85] ATLAS Collaboration, New techniques for jet calibration with the ATLAS detector, *Eur. Phys. J. C* **83**, 761 (2023).
- [86] ATLAS Collaboration, Jet energy measurement with the ATLAS detector in proton–proton collisions at $\sqrt{s} = 7$ TeV, *Eur. Phys. J. C* **73**, 2304 (2013).

G. Aad¹⁰⁵, E. Aakvaag¹⁷, B. Abbott¹²⁴, S. Abdelhameed^{120a}, K. Abeling⁵⁷, N. J. Abicht⁵¹, S. H. Abidi³⁰, M. Aboelela⁴⁶, A. Aboulhorma^{36e}, H. Abramowicz¹⁵⁶, H. Abreu¹⁵⁵, Y. Abulaiti¹²¹, B. S. Acharya^{71a,71b,b}, A. Ackermann^{65a}, C. Adam Bourdarios⁴, L. Adamczyk^{88a}, S. V. Addepalli²⁷, M. J. Addison¹⁰⁴, J. Adelman¹¹⁹, A. Adiguzel^{22c}, T. Adaye¹³⁸, A. A. Affolder¹⁴⁰, Y. Afik⁴¹, M. N. Agaras¹³, J. Agarwala^{75a,75b}, A. Aggarwal¹⁰³, C. Agheorghiesei^{28c}, F. Ahmadov^{40,c}, W. S. Ahmed¹⁰⁷, S. Ahuja⁹⁸, X. Ai^{64e}, G. Aielli^{78a,78b}, A. Aikot¹⁶⁸, M. Ait Tamlihat^{36e}, B. Aitbenchikh^{36a}, M. Akbiyik¹⁰³, T. P. A. Åkesson¹⁰¹, A. V. Akimov¹⁵⁰, D. Akiyama¹⁷³, N. N. Akolkar²⁵, S. Aktas^{22a}, K. Al Houry⁴³, G. L. Alberghi^{24b}, J. Albert¹⁷⁰, P. Albicocco⁵⁵, G. L. Albouy⁶², S. Alderweireldt⁵⁴, Z. L. Alegria¹²⁵, M. Aleksa³⁷, I. N. Aleksandrov⁴⁰, C. Alexa^{28b}, T. Alexopoulos¹⁰, F. Alfonsi^{24b}, M. Algren⁵⁸, M. Alhroob¹⁷², B. Ali¹³⁶, H. M. J. Ali^{94,d}, S. Ali³², S. W. Alibocus⁹⁵, M. Aliev^{34c}, G. Alimonti^{73a}, W. Alkahi⁵⁷, C. Allaire⁶⁸, B. M. M. Allbrooke¹⁵¹, J. S. Allen¹⁰⁴, J. F. Allen⁵⁴, C. A. Allendes Flores^{141f}, P. P. Allport²¹, A. Aloisio^{74a,74b}, F. Alonso⁹³, C. Alpigiani¹⁴³, Z. M. K. Alsolami⁹⁴, M. Alvarez Estevez¹⁰², A. Alvarez Fernandez¹⁰³, M. Alves Cardoso⁵⁸, M. G. Alviggi^{74a,74b}, M. Aly¹⁰⁴, Y. Amaral Coutinho^{85b}, A. Ambler¹⁰⁷, C. Amelung³⁷, M. Amerl¹⁰⁴, C. G. Ames¹¹², D. Amidei¹⁰⁹, B. Amini⁵⁶, K. J. Amirie¹⁵⁹, S. P. Amor Dos Santos^{134a}, K. R. Amos¹⁶⁸, D. Amperiadou¹⁵⁷, S. An⁸⁶, V. Ananiev¹²⁹, C. Anastopoulos¹⁴⁴, T. Andeen¹¹, J. K. Anders³⁷, A. C. Anderson⁶¹, S. Y. Andreato^{49a,49b}, A. Andreatza^{73a,73b}, S. Angelidakis⁹, A. Angerami⁴³, A. V. Anisenkov³⁹, A. Annovi^{76a}, C. Antel⁵⁸, E. Antipov¹⁵⁰, M. Antonelli⁵⁵, F. Anulli^{77a}, M. Aoki⁸⁶, T. Aoki¹⁵⁸, M. A. Aparo¹⁵¹, L. Aperio Bella⁵⁰, C. Appelt¹⁵⁶, A. Apyan²⁷, S. J. Arbiol Val⁸⁹, C. Arcangeletti⁵⁵, A. T. H. Arce⁵³, J-F. Arguin¹¹¹, S. Argyropoulos¹⁵⁷, J.-H. Arling⁵⁰, O. Arnaez⁴, H. Arnold¹⁵⁰, G. Artoni^{77a,77b}, H. Asada¹¹⁴, K. Asai¹²², S. Asai¹⁵⁸, N. A. Asbah³⁷, R. A. Ashby Pickering¹⁷², K. Assamagan³⁰, R. Astalos^{29a}, K. S. V. Astrand¹⁰¹, S. Atashi¹⁶³, R. J. Atkin^{34a}, M. Atkinson¹⁶⁷, H. Atmani^{36f}, P. A. Atmasiddha¹³², K. Augsten¹³⁶, S. Auricchio^{74a,74b}, A. D. Auriol²¹, V. A. Austrup¹⁰⁴, G. Avolio³⁷, K. Axiotis⁵⁸, G. Azuelos^{111,e}, D. Babal^{29b}, H. Bachacou¹³⁹, K. Bachas^{157,f}, A. Bachiu³⁵, E. Bachmann⁵², F. Backman^{49a,49b}, A. Badea⁴¹, T. M. Baer¹⁰⁹, P. Bagnaia^{77a,77b}, M. Bahmani¹⁹, D. Bahner⁵⁶, K. Bai¹²⁷, J. T. Baines¹³⁸, L. Baines⁹⁷, O. K. Baker¹⁷⁷, E. Bakos¹⁶, D. Bakshi Gupta⁸, L. E. Balabram Filho^{85b}, V. Balakrishnan¹²⁴, R. Balasubramanian⁴, E. M. Baldin³⁹, P. Balek^{88a}, E. Ballabene^{24b,24a}, F. Balli¹³⁹, L. M. Baltés^{65a}, W. K. Balunas³³, J. Balz¹⁰³, I. Bamwidhi^{120b}, E. Banas⁸⁹, M. Bandieramonte¹³³, A. Bandyopadhyay²⁵, S. Bansal²⁵, L. Barak¹⁵⁶, M. Barakat⁵⁰, E. L. Barberio¹⁰⁸, D. Barberis^{59b,59a}, M. Barbero¹⁰⁵, M. Z. Barel¹¹⁸, T. Barillari¹¹³, M-S. Barisits³⁷, T. Barklow¹⁴⁸, P. Baron¹²⁶, D. A. Baron Moreno¹⁰⁴, A. Baroncelli^{64a}, A. J. Barr¹³⁰, J. D. Barr⁹⁹, F. Barreiro¹⁰², J. Barreiro Guimarães da Costa¹⁴, U. Barron¹⁵⁶, M. G. Barros Teixeira^{134a}, S. Barsov³⁹, F. Bartels^{65a}, R. Bartoldus¹⁴⁸, A. E. Barton⁹⁴, P. Bartos^{29a}, A. Basan¹⁰³, M. Baselga⁵¹, A. Bassalat^{68,g}, M. J. Basso^{160a}, S. Bataju⁴⁶, R. Bate¹⁶⁹, R. L. Bates⁶¹, S. Batlamous¹⁰², B. Batool¹⁴⁶, M. Battaglia¹⁴⁰, D. Battulga¹⁹

M. Bauce^{77a,77b} M. Bauer⁸¹ P. Bauer²⁵ L. T. Bazzano Hurrell³¹ J. B. Beacham⁵³ T. Beau¹³¹
 J. Y. Beaucamp⁹³ P. H. Beauchemin¹⁶² P. Bechtler²⁵ H. P. Beck^{20,h} K. Becker¹⁷² A. J. Beddall⁸⁴
 V. A. Bednyakov⁴⁰ C. P. Bee¹⁵⁰ L. J. Beemster¹⁶ T. A. Beermann³⁷ M. Begalli^{85d} M. Begel³⁰ A. Behera¹⁵⁰
 J. K. Behr⁵⁰ J. F. Beirer³⁷ F. Beisiegel²⁵ M. Belfkir^{120b} G. Bella¹⁵⁶ L. Bellagamba^{24b} A. Bellerive³⁵
 P. Bellos²¹ K. Beloborodov³⁹ D. Benchekroun^{36a} F. Bendebba^{36a} Y. Benhammou¹⁵⁶ K. C. Benkendorfer⁶³
 L. Beresford⁵⁰ M. Beretta⁵⁵ E. Bergeas Kuutmann¹⁶⁶ N. Berger⁴ B. Bergmann¹³⁶ J. Beringer^{18a}
 G. Bernardi⁵ C. Bernius¹⁴⁸ F. U. Bernlochner²⁵ F. Bernon³⁷ A. Berrocal Guardia¹³ T. Berry⁹⁸ P. Berta¹³⁷
 A. Berthold⁵² S. Bethke¹¹³ A. Betti^{77a,77b} A. J. Bevan⁹⁷ N. K. Bhalla⁵⁶ S. Bhatta¹⁵⁰ D. S. Bhattacharya¹⁷¹
 P. Bhattarai¹⁴⁸ Z. M. Bhatti¹²¹ K. D. Bhide⁵⁶ V. S. Bhopatkar¹²⁵ R. M. Bianchi¹³³ G. Bianco^{24b,24a}
 O. Biebel¹¹² R. Bielski¹²⁷ M. Biglietti^{79a} C. S. Billingsley⁴⁶ Y. Bimgdi^{36f} M. Bindi⁵⁷ A. Bingham¹⁷⁶
 A. Bingul^{22b} C. Bini^{77a,77b} G. A. Bird³³ M. Birman¹⁷⁴ M. Biros¹³⁷ S. Biryukov¹⁵¹ T. Bisanz⁵¹
 E. Bisceglie^{45b,45a} J. P. Biswal¹³⁸ D. Biswas¹⁴⁶ I. Bloch⁵⁰ A. Blue⁶¹ U. Blumenschein⁹⁷ J. Blumenthal¹⁰³
 V. S. Bobrovnikov³⁹ M. Boehler⁵⁶ B. Boehm¹⁷¹ D. Bogavac³⁷ A. G. Bogdanchikov³⁹ L. S. Boggia¹³¹
 C. Bohm^{49a} V. Boisvert⁹⁸ P. Bokan³⁷ T. Bold^{88a} M. Bomben⁵ M. Bona⁹⁷ M. Boonekamp¹³⁹
 C. D. Booth⁹⁸ A. G. Borbély⁶¹ I. S. Bordulev³⁹ G. Borissov⁹⁴ D. Bortoletto¹³⁰ D. Boscherini^{24b}
 M. Bosman¹³ J. D. Bossio Sola³⁷ K. Bouaouda^{36a} N. Bouchhar¹⁶⁸ L. Boudet⁴ J. Boudreau¹³³
 E. V. Bouhova-Thacker⁹⁴ D. Boumediene⁴² R. Bouquet^{59b,59a} A. Boveia¹²³ J. Boyd³⁷ D. Boye³⁰
 I. R. Boyko⁴⁰ L. Bozianu⁵⁸ J. Bracnik²¹ N. Brahimi⁴ G. Brandt¹⁷⁶ O. Brandt³³ F. Braren⁵⁰ B. Brau¹⁰⁶
 J. E. Brau¹²⁷ R. Brenner¹⁷⁴ L. Brenner¹¹⁸ R. Brenner¹⁶⁶ S. Bressler¹⁷⁴ G. Brianti^{80a,80b} D. Britton⁶¹
 D. Britzger¹¹³ I. Brock²⁵ R. Brock¹¹⁰ G. Brooijmans⁴³ A. J. Brooks⁷⁰ E. M. Brooks^{160b} E. Brost³⁰
 L. M. Brown¹⁷⁰ L. E. Bruce⁶³ T. L. Bruckler¹³⁰ P. A. Bruckman de Renstrom⁸⁹ B. Brüers⁵⁰ A. Bruni^{24b}
 G. Bruni^{24b} M. Bruschi^{24b} N. Bruscinò^{77a,77b} T. Buanes¹⁷ Q. Buat¹⁴³ D. Buchin¹¹³ A. G. Buckley⁶¹
 O. Bulekov³⁹ B. A. Bullard¹⁴⁸ S. Burdin⁹⁵ C. D. Burgard⁵¹ A. M. Burger³⁷ B. Burghgrave⁸
 O. Burlayenko⁵⁶ J. Bursleson¹⁶⁷ J. T. P. Burr³³ J. C. Burzynski¹⁴⁷ E. L. Busch⁴³ V. Büscher¹⁰³ P. J. Bussey⁶¹
 J. M. Butler²⁶ C. M. Buttar⁶¹ J. M. Butterworth⁹⁹ W. Buttinger¹³⁸ C. J. Buxo Vazquez¹¹⁰ A. R. Buzykaev³⁹
 S. Cabrera Urbán¹⁶⁸ L. Cadamuro⁶⁸ D. Caforio⁶⁰ H. Cai¹³³ Y. Cai^{14,115c} Y. Cai^{115a} V. M. M. Cairo³⁷
 O. Cakir^{3a} N. Calace³⁷ P. Calafiura^{18a} G. Calderini¹³¹ P. Calfayan³⁵ G. Callea⁶¹ L. P. Caloba^{85b} D. Calvet⁴²
 S. Calvet⁴² M. Calvetti^{76a,76b} R. Camacho Toro¹³¹ S. Camarda³⁷ D. Camarero Munoz²⁷ P. Camarri^{78a,78b}
 M. T. Camerlingo^{74a,74b} D. Cameron³⁷ C. Camincher¹⁷⁰ M. Campanelli⁹⁹ A. Camplani⁴⁴ V. Canale^{74a,74b}
 A. C. Canbay^{3a} E. Canonero⁹⁸ J. Cantero¹⁶⁸ Y. Cao¹⁶⁷ F. Capocasa²⁷ M. Capua^{45b,45a} A. Carbone^{73a,73b}
 R. Cardarelli^{78a} J. C. J. Cardenas⁸ G. Carducci^{45b,45a} T. Carli³⁷ G. Carlino^{74a} J. I. Carlotto¹³
 B. T. Carlson^{133,i} E. M. Carlson^{170,160a} J. Carmignani⁹⁵ L. Carminati^{73a,73b} A. Carnelli¹³⁹ M. Carnesale³⁷
 S. Caron¹¹⁷ E. Carquin^{141f} I. B. Carr¹⁰⁸ S. Carrá^{73a} G. Carratta^{24b,24a} A. M. Carroll¹²⁷ M. P. Casado^{13,j}
 M. Caspar⁵⁰ F. L. Castillo⁴ L. Castillo Garcia¹³ V. Castillo Gimenez¹⁶⁸ N. F. Castro^{134a,134e} A. Catinaccio³⁷
 J. R. Catmore¹²⁹ T. Cavaliere⁴ V. Cavaliere³⁰ N. Cavalli^{24b,24a} L. J. Caviedes Betancourt^{23b}
 Y. C. Cekmecelioglu⁵⁰ E. Celebi⁸⁴ S. Cella³⁷ M. S. Centonze^{72a,72b} V. Cepaitis⁵⁸ K. Cerny¹²⁶
 A. S. Cerqueira^{85a} A. Cerri¹⁵¹ L. Cerrito^{78a,78b} F. Cerutti^{18a} B. Cervato¹⁴⁶ A. Cervelli^{24b} G. Cesarini⁵⁵
 S. A. Cetin⁸⁴ D. Chakraborty¹¹⁹ J. Chan^{18a} W. Y. Chan¹⁵⁸ J. D. Chapman³³ E. Chapon¹³⁹
 B. Chargeishvili^{154b} D. G. Charlton²¹ M. Chatterjee²⁰ C. Chauhan¹³⁷ Y. Che^{115a} S. Chekanov⁶
 S. V. Chekulaev^{160a} G. A. Chelkov^{40,k} A. Chen¹⁰⁹ B. Chen¹⁵⁶ B. Chen¹⁷⁰ H. Chen^{115a} H. Chen³⁰
 J. Chen^{64c} J. Chen¹⁴⁷ M. Chen¹³⁰ S. Chen⁹⁰ S. J. Chen^{115a} X. Chen^{64c} X. Chen^{15,l} Y. Chen^{64a}
 C. L. Cheng¹⁷⁵ H. C. Cheng^{66a} S. Cheong¹⁴⁸ A. Cheplakov⁴⁰ E. Cheremushkina⁵⁰ E. Cherepanova¹¹⁸
 R. Cherkaoui El Moursli^{36e} E. Cheu⁷ K. Cheung⁶⁷ L. Chevalier¹³⁹ V. Chiarella⁵⁵ G. Chiarelli^{76a}
 N. Chiedde¹⁰⁵ G. Chiodini^{72a} A. S. Chisholm²¹ A. Chitan^{28b} M. Chitishvili¹⁶⁸ M. V. Chizhov^{40,m} K. Choi¹¹
 Y. Chou¹⁴³ E. Y. S. Chow¹¹⁷ K. L. Chu¹⁷⁴ M. C. Chu^{66a} X. Chu^{14,115c} Z. Chubinidze⁵⁵ J. Chudoba¹³⁵
 J. J. Chwastowski⁸⁹ D. Cieri¹¹³ K. M. Ciesla^{88a} V. Cindro⁹⁶ A. Ciocio^{18a} F. Ciroto^{74a,74b} Z. H. Citron¹⁷⁴
 M. Citterio^{73a} D. A. Ciubotaru^{28b} A. Clark⁵⁸ P. J. Clark⁵⁴ N. Clarke Hall⁹⁹ C. Clarry¹⁵⁹
 J. M. Clavijo Columbie⁵⁰ S. E. Clawson⁵⁰ C. Clement^{49a,49b} Y. Coadou¹⁰⁵ M. Cobal^{71a,71c} A. Coccaro^{59b}
 R. F. Coelho Barrue^{134a} R. Coelho Lopes De Sa¹⁰⁶ S. Coelli^{73a} L. S. Colangeli¹⁵⁹ B. Cole⁴³ J. Collot⁶²

P. Conde Muiño^{134a,134g} M. P. Connell^{34c} S. H. Connell^{34c} E. I. Conroy¹³⁰ F. Conventi^{74a,n} H. G. Cooke²¹
 A. M. Cooper-Sarkar¹³⁰ F. A. Corchia^{24b,24a} A. Cordeiro Oudot Choi¹³¹ L. D. Corpe⁴² M. Corradi^{77a,77b}
 F. Corriveau^{107,o} A. Cortes-Gonzalez¹⁹ M. J. Costa¹⁶⁸ F. Costanza⁴ D. Costanzo¹⁴⁴ B. M. Cote¹²³
 J. Couthures⁴ G. Cowan⁹⁸ K. Cranmer¹⁷⁵ L. Cremer⁵¹ D. Cremonini^{24b,24a} S. Crépé-Renaudin⁶²
 F. Crescioli¹³¹ M. Cristinziani¹⁴⁶ M. Cristoforetti^{80a,80b} V. Croft¹¹⁸ J. E. Crosby¹²⁵ G. Crosetti^{45b,45a}
 A. Cueto¹⁰² H. Cui⁹⁹ Z. Cui⁷ W. R. Cunningham⁶¹ F. Curcio¹⁶⁸ J. R. Curran⁵⁴ P. Czodrowski³⁷
 M. J. Da Cunha Sargedas De Sousa^{59b,59a} J. V. Da Fonseca Pinto^{85b} C. Da Via¹⁰⁴ W. Dabrowski^{88a} T. Dado³⁷
 S. Dahbi¹⁵³ T. Dai¹⁰⁹ D. Dal Santo²⁰ C. Dallapiccola¹⁰⁶ M. Dam⁴⁴ G. D'amen³⁰ V. D'Amico¹¹²
 J. Damp¹⁰³ J. R. Dandoy³⁵ D. Dannheim³⁷ M. Danninger¹⁴⁷ V. Dao¹⁵⁰ G. Darbo^{59b} S. J. Das³⁰
 F. Dattola⁵⁰ S. D'Auria^{73a,73b} A. D'Avanzo^{74a,74b} C. David^{34a} T. Davidek¹³⁷ I. Dawson⁹⁷ H. A. Day-hall¹³⁶
 K. De⁸ R. De Asmundis^{74a} N. De Biase⁵⁰ S. De Castro^{24b,24a} N. De Groot¹¹⁷ P. de Jong¹¹⁸ H. De la Torre¹¹⁹
 A. De Maria^{115a} A. De Salvo^{77a} U. De Sanctis^{78a,78b} F. De Santis^{72a,72b} A. De Santo¹⁵¹
 J. B. De Vivie De Regie⁶² J. Debevc⁹⁶ D. V. Dedovich⁴⁰ J. Degens⁹⁵ A. M. Deiana⁴⁶ F. Del Corso^{24b,24a}
 J. Del Peso¹⁰² L. Delagrangé¹³¹ F. Deliot¹³⁹ C. M. Delitzsch⁵¹ M. Della Pietra^{74a,74b} D. Della Volpe⁵⁸
 A. Dell'Acqua³⁷ L. Dell'Asta^{73a,73b} M. Delmastro⁴ C. C. Delogu¹⁰³ P. A. Delsart⁶² S. Demers¹⁷⁷
 M. Demichev⁴⁰ S. P. Denisov³⁹ L. D'Eramo⁴² D. Derendarz⁸⁹ F. Derue¹³¹ P. Dervan⁹⁵ K. Desch²⁵
 C. Deutsch²⁵ F. A. Di Bello^{59b,59a} A. Di Ciaccio^{78a,78b} L. Di Ciaccio⁴ A. Di Domenico^{77a,77b}
 C. Di Donato^{74a,74b} A. Di Girolamo³⁷ G. Di Gregorio³⁷ A. Di Luca^{80a,80b} B. Di Micco^{79a,79b} R. Di Nardo^{79a,79b}
 K. F. Di Petrillo⁴¹ M. Diamantopoulou³⁵ F. A. Dias¹¹⁸ T. Dias Do Vale¹⁴⁷ M. A. Diaz^{141a,141b}
 F. G. Diaz Capriles²⁵ A. R. Didenko⁴⁰ M. Didenko¹⁶⁸ E. B. Diehl¹⁰⁹ S. Díez Cornell⁵⁰ C. Díez Pardos¹⁴⁶
 C. Dimitriadi¹⁶⁶ A. Dimitrievska²¹ J. Dingfelder²⁵ T. Dingley¹³⁰ I-M. Dinu^{28b} S. J. Dittmeier^{65b} F. Dittus³⁷
 M. Divisek¹³⁷ B. Dixit⁹⁵ F. Djama¹⁰⁵ T. Djobava^{154b} C. Doglioni^{104,101} A. Dohnalova^{29a} J. Dolejsi¹³⁷
 Z. Dolezal¹³⁷ K. Domijan^{88a} K. M. Dona⁴¹ M. Donadelli^{85d} B. Dong¹¹⁰ J. Donini⁴² A. D'Onofrio^{74a,74b}
 M. D'Onofrio⁹⁵ J. Dopke¹³⁸ A. Doria^{74a} N. Dos Santos Fernandes^{134a} P. Dougan¹⁰⁴ M. T. Dova⁹³
 A. T. Doyle⁶¹ M. A. Draguet¹³⁰ M. P. Drescher⁵⁷ E. Dreyer¹⁷⁴ I. Drivas-koulouris¹⁰ M. Drnevich¹²¹
 M. Drozdova⁵⁸ D. Du^{64a} T. A. du Pree¹¹⁸ F. Dubinin³⁹ M. Dubovsky^{29a} E. Duchovni¹⁷⁴ G. Duckeck¹¹²
 O. A. Ducu^{28b} D. Duda⁵⁴ A. Dudarev³⁷ E. R. Duden²⁷ M. D'uffizi¹⁰⁴ L. Duflost⁶⁸ M. Dührssen³⁷
 I. Duminica^{28g} A. E. Dumitriu^{28b} M. Dunford^{65a} S. Dungs⁵¹ K. Dunne^{49a,49b} A. Duperrin¹⁰⁵
 H. Duran Yildiz^{3a} M. Düren⁶⁰ A. Durglishvili^{154b} D. Duvnjak³⁵ B. L. Dwyer¹¹⁹ G. I. Dyckes^{18a}
 M. Dyndal^{88a} B. S. Dziedzic³⁷ Z. O. Earnshaw¹⁵¹ G. H. Eberwein¹³⁰ B. Eckerova^{29a} S. Eggebrecht⁵⁷
 E. Egidio Purcino De Souza^{85e} L. F. Ehrke⁵⁸ G. Eigen¹⁷ K. Einsweiler^{18a} T. Ekelof¹⁶⁶ P. A. Ekman¹⁰¹
 S. El Farkh^{36b} Y. El Ghazali^{64a} H. El Jarrari³⁷ A. El Moussaouy^{36a} V. Ellajosyula¹⁶⁶ M. Ellert¹⁶⁶
 F. Ellinghaus¹⁷⁶ N. Ellis³⁷ J. Elmsheuser³⁰ M. Elsayy^{120a} M. Elsing³⁷ D. Emelianov¹³⁸ Y. Enari⁸⁶
 I. Ene^{18a} S. Epari¹³ P. A. Erland⁸⁹ D. Ernani Martins Neto⁸⁹ M. Errenst¹⁷⁶ M. Escalier⁶⁸ C. Escobar¹⁶⁸
 E. Etzion¹⁵⁶ G. Evans^{134a,134b} H. Evans⁷⁰ L. S. Evans⁹⁸ A. Ezhilov³⁹ S. Ezzarqtouni^{36a} F. Fabbri^{24b,24a}
 L. Fabbri^{24b,24a} G. Facini⁹⁹ V. Fadeyev¹⁴⁰ R. M. Fakhрутdinov³⁹ D. Fakoudis¹⁰³ S. Falciano^{77a}
 L. F. Falda Ulhoa Coelho³⁷ F. Fallavollita¹¹³ G. Falsetti^{45b,45a} J. Faltova¹³⁷ C. Fan¹⁶⁷ K. Y. Fan^{66b} Y. Fan¹⁴
 Y. Fang^{14,115c} M. Fanti^{73a,73b} M. Faraj^{71a,71b} Z. Farazpay¹⁰⁰ A. Farbin⁸ A. Farilla^{79a} T. Farooque¹¹⁰
 S. M. Farrington^{138,54} F. Fassi^{36e} D. Fassouliotis⁹ M. Fauci Giannelli^{78a,78b} W. J. Fawcett³³ L. Fayard⁶⁸
 P. Federic¹³⁷ P. Federicova¹³⁵ O. L. Fedin^{39,k} M. Feickert¹⁷⁵ L. Feligioni¹⁰⁵ D. E. Fellers¹²⁷ C. Feng^{64b}
 Z. Feng¹¹⁸ M. J. Fenton¹⁶³ L. Ferencz⁵⁰ R. A. M. Ferguson⁹⁴ S. I. Fernandez Luengo^{141f}
 P. Fernandez Martinez⁶⁹ M. J. V. Fernoux¹⁰⁵ J. Ferrando⁹⁴ A. Ferrari¹⁶⁶ P. Ferrari^{118,117} R. Ferrari^{75a}
 D. Ferrere⁵⁸ C. Ferretti¹⁰⁹ D. Fiacco^{77a,77b} F. Fiedler¹⁰³ P. Fiedler¹³⁶ S. Filimonov³⁹ A. Filipčič⁹⁶
 E. K. Filmer^{160a} F. Filthaut¹¹⁷ M. C. N. Fiolhais^{134a,134c,p} L. Fiorini¹⁶⁸ W. C. Fisher¹¹⁰ T. Fitschen¹⁰⁴
 P. M. Fitzhugh¹³⁹ I. Fleck¹⁴⁶ P. Fleischmann¹⁰⁹ T. Flick¹⁷⁶ M. Flores^{34d,q} L. R. Flores Castillo^{66a}
 L. Flores Sanz De Acedo³⁷ F. M. Follega^{80a,80b} N. Fomin³³ J. H. Foo¹⁵⁹ A. Formica¹³⁹ A. C. Forti¹⁰⁴
 E. Fortin³⁷ A. W. Fortman^{18a} M. G. Foti^{18a} L. Fountas^{9,r} D. Fournier⁶⁸ H. Fox⁹⁴ P. Francavilla^{76a,76b}
 S. Francescato⁶³ S. Franchellucci⁵⁸ M. Franchini^{24b,24a} S. Franchino^{65a} D. Francis³⁷ L. Franco¹¹⁷
 V. Franco Lima³⁷ L. Franconi⁵⁰ M. Franklin⁶³ G. Frattari²⁷ Y. Y. Frid¹⁵⁶ J. Friend⁶¹ N. Fritzsche³⁷

- A. Froch⁵⁶ D. Froidevaux³⁷ J. A. Frost¹³⁰ Y. Fu^{64a} S. Fuenzalida Garrido^{141f} M. Fujimoto¹⁰⁵ K. Y. Fung^{66a}
 E. Furtado De Simas Filho^{85e} M. Furukawa¹⁵⁸ J. Fuster¹⁶⁸ A. Gaa⁵⁷ A. Gabrielli^{24b,24a} A. Gabrielli¹⁵⁹
 P. Gadow³⁷ G. Gagliardi^{59b,59a} L. G. Gagnon^{18a} S. Gaid¹⁶⁵ S. Galantzan¹⁵⁶ J. Gallagher¹ E. J. Gallas¹³⁰
 B. J. Gallop¹³⁸ K. K. Gan¹²³ S. Ganguly¹⁵⁸ Y. Gao⁵⁴ F. M. Garay Walls^{141a,141b} B. Garcia³⁰ C. García¹⁶⁸
 A. Garcia Alonso¹¹⁸ A. G. Garcia Caffaro¹⁷⁷ J. E. García Navarro¹⁶⁸ M. Garcia-Sciveres^{18a} G. L. Gardner¹³²
 R. W. Gardner⁴¹ N. Garelli¹⁶² D. Garg⁸² R. B. Garg¹⁴⁸ J. M. Gargan⁵⁴ C. A. Garner¹⁵⁹ C. M. Garvey^{34a}
 V. K. Gassmann¹⁶² G. Gaudio^{75a} V. Gautam¹³ P. Gauzzi^{77a,77b} J. Gavranovic⁹⁶ I. L. Gavrilenko³⁹
 A. Gavriluk³⁹ C. Gay¹⁶⁹ G. Gaycken¹²⁷ E. N. Gazis¹⁰ A. A. Geanta^{28b} C. M. Gee¹⁴⁰ A. Gekow¹²³
 C. Gemme^{59b} M. H. Genest⁶² A. D. Gentry¹¹⁶ S. George⁹⁸ W. F. George²¹ T. Geralis⁴⁸
 P. Gessinger-Befurt³⁷ M. E. Geyik¹⁷⁶ M. Ghani¹⁷² K. Ghorbanian⁹⁷ A. Ghosal¹⁴⁶ A. Ghosh¹⁶³ A. Ghosh⁷
 B. Giacobbe^{24b} S. Giagu^{77a,77b} T. Giani¹¹⁸ A. Giannini^{64a} S. M. Gibson⁹⁸ M. Gignac¹⁴⁰ D. T. Gil^{88b}
 A. K. Gilbert^{88a} B. J. Gilbert⁴³ D. Gillberg³⁵ G. Gilles¹¹⁸ L. Ginabat¹³¹ D. M. Gingrich^{2,e}
 M. P. Giordani^{71a,71c} P. F. Giraud¹³⁹ G. Giugliarelli^{71a,71c} D. Giugni^{73a} F. Giuli^{78a,78b} I. Gkialas^{9,r}
 L. K. Gladilin³⁹ C. Glasman¹⁰² G. R. Gledhill¹²⁷ G. Glemža⁵⁰ M. Glisic¹²⁷ I. Gnesi^{45b} Y. Go³⁰
 M. Goblirsch-Kolb³⁷ B. Gocke⁵¹ D. Godin¹¹¹ B. Gokturk^{22a} S. Goldfarb¹⁰⁸ T. Golling⁵⁸ M. G. D. Gololo^{34g}
 D. Golubkov³⁹ J. P. Gombas¹¹⁰ A. Gomes^{134a,134b} G. Gomes Da Silva¹⁴⁶ A. J. Gomez Delegido¹⁶⁸
 R. Gonçalo^{134a} L. Gonella²¹ A. Gongadze^{154c} F. Gonnella²¹ J. L. Gonski¹⁴⁸ R. Y. González Andana⁵⁴
 S. González de la Hoz¹⁶⁸ R. Gonzalez Lopez⁹⁵ C. Gonzalez Renteria^{18a} M. V. Gonzalez Rodrigues⁵⁰
 R. Gonzalez Suarez¹⁶⁶ S. Gonzalez-Sevilla⁵⁸ L. Goossens³⁷ B. Gorini³⁷ E. Gorini^{72a,72b} A. Gorišek⁹⁶
 T. C. Gosart¹³² A. T. Goshaw⁵³ M. I. Gostkin⁴⁰ S. Goswami¹²⁵ C. A. Gottardo³⁷ S. A. Gotz¹¹²
 M. Goughri^{36b} V. Goumarre⁵⁰ A. G. Goussiou¹⁴³ N. Govender^{34c} R. P. Grabarczyk¹³⁰ I. Grabowska-Bold^{88a}
 K. Graham³⁵ E. Gramstad¹²⁹ S. Grancagnolo^{72a,72b} C. M. Grant^{1,139} P. M. Gravila^{28f} F. G. Gravili^{72a,72b}
 H. M. Gray^{18a} M. Greco^{72a,72b} M. J. Green¹ C. Grefe²⁵ A. S. Grefsrud¹⁷ I. M. Gregor⁵⁰ K. T. Greif¹⁶³
 P. Grenier¹⁴⁸ S. G. Grewe¹¹³ A. A. Grillo¹⁴⁰ K. Grimm³² S. Grinstein^{13,s} J.-F. Grivaz⁶⁸ E. Gross¹⁷⁴
 J. Grosse-Knetter⁵⁷ L. Guan¹⁰⁹ J. G. R. Guerrero Rojas¹⁶⁸ G. Guerrieri³⁷ R. Gugel¹⁰³ J. A. M. Guhit¹⁰⁹
 A. Guida¹⁹ E. Guillon¹⁷² S. Guindon³⁷ F. Guo^{14,115c} J. Guo^{64c} L. Guo⁵⁰ L. Guo¹⁴ Y. Guo¹⁰⁹
 A. Gupta⁵¹ R. Gupta¹³³ S. Gurbuz²⁵ S. S. Gurdasani⁵⁶ G. Gustavino^{77a,77b} P. Gutierrez¹²⁴
 L. F. Gutierrez Zagazeta¹³² M. Gutsche⁵² C. Gutschow⁹⁹ C. Gwenlan¹³⁰ C. B. Gwilliam⁹⁵ E. S. Haaland¹²⁹
 A. Haas¹²¹ M. Habedank⁶¹ C. Haber^{18a} H. K. Hadavand⁸ A. Hadeef⁵² S. Hadzic¹¹³ A. I. Hagan⁹⁴
 J. J. Hahn¹⁴⁶ E. H. Haines⁹⁹ M. Haleem¹⁷¹ J. Haley¹²⁵ G. D. Hallowell¹⁰⁵ L. Halser²⁰ K. Hamano¹⁷⁰
 M. Hamer²⁵ E. J. Hampshire⁹⁸ J. Han^{64b} L. Han^{115a} L. Han^{64a} S. Han^{18a} Y. F. Han¹⁵⁹ K. Hanagaki⁸⁶
 M. Hance¹⁴⁰ D. A. Hangal⁴³ H. Hanif¹⁴⁷ M. D. Hank¹³² J. B. Hansen⁴⁴ P. H. Hansen⁴⁴ D. Harada⁵⁸
 T. Harenberg¹⁷⁶ S. Harkusha¹⁷⁸ M. L. Harris¹⁰⁶ Y. T. Harris²⁵ J. Harrison¹³ N. M. Harrison¹²³
 P. F. Harrison¹⁷² N. M. Hartman¹¹³ N. M. Hartmann¹¹² R. Z. Hasan^{98,138} Y. Hasegawa¹⁴⁵ F. Haslbeck¹³⁰
 S. Hassan¹⁷ R. Hauser¹¹⁰ C. M. Hawkes²¹ R. J. Hawkings³⁷ Y. Hayashi¹⁵⁸ D. Hayden¹¹⁰ C. Hayes¹⁰⁹
 R. L. Hayes¹¹⁸ C. P. Hays¹³⁰ J. M. Hays⁹⁷ H. S. Hayward⁹⁵ F. He^{64a} M. He^{14,115c} Y. He⁵⁰ Y. He⁹⁹
 N. B. Heatley⁹⁷ V. Hedberg¹⁰¹ A. L. Heggelund¹²⁹ N. D. Hehir^{97,a} C. Heidegger⁵⁶ K. K. Heidegger⁵⁶
 J. Heilman³⁵ S. Heim⁵⁰ T. Heim^{18a} J. G. Heinlein¹³² J. J. Heinrich¹²⁷ L. Heinrich^{113,t} J. Hejbal¹³⁵
 A. Held¹⁷⁵ S. Hellesund¹⁷ C. M. Helling¹⁶⁹ S. Hellman^{49a,49b} R. C. W. Henderson⁹⁴ L. Henkelmann³³
 A. M. Henriques Correia³⁷ H. Herde¹⁰¹ Y. Hernández Jiménez¹⁵⁰ L. M. Herrmann²⁵ T. Herrmann⁵² G. Herten⁵⁶
 R. Hertenberger¹¹² L. Hervas³⁷ M. E. Hespington¹⁰³ N. P. Hessey^{160a} J. Hessler¹¹³ M. Hidaoui^{36b} N. Hidic¹³⁷
 E. Hill¹⁵⁹ S. J. Hillier²¹ J. R. Hinds¹¹⁰ F. Hinterkeuser²⁵ M. Hirose¹²⁸ S. Hirose¹⁶¹ D. Hirschbuehl¹⁷⁶
 T. G. Hitchings¹⁰⁴ B. Hiti⁹⁶ J. Hobbs¹⁵⁰ R. Hobincu^{28e} N. Hod¹⁷⁴ M. C. Hodgkinson¹⁴⁴ B. H. Hodgkinson¹³⁰
 A. Hoecker³⁷ D. D. Hofer¹⁰⁹ J. Hofer¹⁶⁸ T. Holm²⁵ M. Holzbock³⁷ L. B. A. H. Hommels³³ B. P. Honan¹⁰⁴
 J. J. Hong⁷⁰ J. Hong^{64c} T. M. Hong¹³³ B. H. Hooberman¹⁶⁷ W. H. Hopkins⁶ M. C. Hoppesch¹⁶⁷ Y. Horii¹¹⁴
 M. E. Horstmann¹¹³ S. Hou¹⁵³ M. R. Housenga¹⁶⁷ A. S. Howard⁹⁶ J. Howarth⁶¹ J. Hoya⁶ M. Hrabovsky¹²⁶
 A. Hrynevich⁵⁰ T. Hryn'ova⁴ P. J. Hsu⁶⁷ S.-C. Hsu¹⁴³ T. Hsu⁶⁸ M. Hu^{18a} Q. Hu^{64a} S. Huang³³
 X. Huang^{14,115c} Y. Huang¹⁴⁴ Y. Huang¹⁰³ Y. Huang¹⁴ Z. Huang¹⁰⁴ Z. Hubacek¹³⁶ M. Huebner²⁵
 F. Hugging²⁵ T. B. Huffman¹³⁰ M. Hufnagel Maranha De Faria^{85a} C. A. Hugli⁵⁰ M. Huhtinen³⁷

S. K. Huiberts¹⁷ R. Hulsken¹⁰⁷ N. Huseynov^{12,u} J. Huston¹¹⁰ J. Huth⁶³ R. Hyneman¹⁴⁸ G. Iacobucci⁵⁸
 G. Iakovidis³⁰ L. Iconomidou-Fayard⁶⁸ J. P. Iddon³⁷ P. Iengo^{74a,74b} R. Iguchi¹⁵⁸ Y. Iiyama¹⁵⁸ T. Iizawa¹³⁰
 Y. Ikegami⁸⁶ N. Ilic¹⁵⁹ H. Imam^{85c} G. Inacio Goncalves^{85d} T. Ingebretsen Carlson^{49a,49b} J. M. Inglis⁹⁷
 G. Introzzi^{75a,75b} M. Iodice^{79a} V. Ippolito^{77a,77b} R. K. Irwin⁹⁵ M. Ishino¹⁵⁸ W. Islam¹⁷⁵ C. Issever¹⁹
 S. Istin^{22a,v} H. Ito¹⁷³ R. Iuppa^{80a,80b} A. Ivina¹⁷⁴ J. M. Izen⁴⁷ V. Izzo^{74a} P. Jacka¹³⁵ P. Jackson¹
 C. S. Jagfeld¹¹² G. Jain^{160a} P. Jain⁵⁰ K. Jakobs⁵⁶ T. Jakoubek¹⁷⁴ J. Jamieson⁶¹ W. Jang¹⁵⁸ M. Javurkova¹⁰⁶
 P. Jawahar¹⁰⁴ L. Jeanty¹²⁷ J. Jejelava^{154a} P. Jenni^{56,w} C. E. Jessiman³⁵ C. Jia^{64b} H. Jia¹⁶⁹ J. Jia¹⁵⁰
 X. Jia^{14,115c} Z. Jia^{115a} C. Jiang⁵⁴ S. Jiggins⁵⁰ J. Jimenez Pena¹³ S. Jin^{115a} A. Jinaru^{28b} O. Jinnouchi¹⁴²
 P. Johansson¹⁴⁴ K. A. Johns⁷ J. W. Johnson¹⁴⁰ F. A. Jolly⁵⁰ D. M. Jones¹⁵¹ E. Jones⁵⁰ K. S. Jones⁸
 P. Jones³³ R. W. L. Jones⁹⁴ T. J. Jones⁹⁵ H. L. Joos^{57,37} R. Joshi¹²³ J. Jovicevic¹⁶ X. Ju^{18a}
 J. J. Junggeburth³⁷ T. Junkermann^{65a} A. Juste Rozas^{13,s} M. K. Juzek⁸⁹ S. Kabana^{141e} A. Kaczmarek⁸⁹
 M. Kado¹¹³ H. Kagan¹²³ M. Kagan¹⁴⁸ A. Kahn¹³² C. Kahra¹⁰³ T. Kaji¹⁵⁸ E. Kajomovitz¹⁵⁵ N. Kakati¹⁷⁴
 I. Kalaitzidou⁵⁶ C. W. Kalderon³⁰ N. J. Kang¹⁴⁰ D. Kar^{34g} K. Karava¹³⁰ M. J. Kareem^{160b} E. Karentzos²⁵
 O. Karkout¹¹⁸ S. N. Karpov⁴⁰ Z. M. Karpova⁴⁰ V. Kartvelishvili⁹⁴ A. N. Karyukhin³⁹ E. Kasimi¹⁵⁷
 J. Katzy⁵⁰ S. Kaur³⁵ K. Kawade¹⁴⁵ M. P. Kawale¹²⁴ C. Kawamoto⁹⁰ T. Kawamoto^{64a} E. F. Kay³⁷
 F. I. Kaya¹⁶² S. Kazakos¹¹⁰ V. F. Kazanin³⁹ Y. Ke¹⁵⁰ J. M. Keaveney^{34a} R. Keeler¹⁷⁰ G. V. Kehris⁶³
 J. S. Keller³⁵ J. J. Kempster¹⁵¹ O. Kepka¹³⁵ B. P. Kerridge¹³⁸ S. Kersten¹⁷⁶ B. P. Kerševan⁹⁶
 L. Keszeghova^{29a} S. Ketabchi Haghighat¹⁵⁹ R. A. Khan¹³³ A. Khanov¹²⁵ A. G. Kharlamov³⁹ T. Kharlamova³⁹
 E. E. Khoda¹⁴³ M. Kholodenko^{134a} T. J. Khoo¹⁹ G. Khorauli¹⁷¹ J. Khubua^{154b,a} Y. A. R. Khwaira¹³¹
 B. Kibirige^{34g} D. Kim⁶ D. W. Kim^{49a,49b} Y. K. Kim⁴¹ N. Kimura⁹⁹ M. K. Kingston⁵⁷ A. Kirchhoff⁵⁷
 C. Kirfel²⁵ F. Kirfel²⁵ J. Kirk¹³⁸ A. E. Kiryunin¹¹³ S. Kita¹⁶¹ C. Kitsaki¹⁰ O. Kivernyk²⁵ M. Klassen¹⁶²
 C. Klein³⁵ L. Klein¹⁷¹ M. H. Klein⁴⁶ S. B. Klein⁵⁸ U. Klein⁹⁵ A. Klimentov³⁰ T. Klioutchnikova³⁷
 P. Kluit¹¹⁸ S. Kluth¹¹³ E. Kneringer⁸¹ T. M. Knight¹⁵⁹ A. Knue⁵¹ D. Kobylanski¹⁷⁴ S. F. Koch¹³⁰
 M. Kocian¹⁴⁸ P. Kodyš¹³⁷ D. M. Koeck¹²⁷ P. T. Koenig²⁵ T. Koffas³⁵ O. Kolay⁵² I. Koletsou⁴
 T. Komarek⁸⁹ K. Köneke⁵⁶ A. X. Y. Kong¹ T. Kono¹²² N. Konstantinidis⁹⁹ P. Kontaxakis⁵⁸ B. Konya¹⁰¹
 R. Kopeliansky⁴³ S. Koperny^{88a} K. Korcyl⁸⁹ K. Kordas^{157,x} A. Korn⁹⁹ S. Korn⁵⁷ I. Korolkov¹³
 N. Korotkova³⁹ B. Kortman¹¹⁸ O. Kortner¹¹³ S. Kortner¹¹³ W. H. Kostecka¹¹⁹ V. V. Kostyukhin¹⁴⁶
 A. Kotsokechagia³⁷ A. Kotwal⁵³ A. Koulouris³⁷ A. Kourkoumeli-Charalampidi^{75a,75b} C. Kourkoumelis⁹
 E. Kourlitis¹¹³ O. Kovanda¹²⁷ R. Kowalewski¹⁷⁰ W. Kozanecki¹²⁷ A. S. Kozhin³⁹ V. A. Kramarenko³⁹
 G. Kramerberger⁹⁶ P. Kramer²⁵ M. W. Krasny¹³¹ A. Krasznahorkay³⁷ A. C. Kraus¹¹⁹ J. W. Kraus¹⁷⁶
 J. A. Kremer⁵⁰ T. Kresse⁵² L. Kretschmann¹⁷⁶ J. Kretschmar⁹⁵ K. Kreul¹⁹ P. Krieger¹⁵⁹ M. Krivos¹³⁷
 K. Krizka²¹ K. Kroeninger⁵¹ H. Kroha¹¹³ J. Kroll¹³⁵ J. Kroll¹³² K. S. Krowpman¹¹⁰ U. Kruchonak⁴⁰
 H. Krüger²⁵ N. Krumnack⁸³ M. C. Kruse⁵³ O. Kuchinskaia³⁹ S. Kuday^{3a} S. Kuehn³⁷ R. Kuesters⁵⁶
 T. Kuhl⁵⁰ V. Kukhtin⁴⁰ Y. Kulchitsky⁴⁰ S. Kuleshov^{141d,141b} M. Kumar^{34g} N. Kumari⁵⁰ P. Kumari^{160b}
 A. Kupco¹³⁵ T. Kupfer⁵¹ A. Kupich³⁹ O. Kuprash⁵⁶ H. Kurashige⁸⁷ L. L. Kurchaninov^{160a} O. Kurdysh⁶⁸
 Y. A. Kurochkin³⁸ A. Kurova³⁹ M. Kuze¹⁴² A. K. Kvam¹⁰⁶ J. Kvita¹²⁶ T. Kwan¹⁰⁷ N. G. Kyriacou¹⁰⁹
 L. A. O. Laatu¹⁰⁵ C. Lacasta¹⁶⁸ F. Lacava^{77a,77b} H. Lacker¹⁹ D. Lacour¹³¹ N. N. Lad⁹⁹ E. Ladygin⁴⁰
 A. Lafarge⁴² B. Laforge¹³¹ T. Lagouri¹⁷⁷ F. Z. Lahbabi^{36a} S. Lai⁵⁷ J. E. Lambert¹⁷⁰ S. Lammers⁷⁰
 W. Lampl⁷ C. Lampoudis^{157,x} G. Lamprinoudis¹⁰³ A. N. Lancaster¹¹⁹ E. Lançon³⁰ U. Landgraf⁵⁶
 M. P. J. Landon⁹⁷ V. S. Lang⁵⁶ O. K. B. Langrekken¹²⁹ A. J. Lankford¹⁶³ F. Lanni³⁷ K. Lantzsche²⁵
 A. Lanza^{75a} M. Lanzac Berrocal¹⁶⁸ J. F. Laporte¹³⁹ T. Lari^{73a} F. Lasagni Manghi^{24b} M. Lassnig³⁷
 V. Latonova¹³⁵ A. Laurier¹⁵⁵ S. D. Lawlor¹⁴⁴ Z. Lawrence¹⁰⁴ R. Lazaridou¹⁷² M. Lazzaroni^{73a,73b} B. Le¹⁰⁴
 H. D. M. Le¹¹⁰ E. M. Le Boulicaut¹⁷⁷ L. T. Le Pottier^{18a} B. Leban^{24b,24a} A. Lebedev⁸³ M. LeBlanc¹⁰⁴
 F. Ledroit-Guillon⁶² S. C. Lee¹⁵³ S. Lee^{49a,49b} T. F. Lee⁹⁵ L. L. Leeuw^{34c} H. P. Lefebvre⁹⁸ M. Lefebvre¹⁷⁰
 C. Leggett^{18a} G. Lehmann Miotto³⁷ M. Leigh⁵⁸ W. A. Leight¹⁰⁶ W. Leinonen¹¹⁷ A. Leisos^{157,y}
 M. A. L. Leite^{85c} C. E. Leitgeb¹⁹ R. Leitner¹³⁷ K. J. C. Leney⁴⁶ T. Lenz²⁵ S. Leone^{76a} C. Leonidopoulos⁵⁴
 A. Leopold¹⁴⁹ R. Les¹¹⁰ C. G. Lester³³ M. Levchenko³⁹ J. Levêque⁴ L. J. Levinson¹⁷⁴ G. Levrini^{24b,24a}
 M. P. Lewicki⁸⁹ C. Lewis¹⁴³ D. J. Lewis⁴ L. Lewitt¹⁴⁴ A. Li³⁰ B. Li^{64b} C. Li^{64a} C-Q. Li¹¹³ H. Li^{64a}
 H. Li^{64b} H. Li^{115a} H. Li¹⁵ H. Li^{64b} J. Li^{64c} K. Li¹⁴ L. Li^{64c} M. Li^{14,115c} S. Li^{14,115c} S. Li^{64d,64c,z} T. Li⁵

X. Li¹⁰⁷ Z. Li¹⁵⁸ Z. Li^{14,115c} Z. Li^{64a} S. Liang^{14,115c} Z. Liang¹⁴ M. Liberatore¹³⁹ B. Liberti^{78a} K. Lie^{66c}
 J. Lieber Marin^{85e} H. Lien⁷⁰ H. Lin¹⁰⁹ K. Lin¹¹⁰ L. Linden¹¹² R. E. Lindley⁷ J. H. Lindon² J. Ling⁶³
 E. Lipeles¹³² A. Lipniacka¹⁷ A. Lister¹⁶⁹ J. D. Little⁷⁰ B. Liu¹⁴ B. X. Liu^{115b} D. Liu^{64d,64c} E. H. L. Liu²¹
 J. B. Liu^{64a} J. K. K. Liu³³ K. Liu^{64d} K. Liu^{64d,64c} M. Liu^{64a} M. Y. Liu^{64a} P. Liu¹⁴ Q. Liu^{64d,143,64c}
 X. Liu^{64a} X. Liu^{64b} Y. Liu^{115b,115c} Y. L. Liu^{64b} Y. W. Liu^{64a} S. L. Lloyd⁹⁷ E. M. Lobodzinska⁵⁰ P. Loch⁷
 E. Lodhi¹⁵⁹ T. Lohse¹⁹ K. Lohwasser¹⁴⁴ E. Loiacono⁵⁰ J. D. Lomas²¹ J. D. Long⁴³ I. Longarini¹⁶³
 R. Longo¹⁶⁷ I. Lopez Paz⁶⁹ A. Lopez Solis⁵⁰ N. A. Lopez-canelas⁷ N. Lorenzo Martinez⁴ A. M. Lory¹¹²
 M. Losada^{120a} G. Lösckce Centeno¹⁵¹ O. Loseva³⁹ X. Lou^{49a,49b} X. Lou^{14,115c} A. Lounis⁶⁸ P. A. Love⁹⁴
 G. Lu^{14,115c} M. Lu⁶⁸ S. Lu¹³² Y. J. Lu⁶⁷ H. J. Lubatti¹⁴³ C. Luci^{77a,77b} F. L. Lucio Alves^{115a} F. Luehring⁷⁰
 O. Lukianchuk⁶⁸ B. S. Lunday¹³² O. Lundberg¹⁴⁹ B. Lund-Jensen^{149,a} N. A. Luongo⁶ M. S. Lutz³⁷
 A. B. Lux²⁶ D. Lynn³⁰ R. Lysak¹³⁵ E. Lytken¹⁰¹ V. Lyubushkin⁴⁰ T. Lyubushkina⁴⁰ M. M. Lyukova¹⁵⁰
 M. Firdaus M. Soberi⁵⁴ H. Ma³⁰ K. Ma^{64a} L. L. Ma^{64b} W. Ma^{64a} Y. Ma¹²⁵ J. C. MacDonald¹⁰³
 P. C. Machado De Abreu Farias^{85e} R. Madar⁴² T. Madula⁹⁹ J. Maeda⁸⁷ T. Maeno³⁰ H. Maguire¹⁴⁴
 V. Maiboroda¹³⁹ A. Maio^{134a,134b,134d} K. Maj^{88a} O. Majersky⁵⁰ S. Majewski¹²⁷ N. Makovec⁶⁸
 V. Maksimovic¹⁶ B. Malaescu¹³¹ Pa. Malecki⁸⁹ V. P. Maleev³⁹ F. Malek^{62,aa} M. Mali⁹⁶ D. Malito⁹⁸
 U. Mallik^{82,a} S. Maltezos¹⁰ S. Malyukov⁴⁰ J. Mamuzic¹³ G. Mancini⁵⁵ M. N. Mancini²⁷ G. Manco^{75a,75b}
 J. P. Mandalia⁹⁷ S. S. Mandary¹⁵¹ I. Mandić⁹⁶ L. Manhaes de Andrade Filho^{85a} I. M. Maniatis¹⁷⁴
 J. Manjarres Ramos⁹² D. C. Mankad¹⁷⁴ A. Mann¹¹² S. Manzoni³⁷ L. Mao^{64c} X. Mapekula^{34c}
 A. Marantis^{157,y} G. Marchiori⁵ M. Marcisovsky¹³⁵ C. Marcon^{73a} M. Marinescu²¹ S. Marium⁵⁰
 M. Marjanovic¹²⁴ A. Markhoos⁵⁶ M. Markovitch⁶⁸ M. K. Maroun¹⁰⁶ E. J. Marshall⁹⁴ Z. Marshall^{18a}
 S. Marti-Garcia¹⁶⁸ J. Martin⁹⁹ T. A. Martin¹³⁸ V. J. Martin⁵⁴ B. Martin dit Latour¹⁷ L. Martinelli^{77a,77b}
 M. Martinez^{13,s} P. Martinez Agullo¹⁶⁸ V. I. Martinez Outschoorn¹⁰⁶ P. Martinez Suarez¹³ S. Martin-Haugh¹³⁸
 G. Martinovicova¹³⁷ V. S. Martoiu^{28b} A. C. Martyniuk⁹⁹ A. Marzin³⁷ D. Mascione^{80a,80b} L. Masetti¹⁰³
 J. Masik¹⁰⁴ A. L. Maslennikov³⁹ S. L. Mason⁴³ P. Massarotti^{74a,74b} P. Mastrandrea^{76a,76b}
 A. Mastroberardino^{45b,45a} T. Masubuchi¹²⁸ T. T. Mathew¹²⁷ T. Mathisen¹⁶⁶ J. Matousek¹³⁷ D. M. Mattern⁵¹
 J. Maurer^{28b} T. Maurin⁶¹ A. J. Maury⁶⁸ B. Maček⁹⁶ D. A. Maximov³⁹ A. E. May¹⁰⁴ R. Mazini^{34g}
 I. Maznas¹¹⁹ M. Mazza¹¹⁰ S. M. Mazza¹⁴⁰ E. Mazzeo^{73a,73b} C. Mc Ginn³⁰ J. P. Mc Gowan¹⁷⁰
 S. P. Mc Kee¹⁰⁹ C. A. Mc Lean⁶ C. C. McCracken¹⁶⁹ E. F. McDonald¹⁰⁸ A. E. McDougall¹¹⁸
 J. A. Mcfayden¹⁵¹ R. P. McGovern¹³² R. P. McKenzie^{34g} T. C. Mclachlan⁵⁰ D. J. McLaughlin⁹⁹
 S. J. McMahon¹³⁸ C. M. Mcpartland⁹⁵ R. A. McPherson^{170,o} S. Mehlhase¹¹² A. Mehta⁹⁵ D. Melini¹⁶⁸
 B. R. Mellado Garcia^{34g} A. H. Melo⁵⁷ F. Meloni⁵⁰ A. M. Mendes Jacques Da Costa¹⁰⁴ H. Y. Meng¹⁵⁹
 L. Meng⁹⁴ S. Menke¹¹³ M. Mentink³⁷ E. Meoni^{45b,45a} G. Mercado¹¹⁹ S. Merianos¹⁵⁷ C. Merlassino^{71a,71c}
 L. Merola^{74a,74b} C. Meroni^{73a,73b} J. Metcalfe⁶ A. S. Mete⁶ E. Meuser¹⁰³ C. Meyer⁷⁰ J-P. Meyer¹³⁹
 R. P. Middleton¹³⁸ L. Mijović⁵⁴ G. Mikenberg¹⁷⁴ M. Mikestikova¹³⁵ M. Mikuž⁹⁶ H. Mildner¹⁰³ A. Milic³⁷
 D. W. Miller⁴¹ E. H. Miller¹⁴⁸ L. S. Miller³⁵ A. Milov¹⁷⁴ D. A. Milstead^{49a,49b} T. Min^{115a} A. A. Minaenko³⁹
 I. A. Minashvili^{154b} L. Mince⁶¹ A. I. Mincer¹²¹ B. Mindur^{88a} M. Mineev⁴⁰ Y. Mino⁹⁰ L. M. Mir¹³
 M. Miralles Lopez⁶¹ M. Mironova^{18a} M. C. Missio¹¹⁷ A. Mitra¹⁷² V. A. Mitsou¹⁶⁸ Y. Mitsumori¹¹⁴
 O. Miu¹⁵⁹ P. S. Miyagawa⁹⁷ T. Mkrtychyan^{65a} M. Mlinarevic⁹⁹ T. Mlinarevic⁹⁹ M. Mlynarikova³⁷
 S. Mobius²⁰ P. Mogg¹¹² M. H. Mohamed Farook¹¹⁶ A. F. Mohammed^{14,115c} S. Mohapatra⁴³
 G. Mokgatitswane^{34g} L. Moleri¹⁷⁴ B. Mondal¹⁴⁶ S. Mondal¹³⁶ K. Mönig⁵⁰ E. Monnier¹⁰⁵
 L. Monsonis Romero¹⁶⁸ J. Montejo Berlingen¹³ A. Montella^{49a,49b} M. Montella¹²³ F. Montekali^{79a,79b}
 F. Monticelli⁹³ S. Monzani^{71a,71c} A. Morancho Tarda⁴⁴ N. Morange⁶⁸ A. L. Moreira De Carvalho⁵⁰
 M. Moreno Llácer¹⁶⁸ C. Moreno Martinez⁵⁸ J. M. Moreno Perez^{23b} P. Morettini^{59b} S. Morgenstern³⁷ M. Morii⁶³
 M. Morinaga¹⁵⁸ M. Moritsu⁹¹ F. Morodei^{77a,77b} P. Moschovakos³⁷ B. Moser¹³⁰ M. Mosidze^{154b}
 T. Moskalets⁴⁶ P. Moskvitina¹¹⁷ J. Moss^{32,bb} P. Moszkowicz^{88a} A. Moussa^{36d} Y. Moyal¹⁷⁴ E. J. W. Moyses¹⁰⁶
 O. Mtintsilana^{34g} S. Muanza¹⁰⁵ J. Mueller¹³³ D. Muenstermann⁹⁴ R. Müller³⁷ G. A. Mullier¹⁶⁶ A. J. Mullin³³
 J. J. Mullin¹³² A. E. Mulski⁶³ D. P. Mungo¹⁵⁹ D. Munoz Perez¹⁶⁸ F. J. Munoz Sanchez¹⁰⁴ M. Murin¹⁰⁴
 W. J. Murray^{172,138} M. Muškinja⁹⁶ C. Mwewa³⁰ A. G. Myagkov^{39,k} A. J. Myers⁸ G. Myers¹⁰⁹ M. Myska¹³⁶
 B. P. Nachman^{18a} O. Nackenhorst⁵¹ K. Nagai¹³⁰ K. Nagano⁸⁶ R. Nagasaka¹⁵⁸ J. L. Nagle^{30,cc} E. Nagy¹⁰⁵

A. M. Nairz³⁷, Y. Nakahama⁸⁶, K. Nakamura⁸⁶, K. Nakkalil⁵, H. Nanjo¹²⁸, E. A. Narayanan⁴⁶, I. Naryshkin³⁹, L. Nasella^{73a,73b}, M. Naseri³⁵, S. Nasri^{120b}, C. Nass²⁵, G. Navarro^{23a}, J. Navarro-Gonzalez¹⁶⁸, R. Nayak¹⁵⁶, A. Nayaz¹⁹, P. Y. Nechaeva³⁹, S. Nechaeva^{24b,24a}, F. Nechansky¹³⁵, L. Nedic¹³⁰, T. J. Neep²¹, A. Negri^{75a,75b}, M. Negri^{24b}, C. Nellist¹¹⁸, C. Nelson¹⁰⁷, K. Nelson¹⁰⁹, S. Nemecek¹³⁵, M. Nessi^{37,dd}, M. S. Neubauer¹⁶⁷, F. Neuhaus¹⁰³, J. Neundorff⁵⁰, J. Newell⁹⁵, P. R. Newman²¹, C. W. Ng¹³³, Y. W. Y. Ng⁵⁰, B. Ngair^{120a}, H. D. N. Nguyen¹¹¹, R. B. Nickerson¹³⁰, R. Nicolaidou¹³⁹, J. Nielsen¹⁴⁰, M. Niemeyer⁵⁷, J. Niermann⁵⁷, N. Nikiforou³⁷, V. Nikolaenko^{39,k}, I. Nikolic-Audit¹³¹, K. Nikolopoulos²¹, P. Nilsson³⁰, I. Ninca⁵⁰, G. Ninio¹⁵⁶, A. Nisati^{77a}, N. Nishu², R. Nisius¹¹³, N. Nitika^{71a,71c}, J-E. Nitschke⁵², E. K. Nkadimeng^{34g}, T. Nobe¹⁵⁸, T. Nommensen¹⁵², M. B. Norfolk¹⁴⁴, B. J. Norman³⁵, M. Noury^{36a}, J. Novak⁹⁶, T. Novak⁹⁶, L. Novotny¹³⁶, R. Novotny¹¹⁶, L. Nozka¹²⁶, K. Ntekas¹⁶³, N. M. J. Nunes De Moura Junior^{85b}, J. Ocariz¹³¹, A. Ochi⁸⁷, I. Ochoa^{134a}, S. Oerdek^{50,ee}, J. T. Offermann⁴¹, A. Ogrodnik¹³⁷, A. Oh¹⁰⁴, C. C. Ohm¹⁴⁹, H. Oide⁸⁶, R. Oishi¹⁵⁸, M. L. Ojeda³⁷, Y. Okumura¹⁵⁸, L. F. Oleiro Seabra^{134a}, I. Oleksiyuk⁵⁸, S. A. Olivares Pino^{141d}, G. Oliveira Correa¹³, D. Oliveira Damazio³⁰, J. L. Oliver¹⁶³, Ö. O. Öncel⁵⁶, A. P. O'Neill²⁰, A. Onofre^{134a,134e}, P. U. E. Onyisi¹¹, M. J. Oreglia⁴¹, G. E. Orellana⁹³, D. Orestano^{79a,79b}, N. Orlando¹³, R. S. Orr¹⁵⁹, L. M. Osojnak¹³², R. Ospanov^{64a}, Y. Osumi¹¹⁴, G. Otero y Garzon³¹, H. Otono⁹¹, P. S. Ott^{65a}, G. J. Ottino^{18a}, M. Ouchrif^{36d}, F. Ould-Saada¹²⁹, T. Ovsiannikova¹⁴³, M. Owen⁶¹, R. E. Owen¹³⁸, V. E. Ozcan^{22a}, F. Ozturk⁸⁹, N. Ozturk⁸, S. Ozturk⁸⁴, H. A. Pacey¹³⁰, A. Pacheco Pages¹³, C. Padilla Aranda¹³, G. Padovano^{77a,77b}, S. Pagan Griso^{18a}, G. Palacino⁷⁰, A. Palazzo^{72a,72b}, J. Pampel²⁵, J. Pan¹⁷⁷, T. Pan^{66a}, D. K. Panchal¹¹, C. E. Pandini¹¹⁸, J. G. Panduro Vazquez¹³⁸, H. D. Pandya¹, H. Pang¹⁵, P. Pani⁵⁰, G. Panizzo^{71a,71c}, L. Panwar¹³¹, L. Paolozzi⁵⁸, S. Parajuli¹⁶⁷, A. Paramonov⁶, C. Paraskevopoulos⁵⁵, D. Paredes Hernandez^{66b}, A. Pareti^{75a,75b}, K. R. Park⁴³, T. H. Park¹⁵⁹, M. A. Parker³³, F. Parodi^{59b,59a}, E. W. Parrish¹¹⁹, V. A. Parrish⁵⁴, J. A. Parsons⁴³, U. Parzefall⁵⁶, B. Pascual Dias¹¹¹, L. Pascual Dominguez¹⁰², E. Pasqualucci^{77a}, S. Passaggio^{59b}, F. Pastore⁹⁸, P. Patel⁸⁹, U. M. Patel⁵³, J. R. Pater¹⁰⁴, T. Pauly³⁷, F. Pauwels¹³⁷, C. I. Pazos¹⁶², M. Pedersen¹²⁹, R. Pedro^{134a}, S. V. Peleganchuk³⁹, O. Penc³⁷, E. A. Pender⁵⁴, S. Peng¹⁵, G. D. Penn¹⁷⁷, K. E. Pensi¹¹², M. Penzin³⁹, B. S. Peralva^{85d}, A. P. Pereira Peixoto¹⁴³, L. Pereira Sanchez¹⁴⁸, D. V. Perepelitsa^{30,cc}, G. Perera¹⁰⁶, E. Perez Codina^{160a}, M. Perganti¹⁰, H. Pernegger³⁷, S. Perrella^{77a,77b}, O. Perrin⁴², K. Peters⁵⁰, R. F. Y. Peters¹⁰⁴, B. A. Petersen³⁷, T. C. Petersen⁴⁴, E. Petit¹⁰⁵, V. Petousis¹³⁶, C. Petridou^{157,x}, T. Petru¹³⁷, A. Petrukhin¹⁴⁶, M. Pettee^{18a}, A. Petukhov³⁹, K. Petukhova³⁷, R. Pezoa^{141f}, L. Pezzotti³⁷, G. Pezzullo¹⁷⁷, A. J. Pflieger³⁷, T. M. Pham¹⁷⁵, T. Pham¹⁰⁸, P. W. Phillips¹³⁸, G. Piacquadio¹⁵⁰, E. Pianori^{18a}, F. Piazza¹²⁷, R. Piegaia³¹, D. Pietreanu^{28b}, A. D. Pilkington¹⁰⁴, M. Pinamonti^{71a,71c}, J. L. Pinfold², B. C. Pinheiro Pereira^{134a}, J. Pinol Bel¹³, A. E. Pinto Pinoargote¹³⁹, L. Pintucci^{71a,71c}, K. M. Piper¹⁵¹, A. Pirttikoski⁵⁸, D. A. Pizzi³⁵, L. Pizzimento^{66b}, A. Pizzini¹¹⁸, M.-A. Pleier³⁰, V. Pleskot¹³⁷, E. Plotnikova⁴⁰, G. Poddar⁹⁷, R. Poettgen¹⁰¹, L. Poggioli¹³¹, I. Pokharel⁵⁷, S. Polacek¹³⁷, G. Polesello^{75a}, A. Poley^{147,160a}, A. Polini^{24b}, C. S. Pollard¹⁷², Z. B. Pollock¹²³, E. Pompa Pacchi^{77a,77b}, N. I. Pond⁹⁹, D. Ponomarenko⁷⁰, L. Pontecorvo³⁷, S. Popa^{28a}, G. A. Popeneciu^{28d}, A. Poreba³⁷, D. M. Portillo Quintero^{160a}, S. Pospisil¹³⁶, M. A. Postill¹⁴⁴, P. Postolache^{28c}, K. Potamianos¹⁷², P. A. Potepa^{88a}, I. N. Potrap⁴⁰, C. J. Potter³³, H. Potti¹⁵², J. Poveda¹⁶⁸, M. E. Pozo Astigarraga³⁷, A. Prades Ibanez^{78a,78b}, J. Pretel¹⁷⁰, D. Price¹⁰⁴, M. Primavera^{72a}, L. Primomo^{71a,71c}, M. A. Principe Martin¹⁰², R. Privara¹²⁶, T. Procter⁶¹, M. L. Proffitt¹⁴³, N. Proklova¹³², K. Prokofiev^{66c}, G. Proto¹¹³, J. Proudfoot⁶, M. Przybycien^{88a}, W. W. Przygoda^{88b}, A. Psallidas⁴⁸, J. E. Puddefoot¹⁴⁴, D. Pudzha⁵⁶, D. Pyatiizbyantseva³⁹, J. Qian¹⁰⁹, R. Qian¹¹⁰, D. Qichen¹⁰⁴, Y. Qin¹³, T. Qiu⁵⁴, A. Quadt⁵⁷, M. Queitsch-Maitland¹⁰⁴, G. Quetant⁵⁸, R. P. Quinn¹⁶⁹, G. Rabanal Bolanos⁶³, D. Rafanoharana⁵⁶, F. Raffaelli^{78a,78b}, F. Ragusa^{73a,73b}, J. L. Rainbolt⁴¹, J. A. Raine⁵⁸, S. Rajagopalan³⁰, E. Ramakoti³⁹, L. Rambelli^{59b,59a}, I. A. Ramirez-Berend³⁵, K. Ran^{50,115c}, D. S. Rankin¹³², N. P. Rapheeha^{34g}, H. Rasheed^{28b}, V. Raskina¹³¹, D. F. Rassloff^{65a}, A. Rastogi^{18a}, S. Rave¹⁰³, S. Ravera^{59b,59a}, B. Ravina⁵⁷, I. Ravinovich¹⁷⁴, M. Raymond³⁷, A. L. Read¹²⁹, N. P. Readioff¹⁴⁴, D. M. Rebuffi^{75a,75b}, G. Redlinger³⁰, A. S. Reed¹¹³, K. Reeves²⁷, J. A. Reidelsturz¹⁷⁶, D. Reikher¹²⁷, A. Rej⁵¹, C. Rembser³⁷, M. Renda^{28b}, F. Renner⁵⁰, A. G. Rennie¹⁶³, A. L. Rescia⁵⁰, S. Resconi^{73a}, M. Ressegotti^{59b,59a}, S. Rettie³⁷, J. G. Reyes Rivera¹¹⁰, E. Reynolds^{18a}, O. L. Rezanova³⁹, P. Reznicek¹³⁷, H. Riani^{36d}, N. Ribaric⁵³, E. Ricci^{80a,80b}, R. Richter¹¹³, S. Richter^{49a,49b}, E. Richter-Was^{88b}, M. Ridel¹³¹, S. Ridouani^{36d}, P. Rieck¹²¹, P. Riedler³⁷, E. M. Riefel^{49a,49b}, J. O. Rieger¹¹⁸, M. Rijssenbeek¹⁵⁰, M. Rimoldi³⁷, L. Rinaldi^{24b,24a}

P. Rincke^{57,166} T. T. Rinn³⁰ M. P. Rinnagel¹¹² G. Ripellino¹⁶⁶ I. Riu¹³ J. C. Rivera Vergara¹⁷⁰
 F. Rizatdinova¹²⁵ E. Rizvi⁹⁷ B. R. Roberts^{18a} S. S. Roberts¹⁴⁰ S. H. Robertson^{107,o} D. Robinson³³
 M. Robles Manzano¹⁰³ A. Robson⁶¹ A. Rocchi^{78a,78b} C. Roda^{76a,76b} S. Rodriguez Bosca³⁷
 Y. Rodriguez Garcia^{23a} A. Rodriguez Rodriguez⁵⁶ A. M. Rodríguez Vera¹¹⁹ S. Roe³⁷ J. T. Roemer³⁷
 A. R. Roepe-Gier¹⁴⁰ O. Røhne¹²⁹ R. A. Rojas³⁷ C. P. A. Roland¹³¹ J. Roloff³⁰ A. Romaniouk⁸¹
 E. Romano^{75a,75b} M. Romano^{24b} A. C. Romero Hernandez¹⁶⁷ N. Rompotis⁹⁵ L. Roos¹³¹ S. Rosati^{77a}
 B. J. Rosser⁴¹ E. Rossi¹³⁰ E. Rossi^{74a,74b} L. P. Rossi⁶³ L. Rossini⁵⁶ R. Rosten¹²³ M. Rotaru^{28b} B. Rottler⁵⁶
 C. Rougier⁹² D. Rousseau⁶⁸ D. Rousso⁵⁰ A. Roy¹⁶⁷ S. Roy-Garand¹⁵⁹ A. Rozanov¹⁰⁵ Z. M. A. Rozario⁶¹
 Y. Rozen¹⁵⁵ A. Rubio Jimenez¹⁶⁸ A. J. Ruby⁹⁵ V. H. Ruelas Rivera¹⁹ T. A. Ruggeri¹ A. Ruggiero¹³⁰
 A. Ruiz-Martinez¹⁶⁸ A. Rummler³⁷ Z. Rurikova⁵⁶ N. A. Rusakovich⁴⁰ H. L. Russell¹⁷⁰ G. Russo^{77a,77b}
 J. P. Rutherford⁷ S. Rutherford Colmenares³³ M. Rybar¹³⁷ E. B. Rye¹²⁹ A. Ryzhov⁴⁶ J. A. Sabater Iglesias⁵⁸
 H. F-W. Sadrozinski¹⁴⁰ F. Safai Tehrani^{77a} B. Safarzadeh Samani¹³⁸ S. Saha¹ M. Sahinsoy⁸⁴ A. Saibel¹⁶⁸
 M. Saimpert¹³⁹ M. Saito¹⁵⁸ T. Saito¹⁵⁸ A. Sala^{73a,73b} D. Salamani³⁷ A. Salnikov¹⁴⁸ J. Salt¹⁶⁸
 A. Salvador Salas¹⁵⁶ D. Salvatore^{45b,45a} F. Salvatore¹⁵¹ A. Salzburger³⁷ D. Sammel⁵⁶ E. Sampson⁹⁴
 D. Sampsonidis^{157,x} D. Sampsonidou¹²⁷ J. Sánchez¹⁶⁸ V. Sanchez Sebastian¹⁶⁸ H. Sandaker¹²⁹ C. O. Sander⁵⁰
 J. A. Sandesara¹⁰⁶ M. Sandhoff¹⁷⁶ C. Sandoval^{23b} L. Sanfilippo^{65a} D. P. C. Sankey¹³⁸ T. Sano⁹⁰
 A. Sansoni⁵⁵ L. Santi^{37,77b} C. Santoni⁴² H. Santos^{134a,134b} A. Santra¹⁷⁴ E. Sanzani^{24b,24a} K. A. Saoucha¹⁶⁵
 J. G. Saraiva^{134a,134d} J. Sardain⁷ O. Sasaki⁸⁶ K. Sato¹⁶¹ C. Sauer³⁷ E. Sauvan⁴ P. Savard^{159,e} R. Sawada¹⁵⁸
 C. Sawyer¹³⁸ L. Sawyer¹⁰⁰ C. Sbarra^{24b} A. Sbrizzi^{24b,24a} T. Scanlon⁹⁹ J. Schaarschmidt¹⁴³ U. Schäfer¹⁰³
 A. C. Schaffer^{68,46} D. Schaile¹¹² R. D. Schamberger¹⁵⁰ C. Scharf¹⁹ M. M. Schefer²⁰ V. A. Schegelsky³⁹
 D. Scheirich¹³⁷ M. Schernau^{141e} C. Scheulen⁵⁷ C. Schiavi^{59b,59a} M. Schioppa^{45b,45a} B. Schlag¹⁴⁸
 S. Schlenker³⁷ J. Schmeing¹⁷⁶ M. A. Schmidt¹⁷⁶ K. Schmieden¹⁰³ C. Schmitt¹⁰³ N. Schmitt¹⁰³ S. Schmitt⁵⁰
 L. Schoeffel¹³⁹ A. Schoening^{65b} P. G. Scholer³⁵ E. Schopf¹³⁰ M. Schott²⁵ J. Schovancova³⁷ S. Schramm⁵⁸
 T. Schroer⁵⁸ H-C. Schultz-Coulon^{65a} M. Schumacher⁵⁶ B. A. Schumm¹⁴⁰ Ph. Schune¹³⁹ A. J. Schuy¹⁴³
 H. R. Schwartz¹⁴⁰ A. Schwartzman¹⁴⁸ T. A. Schwarz¹⁰⁹ Ph. Schwemling¹³⁹ R. Schwienhorst¹¹⁰
 F. G. Sciacca²⁰ A. Sciandra³⁰ G. Sciolla²⁷ F. Scuri^{76a} C. D. Sebastiani⁹⁵ K. Sedlaczek¹¹⁹ S. C. Seidel¹¹⁶
 A. Seiden¹⁴⁰ B. D. Seidlitz⁴³ C. Seitz⁵⁰ J. M. Seixas^{85b} G. Sekhniaidze^{74a} L. Selem⁶²
 N. Semprini-Cesari^{24b,24a} D. Sengupta⁵⁸ V. Senthilkumar¹⁶⁸ L. Serin⁶⁸ M. Sessa^{78a,78b} H. Severini¹²⁴
 F. Sforza^{59b,59a} A. Sfyrla⁵⁸ Q. Sha¹⁴ E. Shabalina⁵⁷ A. H. Shah³³ R. Shaheen¹⁴⁹ J. D. Shahinian¹³²
 D. Shaked Renous¹⁷⁴ L. Y. Shan¹⁴ M. Shapiro^{18a} A. Sharma³⁷ A. S. Sharma¹⁶⁹ P. Sharma⁸² P. B. Shatalov³⁹
 K. Shaw¹⁵¹ S. M. Shaw¹⁰⁴ Q. Shen^{64c} D. J. Sheppard¹⁴⁷ P. Sherwood⁹⁹ L. Shi⁹⁹ X. Shi¹⁴ S. Shimizu⁸⁶
 C. O. Shimmin¹⁷⁷ J. D. Shinner⁹⁸ I. P. J. Shipsey^{130,a} S. Shirabe⁹¹ M. Shiyakova^{40,ff} M. J. Shochet⁴¹
 D. R. Shope¹²⁹ B. Shrestha¹²⁴ S. Shrestha^{123,gg} I. Shreyber³⁹ M. J. Shroff¹⁷⁰ P. Sicho¹³⁵ A. M. Sickles¹⁶⁷
 E. Sideras Haddad^{34g,164} A. C. Sidley¹¹⁸ A. Sidoti^{24b} F. Siegert⁵² Dj. Sijacki¹⁶ F. Sili⁹³ J. M. Silva⁵⁴
 I. Silva Ferreira^{85b} M. V. Silva Oliveira³⁰ S. B. Silverstein^{49a} S. Simion⁶⁸ R. Simoniello³⁷ E. L. Simpson¹⁰⁴
 H. Simpson¹⁵¹ L. R. Simpson¹⁰⁹ S. Simsek⁸⁴ S. Sindhu⁵⁷ P. Sinervo¹⁵⁹ S. Singh³⁰ S. Sinha⁵⁰ S. Sinha¹⁰⁴
 M. Sioli^{24b,24a} I. Siral³⁷ E. Sitnikova⁵⁰ J. Sjölin^{49a,49b} A. Skaf⁵⁷ E. Skorda²¹ P. Skubic¹²⁴ M. Slawinska⁸⁹
 V. Smakhtin¹⁷⁴ B. H. Smart¹³⁸ S. Yu. Smirnov³⁹ Y. Smirnov³⁹ L. N. Smirnova^{39,k} O. Smirnova¹⁰¹
 A. C. Smith⁴³ D. R. Smith¹⁶³ E. A. Smith⁴¹ J. L. Smith¹⁰⁴ R. Smith¹⁴⁸ H. Smitmanns¹⁰³ M. Smizanska⁹⁴
 K. Smolek¹³⁶ A. A. Snesarev³⁹ H. L. Snoek¹¹⁸ S. Snyder³⁰ R. Sobie^{170,o} A. Soffer¹⁵⁶
 C. A. Solans Sanchez³⁷ E. Yu. Soldatov³⁹ U. Soldevila¹⁶⁸ A. A. Solodkov³⁹ S. Solomon²⁷ A. Soloshenko⁴⁰
 K. Solovieva⁵⁶ O. V. Solovyanov⁴² P. Sommer⁵² A. Sonay¹³ W. Y. Song^{160b} A. Sopczak¹³⁶ A. L. Soppio⁵⁴
 F. Sopkova^{29b} J. D. Sorenson¹¹⁶ I. R. Sotarriva Alvarez¹⁴² V. Sothilingam^{65a} O. J. Soto Sandoval^{141c,141b}
 S. Sottocornola⁷⁰ R. Soualah¹⁶⁵ Z. Soumami^{36e} D. South⁵⁰ N. Soybelman¹⁷⁴ S. Spagnolo^{72a,72b}
 M. Spalla¹¹³ D. Sperlich⁵⁶ G. Spigo³⁷ B. Spisso^{74a,74b} D. P. Spiteri⁶¹ M. Spousta¹³⁷ E. J. Staats³⁵
 R. Stamen^{65a} A. Stampekis²¹ E. Stanecka⁸⁹ W. Stanek-Maslouska⁵⁰ M. V. Stange⁵² B. Stanislaus^{18a}
 M. M. Stanitzki⁵⁰ B. Stapf⁵⁰ E. A. Starchenko³⁹ G. H. Stark¹⁴⁰ J. Stark⁹² P. Staroba¹³⁵ P. Starovoitov^{65a}
 S. Stärz¹⁰⁷ R. Staszewski⁸⁹ G. Stavropoulos⁴⁸ A. Stefl³⁷ P. Steinberg³⁰ B. Stelzer^{147,160a} H. J. Stelzer¹³³
 O. Stelzer-Chilton^{160a} H. Stenzel⁶⁰ T. J. Stevenson¹⁵¹ G. A. Stewart³⁷ J. R. Stewart¹²⁵ M. C. Stockton³⁷

G. Stoicea^{28b} M. Stolarski^{134a} S. Stonjek¹¹³ A. Straessner⁵² J. Strandberg¹⁴⁹ S. Strandberg^{49a,49b}
M. Stratmann¹⁷⁶ M. Strauss¹²⁴ T. Strebler¹⁰⁵ P. Strizenc^{29b} R. Ströhmer¹⁷¹ D. M. Strom¹²⁷
R. Stroynowski⁴⁶ A. Strubig^{49a,49b} S. A. Stucci³⁰ B. Stugu¹⁷ J. Stupak¹²⁴ N. A. Styles⁵⁰ D. Su¹⁴⁸ S. Su^{64a}
W. Su^{64d} X. Su^{64a} D. Suchy^{29a} K. Sugizaki¹⁵⁸ V. V. Sulim³⁹ M. J. Sullivan⁹⁵ D. M. S. Sultan¹³⁰
L. Sultanaliev³⁹ S. Sultansoy^{3b} T. Sumida⁹⁰ S. Sun¹⁷⁵ O. Sunneborn Gudnadottir¹⁶⁶ N. Sur¹⁰⁵
M. R. Sutton¹⁵¹ H. Suzuki¹⁶¹ M. Svatos¹³⁵ M. Swiatlowski^{160a} T. Swirski¹⁷¹ I. Sykora^{29a} M. Sykora¹³⁷
T. Sykora¹³⁷ D. Ta¹⁰³ K. Tackmann^{50,ee} A. Taffard¹⁶³ R. Tafirout^{160a} J. S. Tafoya Vargas⁶⁸ Y. Takubo⁸⁶
M. Talby¹⁰⁵ A. A. Talyshev³⁹ K. C. Tam^{66b} N. M. Tamir¹⁵⁶ A. Tanaka¹⁵⁸ J. Tanaka¹⁵⁸ R. Tanaka⁶⁸
M. Tanasini¹⁵⁰ Z. Tao¹⁶⁹ S. Tapia Araya^{141f} S. Tapprogge¹⁰³ A. Tarek Abouelfadl Mohamed¹¹⁰ S. Tarem¹⁵⁵
K. Tariq¹⁴ G. Tarna^{28b} G. F. Tartarelli^{73a} M. J. Tartarin⁹² P. Tas¹³⁷ M. Tasevsky¹³⁵ E. Tassi^{45b,45a}
A. C. Tate¹⁶⁷ G. Tateno¹⁵⁸ Y. Tayalati^{36e,hh} G. N. Taylor¹⁰⁸ W. Taylor^{160b} R. Teixeira De Lima¹⁴⁸
P. Teixeira-Dias⁹⁸ J. J. Teoh¹⁵⁹ K. Terashi¹⁵⁸ J. Terron¹⁰² S. Terzo¹³ M. Testa⁵⁵ R. J. Teuscher^{159,o}
A. Thaler⁸¹ O. Theiner⁵⁸ T. Thevenaux-Pelzer¹⁰⁵ O. Thielmann¹⁷⁶ D. W. Thomas⁹⁸ J. P. Thomas²¹
E. A. Thompson^{18a} P. D. Thompson²¹ E. Thomson¹³² R. E. Thornberry⁴⁶ C. Tian^{64a} Y. Tian⁵⁸
V. Tikhomirov^{39,k} Yu. A. Tikhonov³⁹ S. Timoshenko³⁹ D. Timoshyn¹³⁷ E. X. L. Ting¹ P. Tipton¹⁷⁷
A. Tishelman-Charny³⁰ S. H. Tlou^{34g} K. Todome¹⁴² S. Todorova-Nova¹³⁷ S. Todt⁵² L. Toffolin^{71a,71c}
M. Togawa⁸⁶ J. Tojo⁹¹ S. Tokár^{29a} K. Tokushuku⁸⁶ O. Toldaiev⁷⁰ M. Tomoto^{86,114} L. Tompkins^{148,ii}
K. W. Topolnicki^{88b} E. Torrence¹²⁷ H. Torres⁹² E. Torró Pastor¹⁶⁸ M. Toscani³¹ C. Toscirri⁴¹ M. Tost¹¹
D. R. Tovey¹⁴⁴ I. S. Trandafir^{28b} T. Trefzger¹⁷¹ A. Tricoli³⁰ I. M. Trigger^{160a} S. Trincaz-Duvoid¹³¹
D. A. Trischuk²⁷ B. Trocmé⁶² A. Tropina⁴⁰ L. Truong^{34c} M. Trzebinski⁸⁹ A. Trzupek⁸⁹ F. Tsai¹⁵⁰
M. Tsai¹⁰⁹ A. Tsiamis¹⁵⁷ P. V. Tsiarehka⁴⁰ S. Tsigaridas^{160a} A. Tsirigotis^{157,y} V. Tsiskaridze¹⁵⁹
E. G. Tskhadadze^{154a} M. Tsopoulou¹⁵⁷ Y. Tsujikawa⁹⁰ I. I. Tsukerman³⁹ V. Tsulaia^{18a} S. Tsuno⁸⁶
K. Tsurii¹²² D. Tsybychev¹⁵⁰ Y. Tu^{66b} A. Tudorache^{28b} V. Tudorache^{28b} A. N. Tuna⁶³ S. Turchikhin^{59b,59a}
I. Turk Cakir^{3a} R. Turra^{73a} T. Turtuvshin^{40,jj} P. M. Tuts⁴³ S. Tzamarias^{157,x} E. Tzovara¹⁰³ F. Ukegawa¹⁶¹
P. A. Ulloa Poblete^{141c,141b} E. N. Umaka³⁰ G. Unal³⁷ A. Undrus³⁰ G. Unel¹⁶³ J. Urban^{29b} P. Urrejola^{141a}
G. Usai⁸ R. Ushioda¹⁴² M. Usman¹¹¹ F. Ustuner⁵⁴ Z. Uysal⁸⁴ V. Vacek¹³⁶ B. Vachon¹⁰⁷ T. Vafeiadis³⁷
A. Vaitkus⁹⁹ C. Valderanis¹¹² E. Valdes Santurio^{49a,49b} M. Valente^{160a} S. Valentinetti^{24b,24a} A. Valero¹⁶⁸
E. Valiente Moreno¹⁶⁸ A. Vallier⁹² J. A. Valls Ferrer¹⁶⁸ D. R. Van Arneman¹¹⁸ T. R. Van Daalen¹⁴³
A. Van Der Graaf⁵¹ P. Van Gemmeren⁶ M. Van Rijnbach³⁷ S. Van Stroud⁹⁹ I. Van Vulpen¹¹⁸ P. Vana¹³⁷
M. Vanadia^{78a,78b} U. M. Vande Voorde¹⁴⁹ W. Vandelli³⁷ E. R. Vandewall¹²⁵ D. Vannicola¹⁵⁶ L. Vannoli⁵⁵
R. Vari^{77a} E. W. Varnes⁷ C. Varni^{18b} T. Varol¹⁵³ D. Varouchas⁶⁸ L. Varriale¹⁶⁸ K. E. Varvell¹⁵²
M. E. Vasile^{28b} L. Vaslin⁸⁶ G. A. Vasquez¹⁷⁰ A. Vasyukov⁴⁰ L. M. Vaughan¹²⁵ R. Vavricka¹⁰³
T. Vazquez Schroeder³⁷ J. Veatch³² V. Vecchio¹⁰⁴ M. J. Veen¹⁰⁶ I. Veliscek³⁰ L. M. Veloce¹⁵⁹
F. Veloso^{134a,134c} S. Veneziano^{77a} A. Ventura^{72a,72b} S. Ventura Gonzalez¹³⁹ A. Verbitskyi¹¹³ M. Verducci^{76a,76b}
C. Vergis⁹⁷ M. Verissimo De Araujo^{85b} W. Verkerke¹¹⁸ J. C. Vermeulen¹¹⁸ C. Vernieri¹⁴⁸ M. Vessella¹⁰⁶
M. C. Vetterli^{147,e} A. Vgenopoulos¹⁰³ N. Viaux Maira^{141f} T. Vickey¹⁴⁴ O. E. Vickey Boeriu¹⁴⁴
G. H. A. Viehhauser¹³⁰ L. Vignani^{65b} M. Vigil¹¹³ M. Villa^{24b,24a} M. Villaplana Perez¹⁶⁸ E. M. Villhauer⁵⁴
E. Vilucchi⁵⁵ M. G. Vinciter³⁵ A. Visibile¹¹⁸ C. Vittori³⁷ I. Vivarelli^{24b,24a} E. Voevodina¹¹³ F. Vogel¹¹²
J. C. Voigt⁵² P. Vokac¹³⁶ Yu. Volkotrub^{88b} E. Von Toerne²⁵ B. Vormwald³⁷ V. Vorobel¹³⁷ K. Vorobev³⁹
M. Vos¹⁶⁸ K. Voss¹⁴⁶ M. Vozak¹¹⁸ L. Vozdecky¹²⁴ N. Vranjes¹⁶ M. Vranjes Milosavljevic¹⁶
M. Vreeswijk¹¹⁸ N. K. Vu^{64d,64c} R. Vuillermet³⁷ O. Vujanovic¹⁰³ I. Vukotic⁴¹ I. K. Vyas³⁵ S. Wada¹⁶¹
C. Wagner¹⁴⁸ J. M. Wagner^{18a} W. Wagner¹⁷⁶ S. Wahdan¹⁷⁶ H. Wahlberg⁹³ C. H. Waits¹²⁴ J. Walder¹³⁸
R. Walker¹¹² W. Walkowiak¹⁴⁶ A. Wall¹³² E. J. Wallin¹⁰¹ T. Wamorkar⁶ A. Z. Wang¹⁴⁰ C. Wang¹⁰³
C. Wang¹¹ H. Wang^{18a} J. Wang^{66c} P. Wang⁹⁹ R. Wang⁶³ R. Wang⁶ S. M. Wang¹⁵³ S. Wang^{64b}
S. Wang¹⁴ T. Wang^{64a} W. T. Wang⁸² W. Wang¹⁴ X. Wang^{115a} X. Wang¹⁶⁷ X. Wang^{64c} Y. Wang^{64d}
Y. Wang^{115a} Y. Wang^{64a} Z. Wang¹⁰⁹ Z. Wang^{64d,53,64c} Z. Wang¹⁰⁹ A. Warburton¹⁰⁷ R. J. Ward²¹
N. Warrack⁶¹ S. Waterhouse⁹⁸ A. T. Watson²¹ H. Watson⁵⁴ M. F. Watson²¹ E. Watton^{61,138} G. Watts¹⁴³
B. M. Waugh⁹⁹ J. M. Webb⁵⁶ C. Weber³⁰ H. A. Weber¹⁹ M. S. Weber²⁰ S. M. Weber^{65a} C. Wei^{64a}
Y. Wei⁵⁶ A. R. Weidberg¹³⁰ E. J. Weik¹²¹ J. Weingarten⁵¹ C. Weiser⁵⁶ C. J. Wells⁵⁰ T. Wenaus³⁰

B. Wendland⁵¹, T. Wengler³⁷, N. S. Wenke¹¹³, N. Wermes²⁵, M. Wessels^{65a}, A. M. Wharton⁹⁴, A. S. White⁶³,
 A. White⁸, M. J. White¹, D. Whiteson¹⁶³, L. Wickremasinghe¹²⁸, W. Wiedenmann¹⁷⁵, M. Wielers¹³⁸,
 C. Wiglesworth⁴⁴, D. J. Wilbern¹²⁴, H. G. Wilkens³⁷, J. J. H. Wilkinson³³, D. M. Williams⁴³, H. H. Williams¹³²,
 S. Williams³³, S. Willocq¹⁰⁶, B. J. Wilson¹⁰⁴, P. J. Windischhofer⁴¹, F. I. Winkel³¹, F. Winklmeier¹²⁷,
 B. T. Winter⁵⁶, J. K. Winter¹⁰⁴, M. Wittgen¹⁴⁸, M. Wobisch¹⁰⁰, T. Wojtkowski⁶², Z. Wolffs¹¹⁸, J. Wollrath³⁷,
 M. W. Wolter⁸⁹, H. Wolters^{134a,134c}, M. C. Wong¹⁴⁰, E. L. Woodward⁴³, S. D. Worm⁵⁰, B. K. Wosiek⁸⁹,
 K. W. Woźniak⁸⁹, S. Wozniwski⁵⁷, K. Wraight⁶¹, C. Wu²¹, M. Wu^{115b}, M. Wu¹¹⁷, S. L. Wu¹⁷⁵, X. Wu⁵⁸,
 Y. Wu^{64a}, Z. Wu⁴, J. Wuerzinger^{113,t}, T. R. Wyatt¹⁰⁴, B. M. Wynne⁵⁴, S. Xella⁴⁴, L. Xia^{115a}, M. Xia¹⁵,
 M. Xie^{64a}, S. Xin^{14,115c}, A. Xiong¹²⁷, J. Xiong^{18a}, D. Xu¹⁴, H. Xu^{64a}, L. Xu^{64a}, R. Xu¹³², T. Xu¹⁰⁹, Y. Xu¹⁴³,
 Z. Xu⁵⁴, Z. Xu^{115a}, B. Yabsley¹⁵², S. Yacoob^{34a}, Y. Yamaguchi⁸⁶, E. Yamashita¹⁵⁸, H. Yamauchi¹⁶¹,
 T. Yamazaki^{18a}, Y. Yamazaki⁸⁷, S. Yan⁶¹, Z. Yan¹⁰⁶, H. J. Yang^{64c,64d}, H. T. Yang^{64a}, S. Yang^{64a}, T. Yang^{66c},
 X. Yang³⁷, X. Yang¹⁴, Y. Yang⁴⁶, Y. Yang^{64a}, Z. Yang^{64a}, W-M. Yao^{18a}, H. Ye^{115a}, H. Ye⁵⁷, J. Ye¹⁴, S. Ye³⁰,
 X. Ye^{64a}, Y. Yeh⁹⁹, I. Yeletsikh⁴⁰, B. Yeo^{18b}, M. R. Yexley⁹⁹, T. P. Yildirim¹³⁰, P. Yin⁴³, K. Yorita¹⁷³,
 S. Younas^{28b}, C. J. S. Young³⁷, C. Young¹⁴⁸, C. Yu^{14,115c}, Y. Yu^{64a}, J. Yuan^{14,115c}, M. Yuan¹⁰⁹, R. Yuan^{64d,64c},
 L. Yue⁹⁹, M. Zaazoua^{64a}, B. Zabinski⁸⁹, E. Zaid⁵⁴, Z. K. Zak⁸⁹, T. Zakareishvili¹⁶⁸, S. Zambito⁵⁸,
 J. A. Zamora Saa^{141d,141b}, J. Zang¹⁵⁸, D. Zanzi⁵⁶, O. Zaplatilek¹³⁶, C. Zeitnitz¹⁷⁶, H. Zeng¹⁴, J. C. Zeng¹⁶⁷,
 D. T. Zenger Jr.²⁷, O. Zenin³⁹, T. Ženiš^{29a}, S. Zenz⁹⁷, S. Zerradi^{36a}, D. Zerwas⁶⁸, M. Zhai^{14,115c}, D. F. Zhang¹⁴⁴,
 J. Zhang^{64b}, J. Zhang⁶, K. Zhang^{14,115c}, L. Zhang^{64a}, L. Zhang^{115a}, P. Zhang^{14,115c}, R. Zhang¹⁷⁵, S. Zhang¹⁰⁹,
 S. Zhang⁹², T. Zhang¹⁵⁸, X. Zhang^{64c}, Y. Zhang¹⁴³, Y. Zhang⁹⁹, Y. Zhang^{115a}, Z. Zhang^{18a}, Z. Zhang^{64b},
 Z. Zhang⁶⁸, H. Zhao¹⁴³, T. Zhao^{64b}, Y. Zhao¹⁴⁰, Z. Zhao^{64a}, Z. Zhao^{64a}, A. Zhemchugov⁴⁰, J. Zheng^{115a},
 K. Zheng¹⁶⁷, X. Zheng^{64a}, Z. Zheng¹⁴⁸, D. Zhong¹⁶⁷, B. Zhou¹⁰⁹, H. Zhou⁷, N. Zhou^{64c}, Y. Zhou¹⁵,
 Y. Zhou^{115a}, Y. Zhou⁷, C. G. Zhu^{64b}, J. Zhu¹⁰⁹, X. Zhu^{64d}, Y. Zhu^{64c}, Y. Zhu^{64a}, X. Zhuang¹⁴, K. Zhukov⁷⁰,
 N. I. Zimine⁴⁰, J. Zinsser^{65b}, M. Ziolkowski¹⁴⁶, L. Živković¹⁶, A. Zoccoli^{24b,24a}, K. Zoch⁶³, T. G. Zorbas¹⁴⁴,
 O. Zormpa⁴⁸, W. Zou⁴³, and L. Zwalinski³⁷

(ATLAS Collaboration)

¹Department of Physics, University of Adelaide, Adelaide, Australia²Department of Physics, University of Alberta, Edmonton, Alberta, Canada^{3a}Department of Physics, Ankara University, Ankara, Türkiye^{3b}Division of Physics, TOBB University of Economics and Technology, Ankara, Türkiye⁴LAPP, Université Savoie Mont Blanc, CNRS/IN2P3, Annecy, France⁵APC, Université Paris Cité, CNRS/IN2P3, Paris, France⁶High Energy Physics Division, Argonne National Laboratory, Argonne, Illinois, USA⁷Department of Physics, University of Arizona, Tucson, Arizona, USA⁸Department of Physics, University of Texas at Arlington, Arlington, Texas, USA⁹Physics Department, National and Kapodistrian University of Athens, Athens, Greece¹⁰Physics Department, National Technical University of Athens, Zografou, Greece¹¹Department of Physics, University of Texas at Austin, Austin, Texas, USA¹²Institute of Physics, Azerbaijan Academy of Sciences, Baku, Azerbaijan¹³Institut de Física d'Altes Energies (IFAE), Barcelona Institute of Science and Technology, Barcelona, Spain¹⁴Institute of High Energy Physics, Chinese Academy of Sciences, Beijing, China¹⁵Physics Department, Tsinghua University, Beijing, China¹⁶Institute of Physics, University of Belgrade, Belgrade, Serbia¹⁷Department for Physics and Technology, University of Bergen, Bergen, Norway^{18a}Physics Division, Lawrence Berkeley National Laboratory, Berkeley, California, USA^{18b}University of California, Berkeley, California, USA¹⁹Institut für Physik, Humboldt Universität zu Berlin, Berlin, Germany²⁰Albert Einstein Center for Fundamental Physics and Laboratory for High Energy Physics, University of Bern, Bern, Switzerland²¹School of Physics and Astronomy, University of Birmingham, Birmingham, United Kingdom^{22a}Department of Physics, Bogazici University, Istanbul, Türkiye^{22b}Department of Physics Engineering, Gaziantep University, Gaziantep, Türkiye

- ^{22c}*Department of Physics, Istanbul University, Istanbul, Türkiye*
- ^{23a}*Facultad de Ciencias y Centro de Investigaciones, Universidad Antonio Nariño, Bogotá, Colombia*
- ^{23b}*Departamento de Física, Universidad Nacional de Colombia, Bogotá, Colombia*
- ^{24a}*Dipartimento di Fisica e Astronomia A. Righi, Università di Bologna, Bologna, Italy*
- ^{24b}*INFN Sezione di Bologna, Italy*
- ²⁵*Physikalisches Institut, Universität Bonn, Bonn, Germany*
- ²⁶*Department of Physics, Boston University, Boston, Massachusetts, USA*
- ²⁷*Department of Physics, Brandeis University, Waltham, Massachusetts, USA*
- ^{28a}*Transilvania University of Brasov, Brasov, Romania*
- ^{28b}*Horia Hulubei National Institute of Physics and Nuclear Engineering, Bucharest, Romania*
- ^{28c}*Department of Physics, Alexandru Ioan Cuza University of Iasi, Iasi, Romania*
- ^{28d}*National Institute for Research and Development of Isotopic and Molecular Technologies, Physics Department, Cluj-Napoca, Romania*
- ^{28e}*National University of Science and Technology Politehnica, Bucharest, Romania*
- ^{28f}*West University in Timisoara, Timisoara, Romania*
- ^{28g}*Faculty of Physics, University of Bucharest, Bucharest, Romania*
- ^{29a}*Faculty of Mathematics, Physics and Informatics, Comenius University, Bratislava, Slovak Republic*
- ^{29b}*Department of Subnuclear Physics, Institute of Experimental Physics of the Slovak Academy of Sciences, Kosice, Slovak Republic*
- ³⁰*Physics Department, Brookhaven National Laboratory, Upton, New York, USA*
- ³¹*Universidad de Buenos Aires, Facultad de Ciencias Exactas y Naturales, Departamento de Física, y CONICET, Instituto de Física de Buenos Aires (IFIBA), Buenos Aires, Argentina*
- ³²*California State University, California, USA*
- ³³*Cavendish Laboratory, University of Cambridge, Cambridge, United Kingdom*
- ^{34a}*Department of Physics, University of Cape Town, Cape Town, South Africa*
- ^{34b}*Themba Labs, Western Cape, South Africa*
- ^{34c}*Department of Mechanical Engineering Science, University of Johannesburg, Johannesburg, South Africa*
- ^{34d}*National Institute of Physics, University of the Philippines Diliman (Philippines), Philippines*
- ^{34e}*University of South Africa, Department of Physics, Pretoria, South Africa*
- ^{34f}*University of Zululand, KwaDlangezwa, South Africa*
- ^{34g}*School of Physics, University of the Witwatersrand, Johannesburg, South Africa*
- ³⁵*Department of Physics, Carleton University, Ottawa, Ontario, Canada*
- ^{36a}*Faculté des Sciences Ain Chock, Université Hassan II de Casablanca, Morocco*
- ^{36b}*Faculté des Sciences, Université Ibn-Tofail, Kénitra, Morocco*
- ^{36c}*Faculté des Sciences Semlalia, Université Cadi Ayyad, LPHEA-Marrakech, Morocco*
- ^{36d}*LPMR, Faculté des Sciences, Université Mohamed Premier, Oujda, Morocco*
- ^{36e}*Faculté des sciences, Université Mohammed V, Rabat, Morocco*
- ^{36f}*Institute of Applied Physics, Mohammed VI Polytechnic University, Ben Guerir, Morocco*
- ³⁷*CERN, Geneva, Switzerland*
- ³⁸*Affiliated with an institute formerly covered by a cooperation agreement with CERN*
- ³⁹*Affiliated with an institute covered by a cooperation agreement with CERN*
- ⁴⁰*Affiliated with an international laboratory covered by a cooperation agreement with CERN*
- ⁴¹*Enrico Fermi Institute, University of Chicago, Chicago, Illinois, USA*
- ⁴²*LPC, Université Clermont Auvergne, CNRS/IN2P3, Clermont-Ferrand, France*
- ⁴³*Nevis Laboratory, Columbia University, Irvington, New York, USA*
- ⁴⁴*Niels Bohr Institute, University of Copenhagen, Copenhagen, Denmark*
- ^{45a}*Dipartimento di Fisica, Università della Calabria, Rende, Italy*
- ^{45b}*INFN Gruppo Collegato di Cosenza, Laboratori Nazionali di Frascati, Italy*
- ⁴⁶*Physics Department, Southern Methodist University, Dallas, Texas, USA*
- ⁴⁷*Physics Department, University of Texas at Dallas, Richardson, Texas, USA*
- ⁴⁸*National Centre for Scientific Research “Demokritos”, Agia Paraskevi, Greece*
- ^{49a}*Department of Physics, Stockholm University, Sweden*
- ^{49b}*Oskar Klein Centre, Stockholm, Sweden*
- ⁵⁰*Deutsches Elektronen-Synchrotron DESY, Hamburg and Zeuthen, Germany*
- ⁵¹*Fakultät Physik, Technische Universität Dortmund, Dortmund, Germany*
- ⁵²*Institut für Kern- und Teilchenphysik, Technische Universität Dresden, Dresden, Germany*
- ⁵³*Department of Physics, Duke University, Durham, North Carolina, USA*
- ⁵⁴*SUPA—School of Physics and Astronomy, University of Edinburgh, Edinburgh, United Kingdom*
- ⁵⁵*INFN e Laboratori Nazionali di Frascati, Frascati, Italy*

- ⁵⁶Physikalisches Institut, Albert-Ludwigs-Universität Freiburg, Freiburg, Germany
- ⁵⁷II. Physikalisches Institut, Georg-August-Universität Göttingen, Göttingen, Germany
- ⁵⁸Département de Physique Nucléaire et Corpusculaire, Université de Genève, Genève, Switzerland
- ^{59a}Dipartimento di Fisica, Università di Genova, Genova, Italy
- ^{59b}INFN Sezione di Genova, Italy
- ⁶⁰II. Physikalisches Institut, Justus-Liebig-Universität Giessen, Giessen, Germany
- ⁶¹SUPA—School of Physics and Astronomy, University of Glasgow, Glasgow, United Kingdom
- ⁶²LPSC, Université Grenoble Alpes, CNRS/IN2P3, Grenoble INP, Grenoble, France
- ⁶³Laboratory for Particle Physics and Cosmology, Harvard University, Cambridge, Massachusetts, USA
- ^{64a}Department of Modern Physics and State Key Laboratory of Particle Detection and Electronics, University of Science and Technology of China, Hefei, China
- ^{64b}Institute of Frontier and Interdisciplinary Science and Key Laboratory of Particle Physics and Particle Irradiation (MOE), Shandong University, Qingdao, China
- ^{64c}School of Physics and Astronomy, Shanghai Jiao Tong University, Key Laboratory for Particle Astrophysics and Cosmology (MOE), SKLPPC, Shanghai, China
- ^{64d}Tsung-Dao Lee Institute, Shanghai, China
- ^{64e}School of Physics, Zhengzhou University, China
- ^{65a}Kirchhoff-Institut für Physik, Ruprecht-Karls-Universität Heidelberg, Heidelberg, Germany
- ^{65b}Physikalisches Institut, Ruprecht-Karls-Universität Heidelberg, Heidelberg, Germany
- ^{66a}Department of Physics, Chinese University of Hong Kong, Shatin, N.T., Hong Kong, China
- ^{66b}Department of Physics, University of Hong Kong, Hong Kong, China
- ^{66c}Department of Physics and Institute for Advanced Study, Hong Kong University of Science and Technology, Clear Water Bay, Kowloon, Hong Kong, China
- ⁶⁷Department of Physics, National Tsing Hua University, Hsinchu, Taiwan
- ⁶⁸IJCLab, Université Paris-Saclay, CNRS/IN2P3, 91405, Orsay, France
- ⁶⁹Centro Nacional de Microelectrónica (IMB-CNM-CSIC), Barcelona, Spain
- ⁷⁰Department of Physics, Indiana University, Bloomington, Indiana, USA
- ^{71a}INFN Gruppo Collegato di Udine, Sezione di Trieste, Udine, Italy
- ^{71b}ICTP, Trieste, Italy
- ^{71c}Dipartimento Politecnico di Ingegneria e Architettura, Università di Udine, Udine, Italy
- ^{72a}INFN Sezione di Lecce, Italy
- ^{72b}Dipartimento di Matematica e Fisica, Università del Salento, Lecce, Italy
- ^{73a}INFN Sezione di Milano, Italy
- ^{73b}Dipartimento di Fisica, Università di Milano, Milano, Italy
- ^{74a}INFN Sezione di Napoli, Italy
- ^{74b}Dipartimento di Fisica, Università di Napoli, Napoli, Italy
- ^{75a}INFN Sezione di Pavia, Italy
- ^{75b}Dipartimento di Fisica, Università di Pavia, Pavia, Italy
- ^{76a}INFN Sezione di Pisa, Italy
- ^{76b}Dipartimento di Fisica E. Fermi, Università di Pisa, Pisa, Italy
- ^{77a}INFN Sezione di Roma, Italy
- ^{77b}Dipartimento di Fisica, Sapienza Università di Roma, Roma, Italy
- ^{78a}INFN Sezione di Roma Tor Vergata, Italy
- ^{78b}Dipartimento di Fisica, Università di Roma Tor Vergata, Roma, Italy
- ^{79a}INFN Sezione di Roma Tre, Italy
- ^{79b}Dipartimento di Matematica e Fisica, Università Roma Tre, Roma, Italy
- ^{80a}INFN-TIFPA, Italy
- ^{80b}Università degli Studi di Trento, Trento, Italy
- ⁸¹Universität Innsbruck, Department of Astro and Particle Physics, Innsbruck, Austria
- ⁸²University of Iowa, Iowa City, Iowa, USA
- ⁸³Department of Physics and Astronomy, Iowa State University, Ames, Iowa, USA
- ⁸⁴Istinye University, Sariyer, Istanbul, Türkiye
- ^{85a}Departamento de Engenharia Elétrica, Universidade Federal de Juiz de Fora (UFJF), Juiz de Fora, Brazil
- ^{85b}Universidade Federal do Rio De Janeiro COPPE/EE/IF, Rio de Janeiro, Brazil
- ^{85c}Instituto de Física, Universidade de São Paulo, São Paulo, Brazil
- ^{85d}Rio de Janeiro State University, Rio de Janeiro, Brazil
- ^{85e}Federal University of Bahia, Bahia, Brazil
- ⁸⁶KEK, High Energy Accelerator Research Organization, Tsukuba, Japan

- ⁸⁷Graduate School of Science, Kobe University, Kobe, Japan
- ^{88a}AGH University of Krakow, Faculty of Physics and Applied Computer Science, Krakow, Poland
- ^{88b}Marian Smoluchowski Institute of Physics, Jagiellonian University, Krakow, Poland
- ⁸⁹Institute of Nuclear Physics Polish Academy of Sciences, Krakow, Poland
- ⁹⁰Faculty of Science, Kyoto University, Kyoto, Japan
- ⁹¹Research Center for Advanced Particle Physics and Department of Physics, Kyushu University, Fukuoka, Japan
- ⁹²L2IT, Université de Toulouse, CNRS/IN2P3, UPS, Toulouse, France
- ⁹³Instituto de Física La Plata, Universidad Nacional de La Plata and CONICET, La Plata, Argentina
- ⁹⁴Physics Department, Lancaster University, Lancaster, United Kingdom
- ⁹⁵Oliver Lodge Laboratory, University of Liverpool, Liverpool, United Kingdom
- ⁹⁶Department of Experimental Particle Physics, Jožef Stefan Institute and Department of Physics, University of Ljubljana, Ljubljana, Slovenia
- ⁹⁷School of Physics and Astronomy, Queen Mary University of London, London, United Kingdom
- ⁹⁸Department of Physics, Royal Holloway University of London, Egham, United Kingdom
- ⁹⁹Department of Physics and Astronomy, University College London, London, United Kingdom
- ¹⁰⁰Louisiana Tech University, Ruston, Louisiana, USA
- ¹⁰¹Fysiska institutionen, Lunds universitet, Lund, Sweden
- ¹⁰²Departamento de Física Teórica C-15 and CIAFF, Universidad Autónoma de Madrid, Madrid, Spain
- ¹⁰³Institut für Physik, Universität Mainz, Mainz, Germany
- ¹⁰⁴School of Physics and Astronomy, University of Manchester, Manchester, United Kingdom
- ¹⁰⁵CPPM, Aix-Marseille Université, CNRS/IN2P3, Marseille, France
- ¹⁰⁶Department of Physics, University of Massachusetts, Amherst, Massachusetts, USA
- ¹⁰⁷Department of Physics, McGill University, Montreal, Quebec, Canada
- ¹⁰⁸School of Physics, University of Melbourne, Victoria, Australia
- ¹⁰⁹Department of Physics, University of Michigan, Ann Arbor, Michigan, USA
- ¹¹⁰Department of Physics and Astronomy, Michigan State University, East Lansing, Michigan, USA
- ¹¹¹Group of Particle Physics, University of Montreal, Montreal, Quebec, Canada
- ¹¹²Fakultät für Physik, Ludwig-Maximilians-Universität München, München, Germany
- ¹¹³Max-Planck-Institut für Physik (Werner-Heisenberg-Institut), München, Germany
- ¹¹⁴Graduate School of Science and Kobayashi-Maskawa Institute, Nagoya University, Nagoya, Japan
- ^{115a}Department of Physics, Nanjing University, Nanjing, China
- ^{115b}School of Science, Shenzhen Campus of Sun Yat-sen University, China
- ^{115c}University of Chinese Academy of Science (UCAS), Beijing, China
- ¹¹⁶Department of Physics and Astronomy, University of New Mexico, Albuquerque, New Mexico, USA
- ¹¹⁷Institute for Mathematics, Astrophysics and Particle Physics, Radboud University/Nikhef, Nijmegen, Netherlands
- ¹¹⁸Nikhef National Institute for Subatomic Physics and University of Amsterdam, Amsterdam, Netherlands
- ¹¹⁹Department of Physics, Northern Illinois University, DeKalb, Illinois, USA
- ^{120a}New York University Abu Dhabi, Abu Dhabi, United Arab Emirates
- ^{120b}United Arab Emirates University, Al Ain, United Arab Emirates
- ¹²¹Department of Physics, New York University, New York, New York, USA
- ¹²²Ochanomizu University, Otsuka, Bunkyo-ku, Tokyo, Japan
- ¹²³Ohio State University, Columbus, Ohio, USA
- ¹²⁴Homer L. Dodge Department of Physics and Astronomy, University of Oklahoma, Norman, Oklahoma, USA
- ¹²⁵Department of Physics, Oklahoma State University, Stillwater, Oklahoma, USA
- ¹²⁶Palacký University, Joint Laboratory of Optics, Olomouc, Czech Republic
- ¹²⁷Institute for Fundamental Science, University of Oregon, Eugene, Oregon, USA
- ¹²⁸Graduate School of Science, Osaka University, Osaka, Japan
- ¹²⁹Department of Physics, University of Oslo, Oslo, Norway
- ¹³⁰Department of Physics, Oxford University, Oxford, United Kingdom
- ¹³¹LPNHE, Sorbonne Université, Université Paris Cité, CNRS/IN2P3, Paris, France
- ¹³²Department of Physics, University of Pennsylvania, Philadelphia, Pennsylvania, USA
- ¹³³Department of Physics and Astronomy, University of Pittsburgh, Pittsburgh, Pennsylvania, USA
- ^{134a}Laboratório de Instrumentação e Física Experimental de Partículas—LIP, Lisboa, Portugal
- ^{134b}Departamento de Física, Faculdade de Ciências, Universidade de Lisboa, Lisboa, Portugal
- ^{134c}Departamento de Física, Universidade de Coimbra, Coimbra, Portugal
- ^{134d}Centro de Física Nuclear da Universidade de Lisboa, Lisboa, Portugal
- ^{134e}Departamento de Física, Universidade do Minho, Braga, Portugal

- ^{134f} *Departamento de Física Teórica y del Cosmos, Universidad de Granada, Granada (Spain), Spain*
- ^{134g} *Departamento de Física, Instituto Superior Técnico, Universidade de Lisboa, Lisboa, Portugal*
- ¹³⁵ *Institute of Physics of the Czech Academy of Sciences, Prague, Czech Republic*
- ¹³⁶ *Czech Technical University in Prague, Prague, Czech Republic*
- ¹³⁷ *Charles University, Faculty of Mathematics and Physics, Prague, Czech Republic*
- ¹³⁸ *Particle Physics Department, Rutherford Appleton Laboratory, Didcot, United Kingdom*
- ¹³⁹ *IRFU, CEA, Université Paris-Saclay, Gif-sur-Yvette, France*
- ¹⁴⁰ *Santa Cruz Institute for Particle Physics, University of California Santa Cruz, Santa Cruz, California, USA*
- ^{141a} *Departamento de Física, Pontificia Universidad Católica de Chile, Santiago, Chile*
- ^{141b} *Millennium Institute for Subatomic physics at high energy frontier (SAPHIR), Santiago, Chile*
- ^{141c} *Instituto de Investigación Multidisciplinario en Ciencia y Tecnología, y Departamento de Física, Universidad de La Serena, Chile*
- ^{141d} *Universidad Andres Bello, Department of Physics, Santiago, Chile*
- ^{141e} *Instituto de Alta Investigación, Universidad de Tarapacá, Arica, Chile*
- ^{141f} *Departamento de Física, Universidad Técnica Federico Santa María, Valparaíso, Chile*
- ¹⁴² *Department of Physics, Institute of Science, Tokyo, Japan*
- ¹⁴³ *Department of Physics, University of Washington, Seattle, Washington, USA*
- ¹⁴⁴ *Department of Physics and Astronomy, University of Sheffield, Sheffield, United Kingdom*
- ¹⁴⁵ *Department of Physics, Shinshu University, Nagano, Japan*
- ¹⁴⁶ *Department Physik, Universität Siegen, Siegen, Germany*
- ¹⁴⁷ *Department of Physics, Simon Fraser University, Burnaby, British Columbia, Canada*
- ¹⁴⁸ *SLAC National Accelerator Laboratory, Stanford, California, USA*
- ¹⁴⁹ *Department of Physics, Royal Institute of Technology, Stockholm, Sweden*
- ¹⁵⁰ *Departments of Physics and Astronomy, Stony Brook University, Stony Brook, New York, USA*
- ¹⁵¹ *Department of Physics and Astronomy, University of Sussex, Brighton, United Kingdom*
- ¹⁵² *School of Physics, University of Sydney, Sydney, Australia*
- ¹⁵³ *Institute of Physics, Academia Sinica, Taipei, Taiwan*
- ^{154a} *E. Andronikashvili Institute of Physics, Iv. Javakishvili Tbilisi State University, Tbilisi, Georgia*
- ^{154b} *High Energy Physics Institute, Tbilisi State University, Tbilisi, Georgia*
- ^{154c} *University of Georgia, Tbilisi, Georgia*
- ¹⁵⁵ *Department of Physics, Technion, Israel Institute of Technology, Haifa, Israel*
- ¹⁵⁶ *Raymond and Beverly Sackler School of Physics and Astronomy, Tel Aviv University, Tel Aviv, Israel*
- ¹⁵⁷ *Department of Physics, Aristotle University of Thessaloniki, Thessaloniki, Greece*
- ¹⁵⁸ *International Center for Elementary Particle Physics and Department of Physics, University of Tokyo, Tokyo, Japan*
- ¹⁵⁹ *Department of Physics, University of Toronto, Toronto, Ontario, Canada*
- ^{160a} *TRIUMF, Vancouver, British Columbia, Canada*
- ^{160b} *Department of Physics and Astronomy, York University, Toronto, Ontario, Canada*
- ¹⁶¹ *Division of Physics and Tomonaga Center for the History of the Universe, Faculty of Pure and Applied Sciences, University of Tsukuba, Tsukuba, Japan*
- ¹⁶² *Department of Physics and Astronomy, Tufts University, Medford, Massachusetts, USA*
- ¹⁶³ *Department of Physics and Astronomy, University of California Irvine, Irvine, California, USA*
- ¹⁶⁴ *University of West Attica, Athens, Greece*
- ¹⁶⁵ *University of Sharjah, Sharjah, United Arab Emirates*
- ¹⁶⁶ *Department of Physics and Astronomy, University of Uppsala, Uppsala, Sweden*
- ¹⁶⁷ *Department of Physics, University of Illinois, Urbana, Illinois, USA*
- ¹⁶⁸ *Instituto de Física Corpuscular (IFIC), Centro Mixto Universidad de Valencia—CSIC, Valencia, Spain*
- ¹⁶⁹ *Department of Physics, University of British Columbia, Vancouver British Columbia, Canada*
- ¹⁷⁰ *Department of Physics and Astronomy, University of Victoria, Victoria British Columbia, Canada*
- ¹⁷¹ *Fakultät für Physik und Astronomie, Julius-Maximilians-Universität Würzburg, Würzburg, Germany*
- ¹⁷² *Department of Physics, University of Warwick, Coventry, United Kingdom*
- ¹⁷³ *Waseda University, Tokyo, Japan*
- ¹⁷⁴ *Department of Particle Physics and Astrophysics, Weizmann Institute of Science, Rehovot, Israel*
- ¹⁷⁵ *Department of Physics, University of Wisconsin, Madison, Wisconsin, USA*
- ¹⁷⁶ *Fakultät für Mathematik und Naturwissenschaften, Fachgruppe Physik, Bergische Universität Wuppertal, Wuppertal, Germany*
- ¹⁷⁷ *Department of Physics, Yale University, New Haven, Connecticut, USA*
- ¹⁷⁸ *Yerevan Physics Institute, Yerevan, Armenia*

^aDeceased.

^bAlso at Department of Physics, King's College London, London, United Kingdom.

^cAlso at Institute of Physics, Azerbaijan Academy of Sciences, Baku, Azerbaijan.

^dAlso at Imam Mohammad Ibn Saud Islamic University, Saudi Arabia.

^eAlso at TRIUMF, Vancouver, Canada.

^fAlso at Department of Physics, University of Thessaly, Greece.

^gAlso at An-Najah National University, Nablus, Palestine.

^hAlso at Department of Physics, University of Fribourg, Fribourg, Switzerland.

ⁱAlso at Department of Physics, Westmont College, Santa Barbara, USA.

^jAlso at Departament de Física de la Universitat Autònoma de Barcelona, Barcelona, Spain.

^kAlso at Affiliated with an institute covered by a cooperation agreement with CERN.

^lAlso at The Collaborative Innovation Center of Quantum Matter (CICQM), Beijing, China.

^mAlso at Faculty of Physics, Sofia University, 'St. Kliment Ohridski', Sofia, Bulgaria.

ⁿAlso at Università di Napoli Parthenope, Napoli, Italy.

^oAlso at Institute of Particle Physics (IPP), Canada.

^pAlso at Borough of Manhattan Community College, City University of New York, New York, New York, USA.

^qAlso at National Institute of Physics, University of the Philippines Diliman (Philippines), Philippines.

^rAlso at Department of Financial and Management Engineering, University of the Aegean, Chios, Greece.

^sAlso at Institutio Catalana de Recerca i Estudis Avancats, ICREA, Barcelona, Spain.

^tAlso at Technical University of Munich, Munich, Germany.

^uAlso at CMD-AC UNEC Research Center, Azerbaijan State University of Economics (UNEC), Azerbaijan.

^vAlso at Yeditepe University, Physics Department, Istanbul, Türkiye.

^wAlso at CERN, Geneva, Switzerland.

^xAlso at Center for Interdisciplinary Research and Innovation (CIRI-AUTH), Thessaloniki, Greece.

^yAlso at Hellenic Open University, Patras, Greece.

^zAlso at Center for High Energy Physics, Peking University, China.

^{aa}Also at Department of Physics, Stellenbosch University, South Africa.

^{bb}Also at Department of Physics, California State University, Sacramento, USA.

^{cc}Also at University of Colorado Boulder, Department of Physics, Colorado, USA.

^{dd}Also at Département de Physique Nucléaire et Corpusculaire, Université de Genève, Genève, Switzerland.

^{ee}Also at Institut für Experimentalphysik, Universität Hamburg, Hamburg, Germany.

^{ff}Also at Institute for Nuclear Research and Nuclear Energy (INRNE) of the Bulgarian Academy of Sciences, Sofia, Bulgaria.

^{gg}Also at Washington College, Chestertown, Maryland, USA.

^{hh}Also at Institute of Applied Physics, Mohammed VI Polytechnic University, Ben Guerir, Morocco.

ⁱⁱAlso at Department of Physics, Stanford University, Stanford, California, USA.

^{jj}Also at Institute of Physics and Technology, Mongolian Academy of Sciences, Ulaanbaatar, Mongolia.